MONTE CARLO SIMULATIONS OF THE ADVECTIVE INFLOW AND OUTFLOW AROUND A BLACK HOLE

**Thesis submitted for the degree of
Doctor of Philosophy (Science)
of the
Jadavpur University**

Himadri Ghosh

S. N. Bose National Centre for Basic Sciences
Salt Lake, Sector-III, Block-JD
Kolkata-700098, West Bengal, India

Supervisor:

Sandip K. Chakrabarti
Senior Professor,
S. N. Bose National Centre for Basic Sciences
Salt Lake, Sector-III, Block-JD
Kolkata-700098, West Bengal, India

CERTIFICATE FROM THE SUPERVISOR

This is to certify that the thesis entitled **"MONTE CARLO SIMULATIONS OF THE ADVECTIVE INFLOW AND OUTFLOW AROUND A BLACK HOLE"**, submitted by **Sri Himadri Ghosh** (Index No. 352/07/Phys/17), who got his name registered on **26.06.2007** for the award of Ph.D. (Science) degree of Jadavpur University, is absolutely based upon his own work under the supervision of **Professor Sandip K. Chakrabarti** and that neither this thesis nor any part of it has been submitted for either any degree/diploma or any other academic award anywhere before.

<div style="text-align: right">

Sandip K. Chakrabarti
Senior Professor,
S. N. Bose National Centre for Basic Sciences,
Salt Lake, Sector-III, Block-JD,
Kolkata-700098, West Bengal, India.

</div>

March 28, 2012

ABSTRACT

In this Thesis, we describe the development of a three-dimensional radiative transfer code using Monte Carlo technique and its application to various astrophysical problems. This code is capable of simulating the radiation spectra coming out of the electron cloud of an accretion disk around compact objects, such as black hole X-ray binaries (XRBs). Physical processes included in this code are the relativistic Maxwell-Juttner momentum distribution of the electrons, Compton scattering with these electrons, and gravitational red shift of the photons. Due to general nature of the code, processes like synchrotron radiation, bremsstrahlung radiation, Coulomb coupling and the pair production are also possible to incorporate. Various types of photon energy distribution (e.g., mono-energetic, power-law, black-body and multi-colour black body) and geometry of the photon source (e.g., point or disk) can be used. In this Thesis, we have mainly used multi-color black body photons coming out of a Keplerian disk as the source of soft radiation. This soft radiation is intercepted by the electron cloud. Depending on the optical depth of the cloud, and energy of the electrons, the soft photons may get Comptonized and inverse-Comptonized via multiple scattering or may suffer no scattering at all, and they emerge out of the cloud as a relatively harder radiation. Our simulations provide information regarding the accretion disk and the central compact object. We apply the code to the Two Component Accretion Flow (TCAF) model of black hole XRBs to explain the cause of spectral state transitions. We have also applied this code in a system where both the inflow and outflow/jet are present. We find that the diverging outflow actually causes the down-scattering of the photons whereas the infalling matter upscatters them, thus the final spectrum in presence of jet/outflow is a complex mixture of both kinds of photons. In addition to using various static models (e.g., torus, sphere or sphere with a conical jet) arising out of the toy models or analytical solutions present in the literature, we also use realistic accretion flows obtained from time dependent hydrodynamic simulations. In the last part of the Thesis, we use the output of this simulation as the input flow configuration for our Monte Carlo simulation to calculate the spectral, timing and directional properties of the output radiation at each time step. We present results of zero angular momentum Bondi solution and low angular momentum accretion flows. One major conclusion is that in the presence of an axisymmetric disk which emits soft photons, even an originally spherically symmetric accreting Compton cloud losses its symmetry and becomes axisymmetric as there are considerably higher cooling along the axis. This effect becomes more prominent for low angular momentum flow which produces shock waves close to the axis. The post-shock region cools down and the flow velocity is also increased in the region. The effect of the bulk velocity of the electrons on the spectra is highlighted. We show that in the soft states, the bulk-motion Comptonization

leaves its mark as a power-law at high energies.

In Chapter 1, we have given a description of the important observations regarding the black hole candidates that have developed the subject in a historical perspective. Next, we have briefly discussed the major accretion flow models present in the literature. We have started with the Bondi flow. Spherical flows have very low efficiency of the outcoming radiation. This is due to the fact that the flow has a very high infall velocity. We then discuss the standard Keplerian disk model. This model explains the nature of the multi-colour soft X-ray spectrum very well but it fails to explain very high energy radiation coming from the stellar mass black holes and distant Quasars and AGNs. This brings the advective flows in the picture. This component has lower angular momentum than a Keplerian disk, and is called a sub-Keplerian flow. A realistic accretion flow may have both the components, a sub-Keplerian flow on the top of a Keplerian flow. This is the so-called two-component advective flow or TCAF model. In case of black hole physics, a full general relativistic approach is essential, but it makes the time dependent hydrodynamic equation which includes radiative transfer so complex that it is almost impossible to handle in a finite time. This problem is circumvented using a pseudo-Newtonian potential. This we discuss in this Chapter. This Chapter ends with a short note about the units and dimensions used throughout the Thesis.

In Chapter 2, we have presented the basic radiative processes in an accretion flow around a black hole. We have discussed only the two relevant radiative processes namely, black body radiation and Compton scattering, that we have used in this Thesis.

We then incorporated the physical processes described in Chapter 2 into the Monte Carlo technique, into our radiative transfer code. This is elaborated in Chapter 3. Different methods to model random variables have been discussed in this Chapter. Next, we apply these methods to model injected multi-colored black body spectrum, Compton scattering, scattering cross section and momentum of the electrons. This Chapter ends with a basic Monte Carlo exercise.

In Chapter 4 we have shown the application of our Monte Carlo code for a static electron cloud. We compute the effects of thermal Comptonization of soft photons emitted from a Keplerian disk around a black hole by the hot toroidal electron cloud. We show that the spectral state transitions of black hole candidates could be explained either by varying the size of the Compton cloud or by changing the central density of the same which is governed by the rate of the sub-Keplerian flow. We confirm the conclusions of the previous theoretical studies that the interplay between the intensity of the soft photons emitted by the Keplerian flow and the optical depth and electron temperature of the Comptonizing cloud is responsible for the state transitions in a black hole.

In a black hole accretion, the Keplerian component supplies low-energy (soft) photons while the sub-Keplerian component supplies hot electrons which exchange their energy with the soft photons through Comptonization or inverse Comptonization processes. In the sub-Keplerian flow, a shock is generally produced due to the centrifugal force. The post-shock region is known as the CENtrifugal pressure supported BOundary Layer or CENBOL. In Chapter 5, we compute the effects of the thermal and the bulk motion Comptonization on the soft photons emitted from a Keplerian disk by the CENBOL, the pre-shock sub-Keplerian disk and the outflowing jet. We study the emerging spectrum when both the converging inflow and the diverging outflow (generated from the CENBOL) are simultaneously present. From the strength of the shock, we calculate the percentage of matter being carried away by the outflow and determined how the emerging spectrum depends on outflow rate. The pre-shock sub-Keplerian flow was also found to Comptonize the soft photons significantly. The interplay among the up-scattering and down-scattering effects determines the effective shape of the emerging spectrum. By simulating several cases with various inflow parameters, we conclude that whether the pre-shock flow, or the post-shock CENBOL or the emerging jet is dominant in shaping the emerging spectrum, strongly depends on the geometry of the flow and the strength of the shock in the sub-Keplerian flow.

In Chapter 6, we carry out the time dependent numerical simulation where hydrodynamics and the radiative transfer are coupled together. We consider two component accretion flow in which the Keplerian disk is imersed inside an accreting low angular momentum flow (halo) around a black hole. The injected soft photons from the Keplerian disk are reprocessed by the electrons in the halo. We show that in presence of an axisymmetric soft-photon source, spherically symmetric Bondi flow losses its symmetry and becomes axisymmetric. In our simulation, the low angular momentum flow slows down and forms a centrifugal barrier which adds new features into the spectrum. We generated the radiated spectra from a two component system as functions of the accretion rates. We find that the transition from hard state to soft state is determined by the mass accretion rates of the disk and the halo. We separate out the signature of bulk motion Comptonization and discuss its significance in identifying a black hole candidate. We study how the net spectrum is contributed by photons suffering multiple scatterings and spending different amounts of time inside the Compton cloud. We study the directional properties of the spectrum as well. In the last part of the Thesis we have taken a moderate angular momentum flow where a shock is present. We find that the shock oscillates with time and the nature of the oscillation changes due to Compton cooling.

Finally, in Chapter 7, we draw concluding remarks and briefly mention our future plans.

ACKNOWLEDGMENTS

LIST OF PUBLICATIONS

1. S. K. Garain, <u>H. Ghosh</u> and S. K. Chakrabarti, **Effects of Compton Cooling on Outflow in a Two Component Accretion Flow around a Black Hole: Results of a Coupled Monte Carlo-TVD Simulation**, *The Astrophysical Journal* (to appear) (2012)

2. <u>H. Ghosh</u>, S. K. Garain, K. Giri and S. K. Chakrabarti, **Effects of Compton Cooling on the Hydrodynamic and the Spectral Properties of a Two-Component Accretion Flow around a Black Hole**, *Mon. Not. R. Astron. Soc.*, 416 (pp 959-971) (2011)

3. <u>H. Ghosh</u>, S. K. Garain, K. Giri, S. K. Chakrabarti, **Monte Carlo Simulations of Comptonization Process in a Two Component Accretion Flow Around a Black Hole in Presence of an Outflow**, *Proc. 12th Marcel Grossman Meeting on General Relativity, Eds. T. Damour, R. T. Jantzen & R. Ruffini*, World Scientific (pp 985-989) (2011)

4. <u>H. Ghosh</u> , S. K. Garain, S. K. Chakrabarti and P. Laurent, **Monte Carlo Simulations of the Thermal Comptonization Process in a Two-Component Accretion Flow Around a Black Hole in the presence of an Outflow**, *International Journal of Modern Physics D*, 19 (pp 607-620) (2010)

5. <u>H. Ghosh</u> , S. K. Chakrabarti and P. Laurent, **Monte Carlo Simulations of the Thermal Comptonization Process in a Two-Component Accretion Flow Around a Black Hole**, *International Journal of Modern Physics D*, 18 (pp 1693-1706) (2009)

6. <u>H. Ghosh</u>, S. K. Chakrabarti and Philippe Laurent, **Inverse Comptonization in a Two Component Advective Flow: Results of a Monte Carlo simulation**, *Proc. 2nd Kolkata Conference on Observational Evidence for Black Holes in the Universe, Eds. S. K. Chakrabarti & A. S. Majumder*, AIP Conference Proceedings, 1053 (pp 373-376) (2008)

7. S. K. Chakrabarti, D. Debnath, P.S. Pal, A. Nandi, R. Sarkar, M.M. Samanta, P.J. Wiita, <u>H. Ghosh</u> and D. Som, **Quasi periodic oscillations due to axisymmetric and non-axisymmetric shock oscillations in black hole accretion**,

Proc. 11th Marcel Grossman Meeting on General Relativity, Eds. H. Kleinert, R. T. Jantzen & R. Ruffini, World Scientific (pp 569-588) (2007)

8. S. K. Chakrabarti, <u>H. Ghosh</u> and D. Som, **Astrophysical black holes - do they have boundary layers?**, *Proc. 11th Marcel Grossman Meeting on General Relativity, Eds. H. Kleinert, R. T. Jantzen & R. Ruffini*, World Scientific (pp 1085-1097) (2007)

Contents

Chapter 1

Introduction

Astronomy and Astrophysics is a discipline which conducts scientific study of celestial objects. It includes the observation and interpretation of radiations that comes from various compact objects such as, black holes, neutron stars, white dwarfs, Gamma Ray Bursts (GRBs), Active Galactic Nuclei (AGNs), Quasars etc. In this Thesis we will concentrate only on black hole astrophysics.

1.1 Stars and Compact Objects

The life story of the stars has an important massage to give. The outer layers of a star sprayed out in space during a supernova explosion. They come in contact with fresh hydrogen and form a gaseous mixture, which contains all the chemical elements. This gaseous mixture is enriched by the products of many such explosions and forms a gas cloud. New stars are formed out of these clouds. The Sun is also one such star which is made up of countless supernova remnants dating back to the earliest years of the Galaxy. All the planets including the Earth is also composed almost entirely of these debris. Thus, we owe our existence to events that took places billions of years ago, in stars that lived and died long before the solar system came into being.

Compact objects, namely, white dwarfs, neutron stars and black holes, are 'born' when most of the nuclear fuel of normal stars has been consumed, that is, when the normal stars 'die'. These compact objects are different from the normal stars in two fundamental ways. First, they are unable to stop the gravitational collapse by generating thermal pressure due to the lack of nuclear fuel. To survive the complete collapse, White dwarfs use the degenerate electron pressure, while the neutron stars are supported by the pressure of degenerate neutrons. Black holes are stars that find no ways to prevent this inward pull due to gravity and completely collapse to singularities. All these three objects are essentially static over the lifetime of the

Universe and represent the final stage of stellar evolution. Second, these compact objects are smaller in size compared to the normal stars. Due to the smaller size the surface gravitational fields of the compact objects are much stronger compared to that of a normal star of similar mass. In Table 1.1, we show the comparison (Shapiro & Teukolsky, 1983).

Table 1.1

Object	Mass (M)	Radius (R)	Mean Density (g cm^{-3})	Surface Potential (GM/Rc^2)
Sun	$M_\odot$	$R_\odot$	1	10^{-6}
White dwarf	$\lesssim M_\odot$	$\sim 10^{-2} R_\odot$	$\lesssim 10^7$	$\sim 10^{-4}$
Neutron star	$\sim 1 - 3 M_\odot$	$\sim 10^{-5} R_\odot$	$\lesssim 10^{15}$	$\sim 10^{-1}$
Black hole	Arbitrary	$2GM/c^2$	$\sim M/R^3$	~ 1

Because of the presence of very high density of matter inside the compact objects, the hydrodynamics of matter and the nature of interparticle forces in and around them are very different from that of the normal stars. The large surface potential (Table 1.1) encountered in compact objects implies the importance of general relativity in determining their structure.

For a blackbody of temperature T and radius R, the flux varies as T^4, so that the luminosity varies as RT^4. White dwarfs are characterized by their higher effective temperatures than the normal stars even though they have lower luminosities. The reason for this mysterious behaviour is their smaller R value. Thus, white dwarfs are much 'whiter' than normal stars, hence their name. The reason behind the name 'neutron' star is the dominance of neutrons in their interior, following the mutual elimination of electrons and protons by inverse β-decay. White dwarfs can be observed directly using optical telescopes during their long cooling period. Neutron stars can be observed directly as pulsating radio sources ('pulsars') and indirectly as gas accreting, periodic X-ray sources ('X-ray pulsars'). Black holes are literally 'black' as it does not emit radiations that is observable with present day instruments. It can only be 'observed' indirectly by observing their environment. For example, a black hole can be observed as gas-accreting aperiodic or quasi-periodic X-ray sources under appropriate circumstances. The objective of this Thesis is to find out what could be the observable signatures of a black hole.

1.2   Black Holes

A large number of the 'stars' in the sky are actually multiple systems, having two (or more) stars orbiting around each other about their common centre of mass. These

are called binary star system. X-ray binaries belong to a class of binary stars that are luminous in X-rays. The X-rays are produced by matter falling from one component, called the donor (usually a relatively normal star) to the other component, called the accretor, which is compact: a white dwarf, neutron star, or black hole. The infalling matter releases gravitational potential energy as X-rays.

1.2.1   Classification of X-ray binaries

X-ray binaries are further subdivided into several subclasses. Though these classifications are sometimes overlapping, but they reflect the underlying physics better. The classification by mass (high, intermediate, low) refers to the optically visible donor (M_2), not to the compact X-ray emitting accretor (M_X).

a) Low-Mass X-ray Binaries

In the low-mass X-ray binaries (LMXB), one of the stars (primary one) is normally a black hole or a neutron star. The donor star transfers mass to the compact object by Roche-lobe overflow. The donor (or, secondary) of LMXB systems is less massive than the primary ($M_2 \sim 1 M_\odot$). White dwarfs, late-type main-sequence stars, A-type stars and F-G-type subgiants are found among the low-mass companion stars. A typical LMXB emits almost all of its radiation in X-rays which is originated from the accretion disk around the compact object. These objects are very bright in X-rays but are optically faint. The orbital periods of these binaries vary from few minutes to hundred of days. XTE J1550-564 is a well studied LMXB system having a low mass donor ($M_2 \sim 1.5 M_\odot$) with a black hole of mass $10 \pm 1.5 M_\odot$ and orbital periods 1.5 days. GRO J1655-40 ($M_X \sim 7.02 M_\odot$, $M_2 \sim 2.3 M_\odot$ and orbital period ~ 2.6 days) and GRS 1915+105 ($M_X \sim 14 M_\odot$, $M_2 \sim 1.2 M_\odot$ and orbital period ~ 33.5 days) are other two most well studied LMXBs (Liu et al. 2007).

• Soft X-ray Transients (SXTs)

SXTs are characterized by long periods of quiescence interrupted by intense outbursts where their luminosity can increase by more than 100 times. These outbursts emit radiations throughout the entire electromagnetic spectrum, including the radio (not always sufficient to detect), optical and X-ray wave lengths (van Paradjis, McClintock, 1995). SXTs contain primary object of mass $> 3 M_\odot$. It is most likely that the majority of SXTs contain black holes (Reilly, 2002).

b) High-Mass X-ray Binaries

The HMXB systems are made up of a compact primary object orbiting a high mass OB class star (secondary). The primary component is a strong X-ray emitting neutron star or a black hole. Conventionally, HMXBs can be further divided into two subgroups: first, where the donor is a Be star and the compact object is a neutron

star (Be/X-ray binary) (Zhang, Li & Wang 2004). X-ray outbursts occur when the compact object passes through the Be-star disk, accreting from the low-velocity and high-density wind around Be stars. These X-ray spectra are generally hard in nature. The hard X-ray spectrum, along with transience, is the most interesting characteristic of the Be/X-ray binaries. In the second group of HMXB systems, the donor is a supergiant early-type star (SG/X-ray binary). The compact object orbits deep inside the highly supersonic wind. For these HMXB systems the X-ray luminosity is powered by either the strong stellar wind of the optical companion or Roche-lobe overflow. The X-ray luminosity of $10^{35} - 10^{36} ergs^{-1}$ is produced by the stellar wind. Whereas, a much higher ($\sim 10^{38} ergs^{-1}$) X-ray luminosity is produced in a Roche-lobe overflow system where matter flows via the inner Lagrangian point to an accretion disk (Liu et al. 2006).

To summarize, the donor mass ($\gtrsim 10 M_\odot$) of HMXB system is much higher compared to LMXB ($\lesssim 1 M_\odot$). In HMXB the emission dominates in optical wave length and therefore easy to detect. One of the most well known HMXB is Cyg X-1, which was the first detected stellar-mass black hole (Giacconi et al. 1962). This binary system consists of high mass donor of mass $20 - 30 M_\odot$ with a compact object of mass $6 - 10 M_\odot$.

c) Intermediate-mass X-ray binaries

Above we have described the HMXB and LMXB systems with companion stars having $M_2 \gtrsim 10 M_\odot$ and $\lesssim 1 M_\odot$, respectively. There are also a large number of Galactic compact binaries with companion star masses in the interval $1 - 10 M_\odot$ (van den Heuvel, 1975). These are the so-called intermediate mass X-ray binaries (IMXBs). In this Thesis, we have mainly worked with HMXB and LMXB systems.

1.2.2   Classification of Black Holes

Depending on their physical masses, there are four classes of black holes: stellar, intermediate, supermassive and primordial (or mini). A stellar black hole is a region of space into which a star has collapsed. This type of black holes are created when a star whose remnant core can be more than $2 - 3 M_\odot$ (the Tolman-Oppenheimer-Volkoff limit for neutron stars) reaches the end of its thermonuclear life. The self-gravity of the star then overcomes both electron and neutron degeneracy pressure and the star collapses to a critical size, here gravity dominates all other forces. Black holes found at the center of galaxies have a mass up to 100 million solar masses and are called supermassive black holes. Between these two scales, there are believed to be intermediate black holes with a mass of several thousand solar masses. Primordial black holes, proposed by Stephen Hawking, could have been created at the time of the BIG-BANG due to perturbations in the homogeneous background density field

(Zel'dovich and Novikov, 1966; Hawking, 1971), when some regions might have got so compressed that they underwent gravitational collapse. With original masses comparable to that of earth or less, these mini black holes could be of the order of $1cm$ or smaller. Their existence is, as yet, not confirmed.

We can also classify black holes according to their physical properties. The simplest massive black hole has neither charge nor angular momentum. These non-rotating black holes are the Schwarzschild black holes after Karl Schwarzschild who discovered this solution in 1915. An electrically charged but non-rotating black hole is called Reissner-Nordstrom black hole. Rotating black holes can also be classified in two types. One type of this class does not have any charge: they are called Kerr (after Roy Kerr) black holes. Another type are not electrically neutral and are called the Kerr-Newman black holes. These rotating black holes obey exact black hole solutions of Einsteins equations of General Relativity. When a massive spinning star suffers gravitational collapse rotating black holes are formed. The collapse of a collection of stars or gas with an average non-zero angular momentum can also form a rotating black hole. As most stars rotate it is expected that most black holes in nature are rotating black holes. In the present Thesis, we work only with non-rotating Schwarzschild black hole.

Table 1.2

Class	Mass	Size
Supermassive BH	$\sim 10^6 - 10^9 M_\odot$	$0.001 - 10AU$
Intermediate-mass BH	$\sim 10^3 M_\odot$	$10^3 km = R_\oplus$
Stellar-mass BH	$\sim 10 M_\odot$	$30km$
Primordial BH	$\gtrsim M_{Moon}$	$\lesssim 1cm$

To conclude this Section, a black hole is defined as a region of spacetime that can not communicate with the external universe. The boundary of this region is called the surface of the black hole, or the *event horizon*. The ultimate fate of the collapsing matter, once it has crossed the event horizon, is not known. Black Holes are the simplest of the celestial objects to describe mathematically. To describe the astrophysical processes around a black hole one requires only two constant parameters about the black hole, namely, the mass M and the spin a which can vary from 0 to 1. Stars would require more parameters such as the temperature, pressure, ionization, boundary layer etc. on the star surface.

1.3   X-ray Observations from Black Holes: Historical Perspective

No observable radiation can come out of a black hole horizon. Thus, black holes must be detected by monitoring the radiations emitted by matter accreting on them. There are many indirect ways that tell us if there is any black hole at galactic centers or in binary systems. For instance, one could detect the evidence of rotation of the disk matter by observing the Doppler shifts of the lines emitted from the accretion disk. Alternatively, one could look for the powerful jets which are ejected from the centre of the galactic nuclei. Generally the accretion flows are targeted for identification of black holes as the radiations coming out of an accretion flow carry information about the matter that are being accreted onto the black holes. The radiation is necessarily dependent on the nature of the density and temperature distribution of the accreting matter, which in turn depend on the hydrodynamics of the flow. The hydrodynamics of the flow again depends on the angular momentum of the flow and the nature of the heating and cooling processes in the matter. Thus, the whole process of detecting black holes involves a thorough understanding of the radiative hydrodynamics of the flow in a curved geometry.

Fortunately, there are reasonable assumptions which may be used. For instance, one can replace the general relativistic computation procedure by a pseudo-Newtonian computation procedure discussed below in §1.8. The basic features of the solutions remain almost identical to those obtained in a curved space-time around a black hole. In our study, we shall assume one such simpler model of the accretion flows.

One could study the spectral properties in three distinct ways: the first is through direct observation of the radiation. Different ground based (IR, optical, very high energy gamma rays) or space based (optical, UV, X-rays, gamma-rays) instruments are used in this method. Here, one tries to find out if there are fast variabilities or spectral signatures in the observed radiation. These observations may point to massive compact objects at the core or some spectral signatures especially predicted for black holes. A second method, which is used in this Thesis, is to solve equations which govern the motion of matter around a black hole and produce the most likely solutions which explain both the steady and time-dependent behaviour of the radiation. The third approach is intermediate between the other two approaches: the theoretical results are assimilated to give models and then one fits the observational results with these models using several free parameters.

To understand the production of X-rays and gamma-rays, one needs to realize that the radiation energy is generally due to the thermal energy or the bulk energy of matter. Since 1 eV radiation comes out of a gas of typical temperature $T \sim 10^4$

K, for an X-ray emission of about 10 keV the electron cloud need to have $T \sim 10^8$ K. X-rays from accretion onto compact objects could not be studied from ground because of severe absorption by the atmosphere.

In 1962 Giacconi and his team analyzed the data from a rocket carrying a payload consisting of three large Geiger counters. The analysis revealed a considerable flux of radiation in the night sky that was identified as consisting of soft X-rays. Thus Cosmic X-Ray sources were discovered. Cyg X-1, the first black hole candidate, was discovered in these early attempts in 1962 (Giacconi et al. 1962; Giacconi et al. 1965; Gursky et al. 1966).

In 1970, the first Astrophysics related satellite UHURU was launched. Black hole candidate Cyg X-1 was among the first few objects which was observed by this satellite. In the first few papers (Giacconi et al. 1971) it was shown that this source emits X-rays of energy larger than 100 keV. At similar times, analytical solutions of the disk variables such as temperature, density etc. as a function of the radial distance from the axis were presented by Shakura and Sunyaev, 1973 (hereafter SS73). This model is known as standard disk model. SS73 also computed the radiation spectrum by adding black body contribution from successive annulus of the disk to get the multi-colour black body spectrum. The hall mark of the standard disk model was this so-called multi-colour black body spectrum. It was apparent from X-Ray observations (Agrawal et al. 1972; Tananbaum et al. 1972) that Cyg X-1 actually has a 'soft state' (when X-ray power is emitted mostly in soft X-rays) and a 'hard state' (when X-ray power is mostly emitted in hard X-rays) along with the two distinct components of the spectrum. Subsequently, it was argued by Thorne and Price (1975) that SS73 disk model is unable to explain the high energy X-rays found in Cyg X-1 since the temperature of standard disk is too low. Observed spectra of black hole candidates, such as Cyg X-1 (Sunyaev & Truemper, 1979) clearly indicated the presence of two distinct components, a low energy black-body component and a high energy power-law component. Observations similar to Cyg X-1 were made for active galaxies and Quasars (Katz, 1976). It was shown that the multi-colour black body emission from a Keplerian disk could explain the soft X-ray bump in these spectra. In 1979, Galeev, Rosner and Vaiana used Comptonization of softer photons by hot electrons from a magnetic Corona on an accretion disk to explain the power-law component of the spectra.

The nature of the emitted spectrum from an optically thick converging inflow in Newtonian geometry was studied by Payne and Blandford (1981). They found that the energy spectral index α ($I(\nu) \sim \nu^{-\alpha}$) would be ≈ 2. Considering the general relativistic calculations, α became 1.5 and turns out to be the most convincing signature of a black hole candidate (Chakrabarti & Titarchuk, 1995, hereafter CT95). Wandel, Yahil and Milgrom (1984) and Colpi, Maraschi and Treves (1984) gave

a more general solution in Newtonian geometry. They studied single temperature solution of non-adiabatic flows. It was shown that the Quasar luminosity increases with the accretion rate of the converging inflow and the luminosity is a few percent of the Eddington luminosity. However, spherical or converging flows failed to explain the spectrum of Seyfert galaxies and Quasars, where clear excess of radiation in ultraviolet was seen (Malkan & Sergent, 1982). Several ultraviolet-optical-infrared spectra of quasars and AGNs were fitted using improved multi-colour blackbody radiation emitted by Shakura-Sunyaev Keplerian disk (SS73) and satisfactory results were found (Sun & Malkan, 1989). The mass of the black hole was found to be $\sim 10^8 M_\odot$. It was shown by Wandel and Petrosian (1988) that basically two parameters, namely the mass of the black hole and the accretion rate can describe the spectrum of a thin accretion disk very well and the black hole mass was in the range $10^8 - 10^{9.5} M_\odot$ for the Quasars and $10^{7.5} - 10^{8.5} M_\odot$ for the Seyferts. The disk model was improved by Ross, Fabian and Mineshige (1992) by properly treating the inner edge of the accretion disk. They showed that even for disks around a massive black hole, a significant radiation could be in soft X-rays. Generally, line emissions along with continuum emissions are also shown by active galactic nuclei. Rapidly moving clouds on both sides of an accretion disk are believed to emit these lines. The mass of the central object can be estimated by the measurement of the Doppler shift due to the motion of the cloud and the distances of the cloud from reverberation mapping (variation in strengths of the central photoionizing source in a quasar or Seyfert galaxy generates variations in the strengths and profiles of the emission lines) (Blandford & McKee, 1982).

The launching of EXOSAT in 1983 and GINGA in 1987 made the subject of high energy astrophysics more interesting. For Low Mass X-ray binaries (LMXRB), a large amount of data in X-Rays were becoming available. Important discovery, like the Quasi-periodic Oscillations (QPOs) in LMXRBs and X-ray pulsars were made from these data. It was very clear from the observations that a source of hot electrons is required for Compton scattering as indicated by Sunyaev & Titarchuk (1980, 1985; hereafter ST80 & ST85). Sources such as Cyg X-1, LMC X-3, A0620-00 were identified to be black hole candidates (McClintock and Remillard, 1986) by dynamical considerations. Observations of X-ray spectra for four low-mass binary X-ray sources, Sco X-1, 4U 1608-522, GX 5-1 and GX 349+2 performed with the gas scintillation proportional counters on board Tenma, revealed that every observed spectrum can be expressed by a sum of two spectral components (Fig. 1.1): a hard power-law component and a soft multi-color blackbody component, whose spectral shapes are fixed for each individual source (Mitsuda et al. 1984).

It is very important to identify the source of the high energy X-rays to understand the observed X-ray properties. Earlier, it was believed that Comptonization of
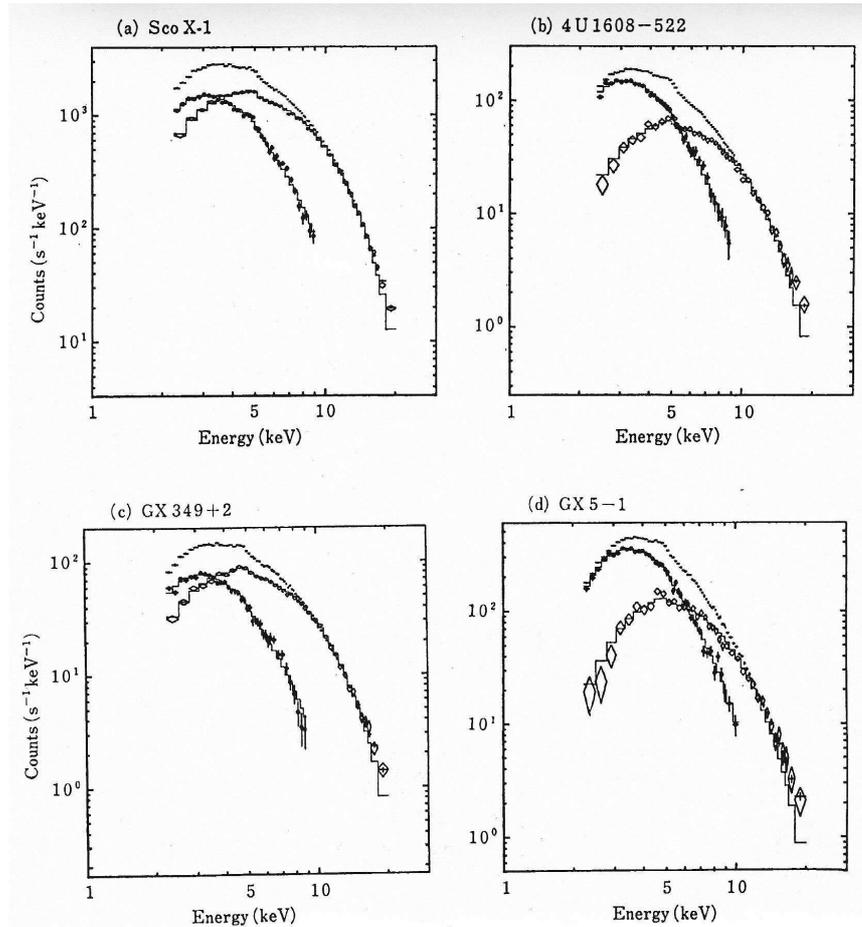
Figure 1.1: Examples of early observation of the net spectra (cross) for Sco X-1, 4U 1608-522, GX 349+2, GX 5-1 and the hard (rhomb) and soft (crossed circle) components of the net spectra. The best-fit 2-keV blackbody and the 'multicolor' spectra are shown by the histograms (Mitsuda et. al. 1984).

soft photons by 'Compton Clouds' floating around the disk or hot corona resulted the hard radiation. Two phase accretion in AGNs were considered by Haardt and Maraschi (1991, 1993), one with cold component along the equatorial plane, and the other with hot component above the cooler component. CT95 introduced the two component advective disk model. Though this model requires more improvement, this picture is generally adopted in most of the models of accretion flows.

1.4   Spectral Properties of Galactic and Extragalactic Black Holes in X-rays

1.4.1   The Eddington Limit

Before discussing the spectral properties of an accretion disk, let us define an useful term called the Eddington limit (Shapiro & Teukolsky, 1983). 'Eddington luminosity' is the maximum theoretical luminosity for which the inward gravitational pull on protons in a fluid element balances the outward force of radiation on electrons (i.e., the maximum luminosity at which matter can be accreted),

$$L_{Edd} = \frac{4\pi GM m_p c}{\sigma_T} = 1.3 \times 10^{47} M_9 \text{erg s}^{-1}, \tag{1.1}$$

where, m_p is the mass of the proton, σ_T is the Thomson scattering cross-section and M_9 is the mass of the central black hole in units of $10^9 M_\odot$. The luminosity of the quasars and active galaxies has been observed to be sometimes as high as 10^{47} erg s^{-1}. The usual explanation for such a high energy output is that the energy is mostly coming from the gravitational binding energy of matter accreting onto a massive black hole with $M \sim 10^9 M_\odot$. The corresponding Eddington rate is defined as $\dot{M}_{Edd} = L_{Edd}/c^2$.

The characteristic black body temperature of the radiation that is emitted from an accretion disk with luminosity L_{Edd} at $r = r_g$ is given by (Chakrabarti, 1996a),

$$T_E \sim 2.8 \times 10^5 M_9^{-1/4} \ K. \tag{1.2}$$

Eddington rate is an upper limit of the accretion rate. It is an indicator of the rate at which matter is falling onto a black hole. Usually, the actual accretion rate is much lower than the Eddington rate, there are evidences of the presence of higher accretion rates as well. However, higher accretion rates are also allowed for black holes as some of the radiations could be trapped and advected inside the horizon.

1.4.2   Examples of different spectral states

We now provide an example of the spectral state variation of stellar mass black holes in in Fig. 1.2. We plot the power (EF_E) in the y-axis and the energy (E) in the X-axis. In the so-called soft state, the power is high in the low energy X-rays which is dominated by a multi-colour black body spectrum. At high energies, the power drops off rapidly. Occasionally a power-law is seen extending to ~ 0.5 MeV and could be due to bulk motion of the matter entering into the black hole. An
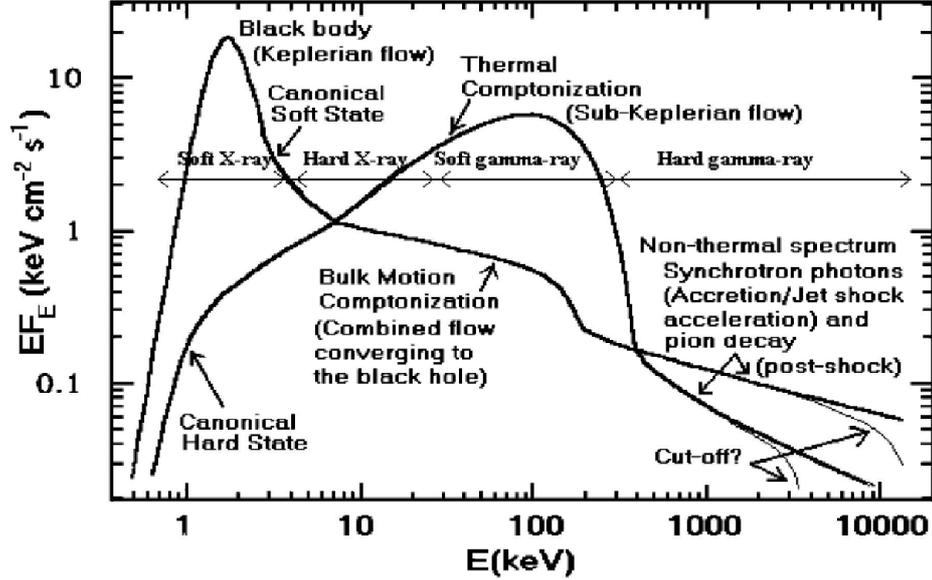
Figure 1.2: Power (EF_E) as a function of energy E in the soft and hard states of a stellar mass black hole. Soft states are dominated by high power at lower energy X-rays, while the hard states are dominated by high power at intermediate energies ($\sim 40 - 100$ keV) while the $2 - 20$ keV region is well described by a power-law. There could be a non-thermal power-law component at high energies (low power) in both the cases.

extended power law till ~ 20 Mev which is also seen sometimes, could be due to non-thermal Comptonization of the non-thermal synchrotron radiation. In the so-called hard states, the power is very low at low energy X-rays due to the low accretion rate of the Keplerian disk. However the power is high typically at $\sim 40 - 100$ keV. In the $2 - 20$ keV range the spectrum is a power-law (straight line in a log-log scale). After the exponential cut-off, a power-law spectrum is again seen in the $\sim 200 - 1000$ keV range which could be due to Comptonization of the non-thermal synchrotron photons. The non-thermal electron population may come from shock acceleration or other non-thermal means. This spectrum is taken from Chakrabarti (2005) and references therein (McConnell et al. 2002; Ling & Wheaton, 2003, 2005; Case et al. 2005).

In case of supermassive black holes, from a purely theoretical point of view, it is expected that a similar spectral states should be present, though the blackbody
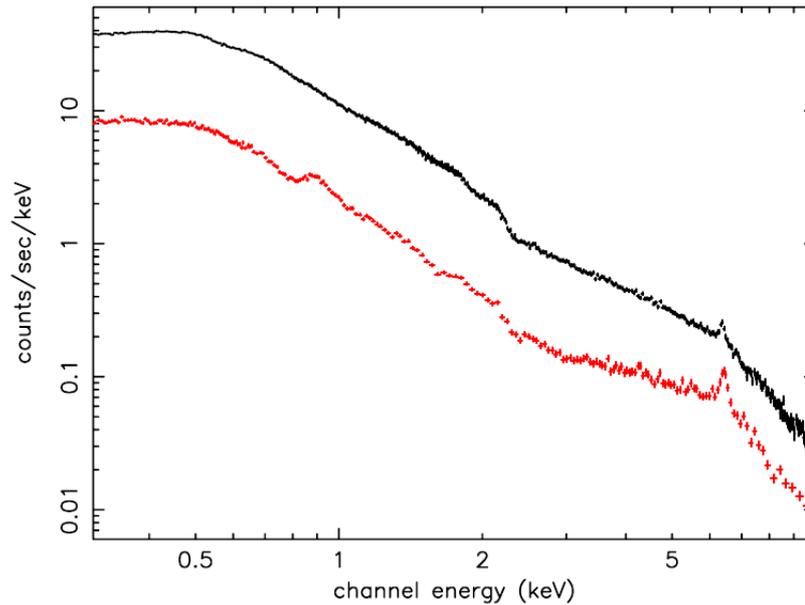
Figure 1.3: Background subtracted *XMM-Newton* X-ray spectra of the nearby Seyfert galaxy NGC 4051, taken in relatively high (2001 May, black) and low-flux (2002 November, red) states. See, Pounds et al. (2004) and the references therein.

spectral bump is at UV band, rather than at soft X-rays. In stellar mass black holes, the state transition may occur in a few tens of seconds to a few days. In supermassive black holes, where the mass could be up to 10^9 times larger, this time scale would be proportionally higher. It is unlikely that the transition could be seen at all.

In Fig. 1.3, the broad-band X-ray spectra of NGC 4051, integrated over the separate *XMM-Newton* observations, are shown (Figure taken from Pounds et al. 2004). We notice here that the mean flux levels of these two spectra are very much different. From ~ 0.3 to 3 keV the spectral shape is almost unchanged, only difference is that the flux in 2001 is about 5 times higher than that in 2002. From ~ 3 keV up to the emission line at ~ 6.4 keV, the flux ration decreases. In this energy band the low-state (red plot) spectrum indicates a flatter continuum slope. The emission line at ~ 6.4 keV appears to be unchanged for these two spectra.

1.5   An Overview of the Accretion Flow Models

In astrophysical context, the accretion is a process by which diffused matter in orbital motion is collected around a central object and an accretion disk is a structure where the gravitational energy is converted into kinetic and thermal energy. Accretion occurs in systems like X-ray binaries, active galactic nuclei (AGNs) etc. where white dwarfs, neutron stars and even super massive black holes may be located at the center. In low mass X-ray binary system, there are two ways by which matter can be supplied from the companion to the compact object. Matter with Keplerian angular momentum is accreted through the Lagrange point when the Roche lobe of the companion overflows. If the companion has a significant wind with it, and the compact object moves through the wind, then some winds with a very little angular momentum is also accreted. Another way to accrete matter from the companion is through tidal disruption. In this case the companion star is tidally deformed and matter flows out from it to the compact object. Matter can also be accreted from the interstellar medium at a very low rate in case of an isolated object. In many of the galactic centers there are evidences of the presence of supermassive black holes. In absence of companions, these black holes accrete matter from winds of surrounding stars. Those surrounding stars may also get tidally disrupted if they come very close to the black hole and the matter would be accreted from the disrupted star to the central black hole.

There are several accretion and wind solutions in the literature, but their applicability is restricted. To describe a black hole accretion, several quantities are important: specific energy (ϵ), specific angular momentum (λ), viscous stress etc. A mass accretion rate ($\dot{M}$) is also needed. Some models use two mass accretion rates, one for the Keplerian disk and the other for the sub-Keplerian disk.

(a) **Steady, spherically symmetric accretion: Bondi Flow**

The steady state behaviour of spherically accreting matter which has no angular momentum, was first studied by H. Bondi (1952). A detailed description of this particular type of flow has been given in Theory of Transonic Astrophysical Flows (Chakrabarti, 1990; hereafter C90). Let us assume a compact object of mass M, accretes matter from a large gas cloud. The object is at rest with respect to the cloud. The matter flow is spherically symmetric, and adiabatic in nature, i.e., there is no exchange of energy between the gas cloud and outside world. In case of Bondi flow, the mass accretion rate is given by,

$$\dot{M} = 4\pi r^2 \rho v, \tag{1.3}$$

which is constant throughout the flow. To conserve the accretion rate, the density (ρ) and velocity (v) will go up simultaneously, as matter accretes radially towards the

compact object. In case of a Bondi flow onto a Schwarzschild black hole, the matter velocity must reach the velocity of light (c) at the horizon making the density close to zero as most of the matter vanishes through the horizon. On the other-hand, the flow at infinity where the matter is almost at rest, is characterized by the velocity v_∞ and density ρ_∞. Apart from these two boundary conditions, for a fluid of highly relativistic point particles, maximum attainable sound speed is $c/\sqrt{3}$ (Weinberg, 1972). Thus the black hole accretion is transonic in nature, and the flow velocity becomes equal to the velocity of sound at a particular distance r, away from the compact object. The distance is called sonic radius (r_s) at which the flow changes from subsonic to supersonic. We can calculate the mass accretion rate in terms of ρ_∞ and T_∞ , where T_∞ is the temperature of the flow at infinity. It is given by (Shapiro & Teukolsky, 1983),

$$\dot{M} = 1.2 \times 10^{10} \left(\frac{M}{M_\odot} \right)^2 \left(\frac{\rho_\infty}{10^{-24}\text{gcm}^{-3}} \right) \left(\frac{T_\infty}{10^4\text{K}} \right)^{-3/2} \text{g s}^{-1}. \qquad (1.4)$$

This mass accretion rate would produce a luminosity of $\sim 10^{31}$ erg/s ($\sim 1\%$ of solar luminosity). Thus Bondi flow is radiatively inefficient. Unless magnetic fields and other dissipative mechanisms are added, this flow radiate very little and thus cannot explain the high luminosities as in a quasar.

(b) **Standard disks:**

The first accretion disk flow model was proposed by Shakura (1972), but the complete work on the model was published in a subsequent article by Shakura & Sunyaev (SS73) and the disk is generally known as the Shakura-Sunyaev disk (SS disk) or the standard disk. A relativistic version of the model was put forward by Novikov & Thorne in 1973. In this disk model, it is assumed that the accreted matter forms a geometrically thin disk in which matter rotates in Keplerian orbits and that the inflow velocity is much smaller than the free-fall velocity. The matter has angular momentum distribution same as the Keplerian distribution (obtained by equating gravitational force with centrifugal force). The accretion velocity is negligible, though it can have any reasonable accretion rate. The viscous torque ($t_{r\phi}$) which acts on different layers of the accreting matter transports the angular momentum outwards and thus makes the accretion possible. In this model $t_{r\phi}$ was assumed to be proportional to the total vertically averaged pressure of the gas in the disk, p_{total}, i.e.,

$$t_{r\phi} = \alpha_{ss}p_{total}, \qquad (1.5)$$

where, $\alpha_{ss} < 1$ is the so called viscosity parameter. The larger the value of α_{ss}, the more efficient is the transport of angular momentum outwards. As α_{ss} increases, radial velocity (at a constant $\dot{M}$) of the flow increases and the surface density (Σ) of the disk decreases.

For the steady-state disk, the energy flux, radiated from unit surface area of the disk per unit time at a radius R can be written as,

$$Q(R) = \frac{3}{8\pi} \dot{M} \frac{GM}{R^3} \left[1 - \left(\frac{R_0}{R} \right)^{1/2} \right], \tag{1.6}$$

and the corresponding luminosity produced by the disk in between R_1 and R_2 is given by,

$$L(R_1, R_2) = 2 \int Q(R) 2\pi R dR,$$

which yields,

$$L(R_1, R_2) = \frac{3GM\dot{M}}{2} \left[\frac{1}{R_1} \left[1 - \frac{2}{3} \left(\frac{R_0}{R_1} \right)^{1/2} \right] - \frac{1}{R_2} \left[1 - \frac{2}{3} \left(\frac{R_0}{R_2} \right)^{1/2} \right] \right]. \tag{1.7}$$

For $R_1 = R_0$ (the radius of the central star or the Schwarzschild radius) and $R_2 = \infty$ the total luminosity radiated from the accretion disk becomes,

$$L_{disk} = \frac{GM\dot{M}}{2R_0}. \tag{1.8}$$

So, half of the gravitational energy is radiated away from the accretion disk.

In case the Shakura-Sunyaev disk is optically thick and opacity due to free-free absorption is more important than the opacity due to scattering, each element of the disk surface radiates blackbody spectrum with surface temperature $T(R)$ given by equating the dissipation rate to the blackbody flux,

$$T(R) \approx 5 \times 10^7 \left(\frac{M}{M_\odot} \right)^{-1/2} \dot{M}_{17}^{1/4} (2R)^{-3/4} \left(1 - \sqrt{\frac{3}{R}} \right)^{1/4} K. \tag{1.9}$$

In this equation M is measured in units of $M_\odot$, $\dot{M}_{17}$ is in units of 10^{17} g s^{-1} and R is measured in units of $2GMM_\odot/c^2$.

This disk is radiatively very efficient. But, the disk is terminated at the last stable circular orbit ($3r_g$ for Schwarzschild black hole). The effective temperature of the radiation is around ~ 1 keV for stellar black holes ($M \sim 10M_\odot$). However, for Quasars, the radiation emitted from such a disk is in the ultraviolet region and is widely known as the big blue bump. This disk is an ideal solution, as it assumes the angular momentum distribution to be pre-determined (Keplerian λ_K) and it has no solution below $r = 3r_g$. The gas pressure is assumed to be negligible. This model is unable to explain the observed emission features of accreting black holes at energies higher than 10 keV.

(c) **Thick Accretion Disks:**

In order that the disks are more efficient radiators and also to collimate the jets, one needs to incorporate the effects of pressure. Paczyński and his collaborators assumed the disk to be radiation pressure dominated and radial velocity of the matter is zero (Paczyński & Wiita, 1980, hereafter PW80). Due to high pressure, the initial angular momentum of the disk is deviated from its Keplerian distribution. Thus, the disk puffs up and the height becomes comparable to the radial distance, hence the name thick disk. For low accretion rate and radiatively inefficient flow the thermal pressure (Rees et al. 1982) instead of radiation pressure can also make a thick disk. In such disks, the region around the vertical axis is devoid of matter due to centrifugal force. Just like the SS disk, this solution is also not transonic as the horizon is not joined to infinity (no radial velocity). In a General Relativistic thick disk, Chakrabarti-distribution of angular momentum derived using von-Zeipel theorem is used (Chakrabarti, 1985).

In late 80's and early 90's, improvements in space-borne (satellite) and ground based (radio antennas) instruments have triggered the challenge to explain the observed X-ray spectra of the black hole binaries. In low energy range (< 10 keV), the spectrum was modeled as a blackbody spectra but at high energies (few 100 keV) there was power-law like behaviour whose slope changes from time to time. The Standard disk and the thick-disk both were unable to reproduce the hard spectra extending upto 100 keV and beyond. To explain this, the presence of hot ($T_e \sim 10^9$ K), optically thin plasma was required. At the same time a very interesting feature called the quasi-periodic oscillations (QPOs) was also observed in most of the galactic black hole cadidates. It was found that the X-ray variabilities are quasi-periodic in nature and their Fourier decomposition shows a very prominent peak in the power density spectrum (PDS). The radio observations confirmed that the jets and outflows that are observed in GBHs are coming out from vicinity of the hole. To explain all the above features, a complete accretion disk model was needed instead of different models to explain different observations.

(d) **Two Component Advective Flows (TCAF):**

In early 90's, Chakrabarti and his collaborators (C90; Chakrabarti & Molteni, 1993; CT95; Chakrabarti, 1996a; 1996b; Molteni, Sponholz & Chakrabarti, 1996; hereafter referred to as MSC96) presented a accretion disk solution incorporating all the physical processes by solving the most general flow equations. A schematic representation of the accretion disk in this model is shown in Fig. 1.4.

An advective accretion disk is one which advects, or carry 'something', namely, mass, entropy, energy etc. This means, an advective disk should have a finite radial velocity which may even reach the velocity of light on the horizon. Therefore, before entering into a black hole, matter had to be supersonic (i.e., Mach number,
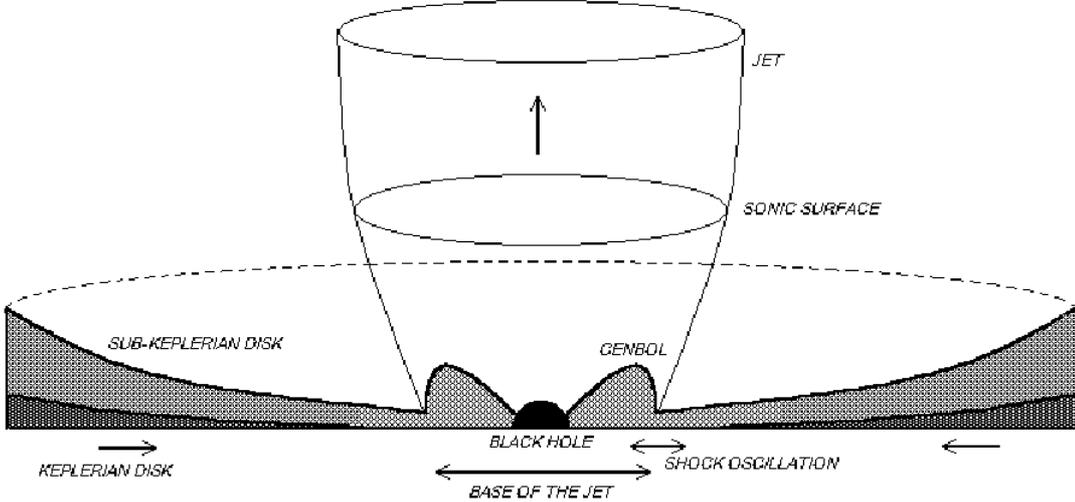
Figure 1.4: Cartoon diagram of the Two Component Advective Flow (TCAF) solution around a black hole, which shows the disk-jet connection highlighting different components. The centrifugal pressure dominated boundary layer or CENBOL is the postshock region of the combined Keplerian and sub-Keplerian flow. There could be transient shocks close to the inner sonic point (Chakrabarti, 2003).

$M_a = v/a > 1$, where v and a are radial velocity and sound speed respectively). As $v \sim 0$ at infinity, the matter must pass through at least one sonic point ($M_a = 1$), and as a sub-Keplerian flow (i.e., a flow with specific angular momentum $\lambda < \lambda_K$, the Keplerian angular momentum). Close to the black hole the matter falls very rapidly towards the horizon, thus making $\lambda \sim constant$. As the matter approaches the black hole, the centrifugal force ($\sim 1/r^3$) grows much faster compared to the gravitational force ($\sim 1/r^2$) and creates a shock or 'boundary layer' before entering into a black hole. For a large region of the parameter space (C90), a stable solution can have a standing shock wave. Depending on the physical parameters, a shock may be steady or oscillating in nature, it may even be absent. The oscillations of the shock may give rise to the temporal variability in the form of QPOs which are observed in many of the BH candidates. In this 'boundary layer', the flow kinetic energy is converted into the thermal energy forming a hot Compton cloud which can inverse-Comptonize the soft photons into hard photons and produce outflows and winds (Chakrabarti, 1999; hereafter C99). This boundary layer is called the CENtrifugal pressure supported BOundary Layer (or, CENBOL).

Two Component Advective Flow (TCAF) (Fig. 1.4) is a combination of two types of flows: a highly viscous Keplerian component which is accreted in long, viscous time scale and a initially sub-Keplerian component, with higher radial velocity and lower angular momentum. The sub-Keplerian flow is accreted in the short, free-fall time scale. The Keplerian disk, because of its low energy, resides at the equatorial plane, while matter with lower angular momentum flows above and below it. The wind is predominantly produced from the CENBOL area, which is the post-shock region. A transient shock can also be present just outside the inner sonic point. The inner edge of the Keplerian disk is terminated at the shock loaction. The amount of matter inside the jets and outflows vary due to the shock-oscillation.

The soft radiation coming from the Keplerian disk is intercepted by the hot sub-Keplerian flows in the CENBOL region and is re-radiated after multiple scattering. This radiative transfer between the photons and electrons changes the temperature of the electron cloud. Depending on the relative importance of the Keplerian disk rate $\dot{M}_d$ and the sub-Keplerian halo rate $\dot{M}_h$, the electrons in the sub-Keplerian disk may loose (inverse Compton scattering) or gain (Compton scattering) energy. When the electron cloud gets hotter, the system is in the hard state and if the electron cloud cools down by loosing energy to the photons, the system is in the soft state. The hard state is thus dominated by a power-law hard photon component. In the soft state, the electrons in CENBOL cooled down and collapses, but due to the inner boundary condition (matter must be supersonic when it reaches the horizon), the matter accelerates rapidly and up-scatters photons to its energy ($\sim m_e c^2$). Thus, the power-law photons can also be seen in the soft state due to this so-called, bulk motion Comptonization (BMC) (CT95).

In Fig. 1.5 we present the evolution of the solution of transonic flows since 1990 (Chakrabarti, Ghosh & Som, 2008; hereafter CGS08). With more and more applications, the solution is also enriched. Each diagram is drawn with specific solution in mind.

The general type of accretion is shown in Fig. 1.6 (adapted from Chakrabarti, 2008). We see that different parts of the flow actually behaves as individual solutions already existing in the literature. Thus in reality, an accretion flow is a complex mixture of all the known types of solutions: Bondi, transonic, Keplerian, thick disks, sub-Keplerian (transonic) and outflows (transonic). In various situations, various components may become dominant.
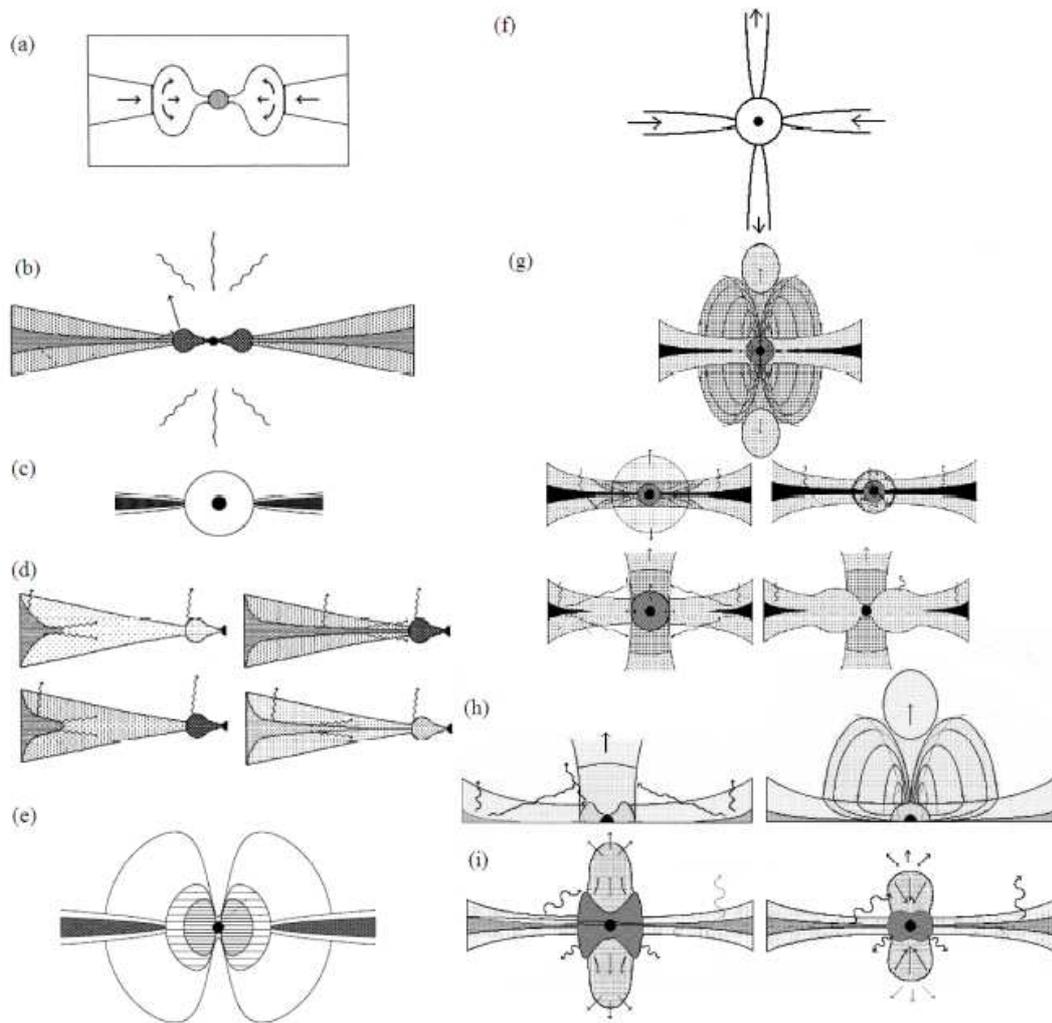
Figure 1.5: Evolution of the solution of the transonic flow to keep up with more and more observational data. (a) C90 ; (b) CT95; (c) Ebisawa, Titarchuk & Chakrabarti, 1996; (d) Chakrabarti & Sahu, 1997; (e) Chakrabarti, 1997; (f) Chakrabarti, 1998ab; (g) Chakrabarti & Nandi 2000; (h) Nandi et al. 2001; (i) Chakrabarti et al. 2002 (Figure taken from CGS08). The exact configuration would depend on the mass accretion rates in the two components of the flow.
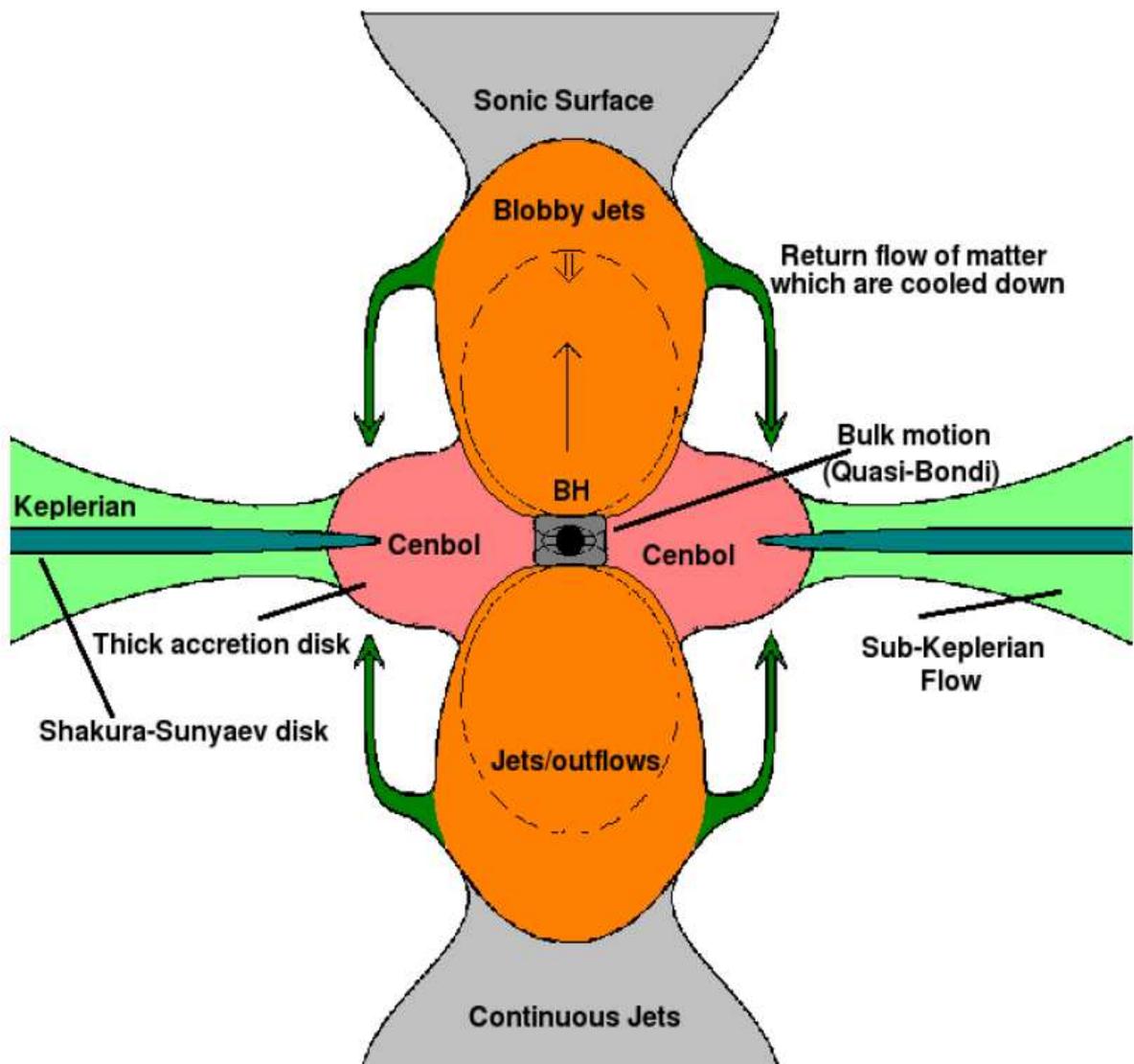
Figure 1.6: The most general type of the accretion flow which seems to encompass all the relevant flow solutions such as Bondi flow (close to black hole horizon), standard disk (on equatorial plane), Transonic sub-Keplerian flow (away from the plane) with shocks (CENBOL), Thick accretion disks (post-shock flow) and the jets and outflows from CENBOL. If the CENBOL is cooled down, then there is no outflow. If the outflows are also cooled down, some matter could fall back on the disk, giving rise to burst-on states (Chakrabarti, 2008).

1.6   Spectral and Timing Studies using TCAF

Study of spectral as well as the timing properties of the black hole candidates can only give us the vital clues of the understanding of the invisible central object. The spectrum of radiation, particularly in high energies give information about the thermodynamic properties of matter accreting onto a black hole. The timing properties give information about how these thermodynamic properties are changing with time. The thermodynamic properties such as the mass density, temperature etc. and the dynamic properties such as the velocity components are the solutions of the governing equations. Thus, a thorough knowledge about the spectral and timing properties are essential (Chakrabarti, 1996a).

CT95 and Chakrabarti (1997, hereafter C97) pointed out that the dynamic corona of a disk, namely the inner part of the sub-Keplerian flow is indeed the Compton cloud. They described that the post-shock region of a rotating sub-Keplerian flow could actually be the Compton cloud and the Keplerian flow on the equatorial plane supplies soft photons to it to be inverse Comptonized. Simply put, in this so-called two component advective flow (TCAF) model, the state of a black hole is decided by the relative importance of the processing of the *intercepted* soft photons emitted from a Keplerian disk by the puffed-up post-shock region (CENBOL) formed in the sub-Keplerian halo. The TCAF model showed that the spectral properties are direct consequences of variation of accretion rates of the Keplerian (disk) and sub-Keplerian (halo) components. If the CENBOL remains hot (generally due to smaller number of soft-photons from a Keplerian disk having lower accretion rate), and emits hard X-rays, it is the low/hard state since more power is in the hard X-ray region. On the contrary, if the CENBOL is cooled down by copious number of intercepted photons, the black hole is in the high/soft state. CT95 also pointed out that even in a high/soft state, some electrons should be energized by the momentum deposition due to the bulk motion of the electrons rushing towards the horizon. These photons would have a almost constant spectral slope. This was later verified by Monte Carlo simulations (Laurent & Titarchuk 1999; 2001).

Subsequenly, efforts were made to explain the timing properties using the TCAF model. Several numerical simulations including radiative processes (MSC96, Chakrabarti, Acharyya and Molteni 2004) indicate that the resonance effects between the cooling time scale and the infall time scale causes the shocks (Chakrabarti, 1989) to oscillate and cause the most important feature of the power density spectrum, namely, the quasi-periodic oscillations (QPOs) to appear. Thus is it generally established that the sub-Keplerian flows are responsible for both the spectral and timing properties of the black hole candidates. This is shown by several observations (Smith, Heindl, & Swank, 2002; Wu et al. 2002, Soria et al. 2001, Pottschmidt et al. 2006, Dutta

& Chakrabarti, 2010).

1.7   Relevant Radiation Mechanisms

The observed spectrum in X-ray binaries is the superposition of several spectral components originating from different regions of the system. In this Section, we will summarize the radiation emission processes in X-ray binaries (Longair, 1981; Diehl, 2001). The details of these processes will be given in Chapter 2.

- **Thermal emission**

High temperature gases can produce thermal emission in the form of a black body radiation in the X-ray regime. This situation is very common in very hot in stellar winds, accretion disks etc.

- **Compton scattering**

This is the interaction of photons with stationary electrons, in such a way that the high energy photon loses energy which is gained by the electron.

- **Inverse Compton scattering**

In this interaction photon gains energy which is lost by the very energetic particle. This scattering happens in case of the accretion disk surrounding black holes or neutron stars in X-ray binary systems due to the presence of hot ($\sim 10^9$ K) plasma which becomes highly ionized, i.e., with a large amount of highly energetic free electrons.

- **Synchrotron radiation**

Charged particles accelerate when interacting with a magnetic field. The trajectory of these particles is modified as the particle looses energy. The lost energy is emitted in the form of synchrotron radiation. The energy components perpendicular to the magnetic field are quantized. Thus, photons can be emitted or absorbed in frequencies corresponding to the energy difference between such levels, and Cyclotron emission or absorption can be produced.

- **Bremsstrahlung**

Charged particles can also interact with electrostatic fields, for example, the case of an electron passing by an ionized atom. In this case the charged particle is 'braked'

and the energy lost is emitted in the form of bremsstrahlung emission.

• Photoelectric Absorption

The atomic electrons are removed from their nuclei by the X-ray and γ-ray photons, thus the incident photon is absorbed by an electron whose binding energy was equal to the photon's energy.

In this Thesis, we consider only three types of radiative processes: thermal emission, Compton and inverse-Compton scattering.

1.8 General Relativistic and Pseudo-Newtonian Approaches

General relativity, though it is elegant and beautiful, may not be easy to use in presence of complex physical processes. In such cases, sometimes it is easy to work with pseudo-potentials. In realistic cases when heating and cooling are important, the general relativistic calculations become extremely difficult and time consuming. Under these circumstances, one easy way out is to use the so-called pseudo-Newtonian geometry. This will mimic the black hole surrounding with very little error and we can work within the realms of Newtonian physics or special relativity (as the problem may be). We will briefly describe the environment of a non-rotating black hole and the pseudo-potential which will mimic it. In this Thesis we have used this potential to take care of the general relativistic effects.

1.8.1 GR Approach

The region around a non-rotating compact object is described by the Schwarzschild metric, and is given by,

$$ds^2 = -\left(1 - 2/r\right) dt^2 + \left(1 - 2/r\right)^{-1} dr^2 + r^2 d\theta^2 + r^2 sin^2\theta d\phi^2. \tag{1.10}$$

Here, we use the spherical polar coordinate. Also we adopt units where the gravitational constant G, the central mass M and the velocity of light c are all unity ($G = M = c = 1$). Solving the geodesic equation one gets

$$-u_t = \left(1 - 2/r\right) u^t = E = \text{constant of motion} \tag{1.11}$$

and, for $\theta = \pi/2$,

$$u_\phi = r^2 u^\phi = l = \text{constant of motion}. \tag{1.12}$$

Using the above equations we can get,

$$\left(\frac{dr}{ds}\right)^2 = E^2 - \left(1 - \frac{2}{r}\right)\left(1 + \frac{l^2}{r^2}\right). \tag{1.13}$$

The second term in the RHS of Eqn. (1.13), behaves like an effective potential,

$$V_{eff}^2 = \left(1 - \frac{2}{r}\right)\left(1 + \frac{l^2}{r^2}\right). \tag{1.14}$$

The gravitational potential that a test particle around a Newtonian star feels is given by,

$$\Phi_N = -\frac{1}{r}. \tag{1.15}$$

The effective potential of a rotating gas with specific angular momentum l is obtained by the summation of the gravitational potential and the centrifugal potential.

$$V_{Newt}(r) = 1 + \Phi_N + \frac{1}{2}\frac{\ell^2}{r^2}. \tag{1.16}$$

In Fig. 1.7 we have plotted both V_{eff} and V_{Newt} against r to compare the GR potential with the Newtonian one. We see some remarkable features. First, we notice that for small r, V_{eff} dives down with decreasing r and $V_{eff} = 0$ at $r = r_g = 2$. r_g is called the event horizon or the Schwarzschild radius. Second, no matter how hard one throws a particle at a Newtonian star it will bounce back, while a black hole definitely consumes a particle if it is thrown hard enough. The particle then enters the black hole in trajectories known as 'capture orbits'. We will focus on the bound particles. Conditions for the circular orbits are: (a) $\frac{\delta V_{eff}}{\delta r} = 0$ and, (b) $\frac{dr}{ds} = 0$.

Condition (a) gives the following equation:

$$r^2 - l^2 r + 3l^2 = 0. \tag{1.17}$$

Thus, for $l \geq 2\sqrt{3}$, real values of r exists, which implies V_{eff} has an extremum for $l \geq 2\sqrt{3}$. For $l = 2\sqrt{3}$, we have the position for the *last stable orbit* or the *marginally stable orbit* (r_{ms}; shown in Fig. 1.7). Putting $l = 2\sqrt{3}$ in Eqn. (1.17), we get $r_{ms} = 6$. Imposing condition (b) in Eqn. (1.14), and using Eqn. (1.17) we get,

$$E^2 = \frac{(r-2)^2}{r(r-3)}. \tag{1.18}$$

If we take the definition of specific angular momentum as, $-u_\phi/u_t$ (Chakrabarti 1996a), the specific Keplerian angular momentum curve is the locus of the extrema of V_{eff}. Hence,

$$\lambda_{Kep}^2 = \left(-\frac{u_\phi}{u_t}\right)^2 = \frac{r^3}{(r-2)^2}. \tag{1.19}$$

Putting $r = 6$ and $l = 2\sqrt{3}$ in Eqn. (1.14), we have,

$$V_{eff}(r_{ms}) = \sqrt{\frac{8}{9}}. \tag{1.20}$$
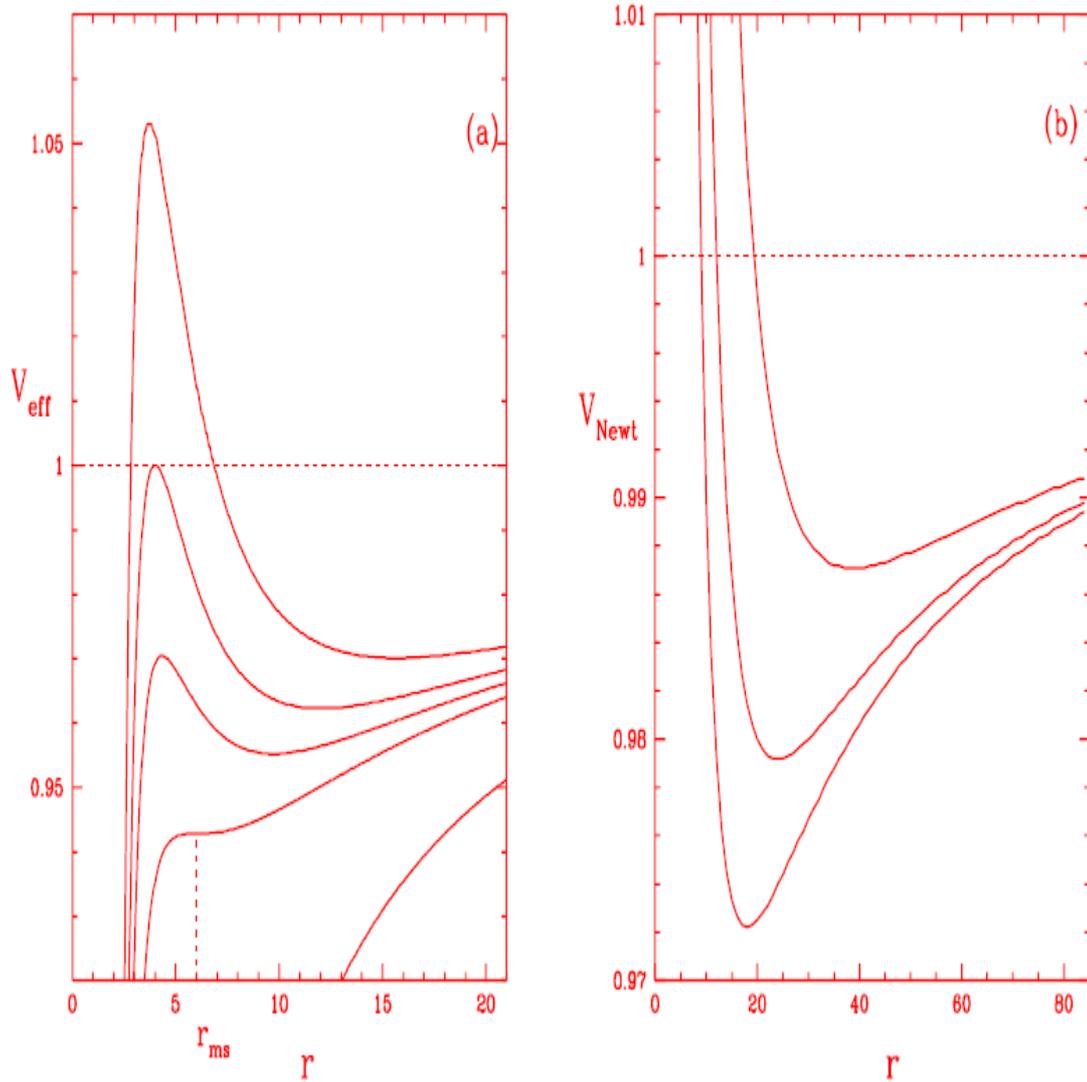
Figure 1.7: Comparison of general relativistic (a) and Newtonian (b), effective potentials. (a) The effective potential V_{eff} is drawn for the values of $l = 0$, 3.464, 3.75, 4 and 4.4, from lowest curve upwards, respectively. r_{ms} is the marginally stable radius. The dotted line for which $V_{eff} = 1$, denotes rest mass energy of particle falling into the black hole. (b) The Newtonian effective potential V_{Newt}, is drawn for the values of $\ell = 3$, 3.464 and 4.4 from the lowest curve upwards, respectively (Chattopadhyay, 2002).

Therefore, the binding energy at r_{ms} is,

$$E_{bind} = 1 - \sqrt{\frac{8}{9}} = 5.72\%. \tag{1.21}$$

When a particle enters into a black hole E_{bind} amount of energy will be liberated as radiation.

1.8.2 Pseudo-Newtonian Approach

In the case of most of the astrophysical systems involving a rotating compact star or a black hole, it is not essential that one solves the problem using full general relativity. Fortunately, a few tools are now available which allow one to use the Newtonian concepts (such as equations in flat geometry, additivity of the energy components, etc.) at the same time retaining the salient features of a black hole geometry. As long as one is not interested in processes very close (within $1 - 2r_g$) to the horizon, one may safely use these tools and obtain sufficiently accurate results. The potential we describe was proposed by PW80 and is called *Paczyński-Wiita potential*. Paczyński-Wiita potential or pseudo-Newtonian potential is given by,

$$\Phi_{PW} = -\frac{1}{(r-2)}. \tag{1.22}$$

Adding the rest mass energy to this potential and then writing the effective potential,

$$V_{eff(PW)} = 1 + \frac{\ell^2}{2r^2} + \Phi_{PW}. \tag{1.23}$$

Putting the condition $\delta V_{eff(PW)}/\delta r = 0$, we get,

$$\ell^2_{Kep} = \frac{r^3}{(r-2)^2}. \tag{1.24}$$

We find that the specific Keplerian angular momentum produced by Φ_{PW} is same as that produced by exact GR calculations. We have already seen that r_{ms} is the position of the minima of the Keplerian angular momentum. Taking the minima of Eqn. (1.24), we find, $r_{ms} = 6$.

Please note that we have used two different notations for specific angular momentum in GR (λ) and in pseudo-Newtonian (ℓ) description, only to differentiate these two approaches. The binding energy at r_{ms} in pseudo-Newtonian description is,

$$E_{bind} = 1 - V_{eff(PW)}(r_{ms}) = 6.25\%. \tag{1.25}$$

Thus, we find that the pseudo-Newtonian approach is quite accurate, and the error is within few percent. In the next Chapters, we shall use Φ_{PW} to take care of the general relativistic effects.

1.8.3   Some Remarks About Units and Dimensions

The radius of a non-rotating black hole $r_g = 2GM/c^2$ is only 3.0 km if $M = M_\odot$. A stellar mass black hole generally has $M > 3M_\odot$. Hence the radius is around 9 km. For a super-massive black hole, one can scale these numbers depending on the mass of the black hole. However, the physical processes in accretion flows generally have length scales of the order of the Schwarzschild radius and thus, it is convenient to choose this the unit of length. Similarly, it is well known that the velocity of in-falling matter through the horizon is equal to the velocity of light (Chakrabarti, 1996bc). Thus it is expected that matter and sound velocities would be of this order and thus the units may be chosen accordingly.

Keeping these in mind, we choose, $G = c = M = 1$. In this case the unit of velocity would be c, the unit of distance would be $2GM/c^2$ (the Schwarzschild radius), the unit of time would be $2GM/c^3$ and the unit of angular momentum would be $2GM/c$. In this unit system, the pseudo-Newtonian potential is written as $-\frac{1}{2(r-1)}$.

Chapter 2

Radiation Processes in Accretion Flows

We discussed that black holes can be detected by monitoring the radiations emitted by matter accreting on them. These radiations are emitted after various interactions which happen inside the infalling matter. Processes like bremsstrahlung and synchrotron radiation generate new photons. In Compton scattering, the energy exchange happens between the electrons and the photons. The flow parameters, density and scattering cross-section determine the optical depth (τ) of the medium, which determines the number of scattering inside the medium. Depending on τ, a photon can suffer a single scattering or multiple scatterings or no scattering at all inside the accretion disk which is manifested in the radiation spectrum. The radiation pressure can also affect the hydrodynamics, but presently we are not considering that effect. There are two main radiation types: thermal and non-thermal. Thermal radiation is the radiation emitted by matter satisfying Maxwell-Boltzmann thermodynamic equilibrium conditions for particle velocities. It is characterized by the temperature of the emitting gas. Black-body radiation is an example of thermal radiative process. Non-Thermal radiation is emitted by particles not in thermal equilibrium. Synchrotron, bremsstrahlung and Compton processes *could be* non-thermal radiations. Below we discuss the black body, and Compton radiation. We will not discuss about the bremsstrahlung and synchrotron processes because in this Thesis we have only considered black body, and Compton radiation. We have followed Longair (1981), Rybicki & Lightman (1979, hereafter RL79) and Poznyakov, Sobol & Syunyaev (1983, hereafter, PSS83) to write this Chapter.

2.1   Black Body Radiation

If a body is irradiated with radiation of frequency ν, and a fraction $a(\nu)$ of that radiation is absorbed and the remainder being either reflected or transmitted, $a(\nu)$ would be called the absorptance at frequency ν. The fractions of the radiation re-

flected and transmitted are called the reflectance and the transmittance respectively. The sum of the absorptance, reflectance and transmittance is unity.

A body for which $a(\nu) = 1$ for all frequencies is a black body.

Blackbody radiation is the radiation which is itself in thermal equilibrium with the surroundings. The spectral volume density of radiation energy can be determined by calculating the equilibrium distribution of photons, for which the radiation field entropy is maximum. The energy of the photon with frequency ν is equal to $h\nu$, where h is the Planck constant. Assuming the radiation field to be a gas obeying the Bose-Einstein statistics, then we obtain the Planck formula for the energy per solid angle per volume per frequency of radiation:

$$u_\nu(T, \Omega) = \frac{2h\nu^3}{c^3} \frac{1}{[exp(h\nu/k_BT) - 1]}, \qquad (2.1)$$

where k_B is the Boltzmann constant. The intensity of the black body radiation $I_\nu(T, \Omega) = u_\nu(T, \Omega) \times c$, so that

$$I_\nu(T, \Omega) = \frac{2h\nu^3}{c^2} \frac{1}{[exp(h\nu/k_BT) - 1]}, \qquad (2.2)$$

Eqn. (2.2) expresses the *Planck law*. A plot of I_ν versus ν for a range of values of T ($1 \text{ K} < T < 10^7 \text{ K}$) is given in Fig. 2.1.

• **The Rayleigh-Jeans Law** ($h\nu \ll k_BT$)**:** In this case, we can expand the exponential as,

$$exp\left(\frac{h\nu}{k_BT}\right) - 1 = \frac{h\nu}{k_BT} + ...$$

Thus, for $h\nu \ll k_BT$ range of photon energy, we have the *Rayleigh-Jeans Law*:

$$I_\nu^{RJ}(T, \Omega) = \frac{2\nu^2}{c^2} k_BT. \qquad (2.3)$$

The Rayleigh-Jeans Law is valid at low frequencies. It gives the straight-line part of the log I_ν - log ν plot in Fig. 2.1. An important feature of Eqn. (2.3) is that, if we integrate $I_\nu^{RJ}(T, \Omega)$ over all frequencies, the total energy $\propto \int \nu^2 d\nu$ will diverge. This is known as the *ultraviolet catastrophe*.

• **Wien Law** ($h\nu \gg k_BT$)**:** This limit allows us to neglect the unity term in the denominator in comparison with $exp(h\nu/k_BT)$. Thus *Wien Law* gives:

$$I_\nu^W(T, \Omega) = \frac{2h\nu^3}{c^2} exp\left(\frac{-h\nu}{k_BT}\right). \qquad (2.4)$$

The steep portions of curves in Fig. 2.1 are associated with the Wien Law.
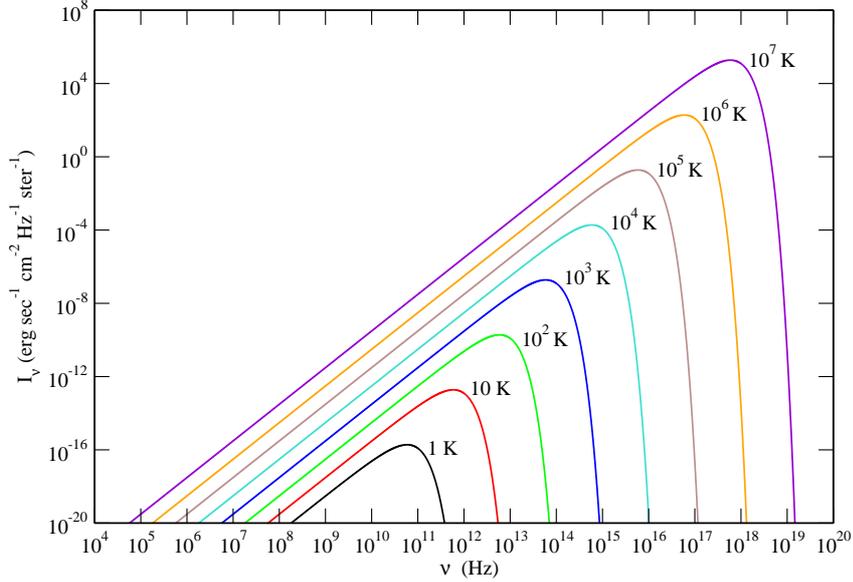
Figure 2.1: Spectrum of a blackbody radiation at various temperatures.

• **Wien Displacement Law:** The frequency ν_{max} at which the peak of I_ν occurs is given by,

$$\left[\frac{\partial I_\nu}{\partial \nu}\right]_{\nu=\nu_{max}} = 0,$$

or,

$$\frac{\nu_{max}}{T} = 5.88 \times 10^{10} \text{ Hz deg}^{-1}. \tag{2.5}$$

Eqn. (2.5) shows that the peak frequency shifts linearly with black body temperature. This is known as the *Wien Displacement Law.*

• **Number of black body photons:** Number of black body photons emitted per unit volume per solid angle per sec per frequency of radiation is given by,

$$N_\nu(T,\Omega) = \frac{u_\nu(T,\Omega)}{h\nu}.$$

Integrating over the solid angle Ω and frequency we get,

$$N(T) = \int_{\nu=0}^{\infty} \int_{\Omega} \frac{u_\nu(T,\Omega)}{h\nu} d\Omega d\nu.$$

Performing the above integration we get the total number of emitted black body
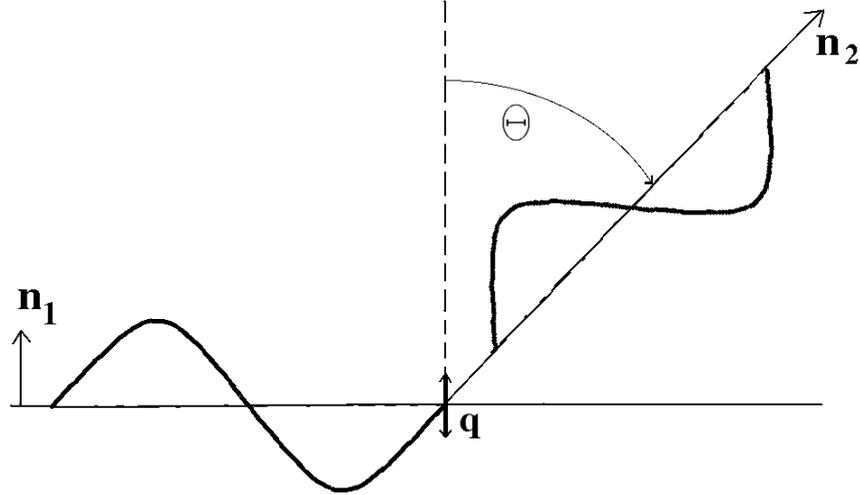
Figure 2.2: Scattering of polarized radiation by a charged particle.

photons per unit volume per sec for temperature T, as,

$$N(T) = 16\pi \times 1.202057 \times \left(\frac{k_B}{hc}\right)^3 T^3. \tag{2.6}$$

Thus, the number of photons per unit volume is proportional to the cube of the black body temperature.

2.2 Scattering Processes

2.2.1 Thomson Scattering

This is a frequency-independent nonrelativistic scattering. Suppose a lonely electron has an electromagnetic wave incident on it. The wave has a frequency ω_0. The electric force from a linearly polarized wave is

$$\mathbf{F} = qE_0 \sin \omega_0 t \mathbf{n_1},$$

where q is the charge and $\mathbf{n_1}$ is the direction of the $\mathbf{E}$-field. From the Newton's second law and the definition of the dipole moment $\mathbf{d} = q\mathbf{r}$, we get

$$\ddot{\mathbf{d}} = \frac{q^2 E_0}{m_e} \sin \omega_0 t \mathbf{n_1},$$

and

$$\mathbf{d} = -\left(\frac{q^2 E_0}{m_e \omega_0^2}\right) \sin \omega_0 t \mathbf{n_1},$$

which gives an oscillating dipole of amplitude

$$\mathbf{d_0} = \frac{q^2 E_0}{m_e \omega_0{}^2} \mathbf{n_1}.$$

Larmor's formula gives the time-averaged power per solid angle:

$$\frac{dP}{d\Omega} = \frac{q^4 E_0{}^2}{8\pi m_e{}^2 c^3} \sin^2 \Theta. \tag{2.7}$$

The incident flux is $\langle S \rangle = (c/8\pi) E_0{}^2$, so we can define a differential cross section $d\sigma$ for scattering into the solid angle $d\Omega$:

$$\frac{dP}{d\Omega} = \langle S \rangle \frac{d\sigma}{d\Omega} = \frac{c E_0{}^2}{8\pi} \frac{d\sigma}{d\Omega}. \tag{2.8}$$

Therefore, we have the relation

$$\left(\frac{d\sigma}{d\Omega}\right)_{pol} = \left(\frac{q^4}{m_e c^4}\right) \sin^2 \Theta. \tag{2.9}$$

For an electron $r_0 = q^2/m_e c^2$ is known as 'classical radius of the electron', $r_0 \approx 2.8 \times 10^{-13}$ cm. It is the radius that gives an electrostatic energy equal to $m_e c^2$. Integrating over all angles, one finds the total cross section to be

$$\sigma = \left(\frac{8\pi}{3}\right) r_0{}^2. \tag{2.10}$$

For an electron, $\sigma = \sigma_T = 6.65 \times 10^{25}\ cm^2$.

We can now compute the differential cross section for an unpolarized radiation by the superposition of two orthogonally polarized waves. If we define θ as the angle between the scattered radiation and the original radiation (so that $\theta = \pi/2 - \Theta$), we have the result

$$\left(\frac{d\sigma}{d\Omega}\right)_{unpol} = \frac{1}{2}\left[\left(\frac{d\sigma(\Theta)}{d\Omega}\right)_{pol} + \left(\frac{d\sigma(\theta)}{d\Omega}\right)_{pol}\right] = \frac{1}{2} r_0{}^2 \left(1 + \sin^2 \Theta\right) = \frac{1}{2} r_0{}^2 \left(1 + \cos^2 \theta\right). \tag{2.11}$$

From Eqn. (2.11), we find that the total cross section depends only on the angle between the incident and scattered directions, as it should be, since an electron at rest has no intrinsic polarization, so it has to react to all linear polarizations in the same way.
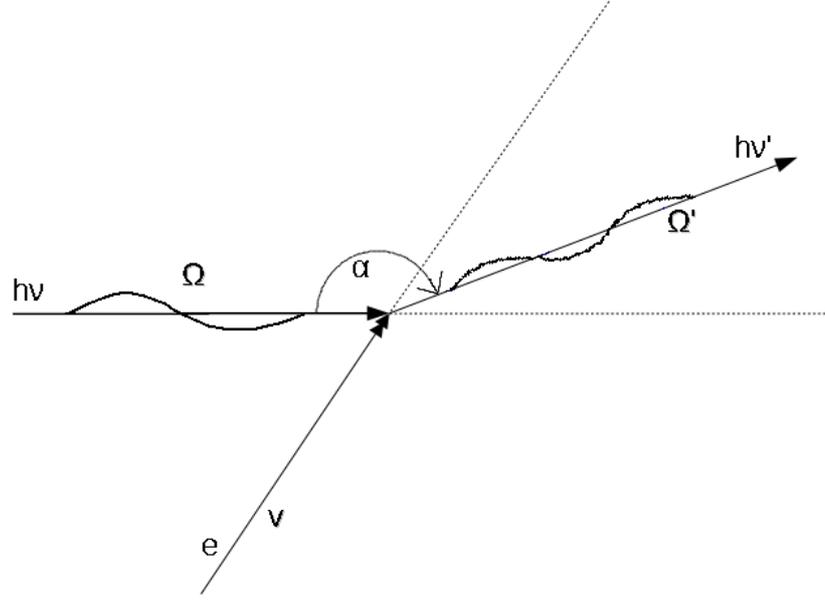
Figure 2.3: The Compton effect. A photon with energy $h\nu$ is scattered by an electron, moving with velocity **v**. The scattered photon has energy $h\nu'$ and the scattering angle is α.

2.2.2   Compton Scattering

In Thomson scattering, there is no change in the frequency of the incoming radiation. The electron simply acts as a radiator which scatters the incoming radiation. This remains a good approximation provided the energy of the photon is much less than the rest mass energy of the electron i.e., $h\nu \ll mc^2$. However for high energy of the incident photon the collision between a free electron and photon leads to a change in frequency of the photon and it has important implications in high energy astrophysics. This is known as the Compton scattering. For more detailed description one may read PSS83.

Let us consider a photon of energy $h\nu$ and momentum $\frac{h\nu}{c}\widehat{\boldsymbol{\Omega}}$ is scattered by an electron of energy γmc^2 and momentum $\overrightarrow{\mathbf{p}} = \gamma m \overrightarrow{\mathbf{v}}$, where the electron Lorentz factor $\gamma = \left(1 - \frac{v^2}{c^2}\right)^{-1/2}$. Let, $h\nu'$ and $\frac{h\nu'}{c}\widehat{\boldsymbol{\Omega'}}$ denote the energy and momentum of the photon after the scattering.

Shift in Photon Frequency

If we introduce the electron and photon four-momenta before scattering as: p_{el} and p_{ph}, respectively and p'_{el} and p'_{ph}, after the scattering, then p_{el}, p_{ph}, p'_{el}, p'_{ph} are given

by:

$$p_{el} = \left(\overrightarrow{\mathbf{p}}, i\gamma mc \right),$$

$$p_{ph} = \left(\frac{h\nu}{c} \widehat{\mathbf{\Omega}}, \frac{ih\nu}{c} \right),$$

$$p'_{el} = \left(\overrightarrow{\mathbf{p'}}, i\gamma' mc \right),$$

$$p'_{ph} = \left(\frac{h\nu'}{c} \widehat{\mathbf{\Omega'}}, \frac{ih\nu'}{c} \right).$$

Conservation of energy and momentum gives,

$$p_{el} + p_{ph} = p'_{el} + p'_{ph}. \tag{2.12}$$

Squaring this relation and noting that:

$$p_{el}{}^2 = p'_{el}{}^2 = -m^2 c^2,$$

and,

$$p_{ph}{}^2 = p'_{ph}{}^2 = 0,$$

we find,

$$p_{el}p_{ph} = p'_{el}p'_{ph}. \tag{2.13}$$

Now, multiplying Eqn. (2.12) by p'_{ph} we find

$$p'_{el}p'_{ph} = p_{el}p'_{ph} + p_{ph}p'_{ph}. \tag{2.14}$$

Using Eqn. (2.13) we rewrite Eqn. (2.14) as:

$$p_{el}p_{ph} = p_{el}p'_{ph} + p_{ph}p'_{ph}. \tag{2.15}$$

Defining $\mu = \widehat{\mathbf{\Omega}}.\widehat{\mathbf{v}}$, $\mu' = \widehat{\mathbf{\Omega'}}.\widehat{\mathbf{v}}$, and the scattering angle $\alpha = \cos^{-1}\left(\widehat{\mathbf{\Omega}}.\widehat{\mathbf{\Omega'}} \right)$, we may write from Eqn. (2.15),

$$\frac{\nu'}{\nu} = \frac{1 - \mu v/c}{1 - \mu' v/c + (h\nu/\gamma mc^2)(1 - \cos\alpha)}. \tag{2.16}$$

If the photon is scattered by an electron at rest ($v = 0$), its frequency will change solely because of *recoil* effect of the electron:

$$\frac{\nu'}{\nu} = \frac{1}{1 + (h\nu/mc^2)(1 - \cos\alpha)}. \tag{2.17}$$

In the case of a photon with $h\nu \ll mc^2$ we will have

$$\frac{\Delta\nu}{\nu} = -\frac{h\nu}{mc^2}\left(1 - \cos\alpha\right).$$

If instead the electrons are traveling at high speed, the *Doppler effect* will play the dominant role in changing the frequency of low-energy photons. For a reference frame comoving with the scattering electron, the photon frequency prior to the scattering event will be

$$\nu_0 = \gamma\nu\left(1 - \frac{\mu\nu}{c}\right),$$

and if $h\nu_0 \ll mc^2$, we can assume that there is no change in scattered photon energy in the electron rest frame: $\nu'_0 \approx \nu_0$. When this condition is satisfied, the scattering is closely elastic. Reverting to the laboratory reference frame, we obtain

$$\nu' = \frac{\nu'_0}{\gamma\left(1 - \mu'\nu/c\right)} \approx \frac{\nu_0}{\gamma\left(1 - \mu'\nu/c\right)} = \nu.\frac{\left(1 - \mu\nu/c\right)}{\left(1 - \mu'\nu/c\right)}, \tag{2.18}$$

which will agree with Eqn. (2.16) if the condition $h\nu/\gamma mc^2 \ll 1$ holds. In the nonrelativistic limit $v/c \ll 1$, Eqn. (2.18) gives

$$\frac{\nu' - \nu}{\nu} = \frac{v}{c}\left(\mu' - \mu\right) + \frac{v^2}{c^2}\mu'^2. \tag{2.19}$$

Scattering Cross Section

The differential cross section for Compton scattering can be calculated using quantum electrodynamics and is expressed by the formula:

$$\frac{d\sigma}{d\Omega'} = \frac{r_e^2}{2\gamma^2}\frac{X}{\left(1 - \mu\nu/c\right)^2}\left(\frac{\nu}{\nu'}\right)^2, \tag{2.20}$$

where the function

$$X = \frac{x}{x'} + \frac{x'}{x} + 4\left(\frac{1}{x} - \frac{1}{x'}\right) + 4\left(\frac{1}{x} - \frac{1}{x'}\right)^2, \tag{2.21}$$

$$x = \frac{2h\nu}{mc^2}\gamma\left(1 - \mu\frac{v}{c}\right), \tag{2.22}$$

$$x' = \frac{2h\nu'}{mc^2}\gamma\left(1 - \mu'\frac{v}{c}\right). \tag{2.23}$$

For the case, $\nu \sim \nu'$ Eqn. (2.20) reduces to the classical expression. Thus, in the nonrelativistic limit,

$$\frac{d\sigma}{d\Omega'} = \frac{r_e^2}{2}\left(1 + cos^2\alpha\right). \tag{2.24}$$

Here, $r_e = e^2/mc^2$ is the classical electron radius. So, we find that the cross section reduces from its classical value for larger photon energy. Thus Compton scattering becomes less efficient at high energies. The total scattering cross section is given by Klein-Nishina formula:

$$\sigma = \frac{2\pi r_e^2}{x} \left[\left(1 - \frac{4}{x} - \frac{8}{x^2} \right) ln\,(1+x) + \frac{1}{2} + \frac{8}{x} - \frac{1}{2\,(1+x)^2} \right]. \qquad (2.25)$$

In the nonrelativistic limit $(x \ll 1)$ we have approximately

$$\sigma \approx \frac{8\pi}{3} r_e^2 (1 - x) = \sigma_T (1 - x), \qquad (2.26)$$

while in the ultrarelativistic regime $(x \gg 1)$ we have

$$\sigma = 2\pi r_e^2 x^{-1} \left(lnx + \frac{1}{2} \right). \qquad (2.27)$$

Here, σ_T is the Thomson scattering cross section for an electron, given by Eqn. (2.10).

Photon Free Path

The probability that a photon will be scattered within a path length dl by a directed beam of electrons having a density $N_e(\tilde{\mathbf{v}})$ and moving at velocity $\vec{v}$ is expressed by (Landau and Lifshitz, 1976)

$$d\pi = \left(1 - \mu\frac{v}{c} \right) \sigma(x) N_e(\tilde{\mathbf{v}}) dl. \qquad (2.28)$$

From the scattering probability we can calculate the mean free path $\overline{\lambda}$ of a photon in plasma whose electrons have any desired isotropic distribution $N_e(\tilde{\mathbf{v}})$ with respect to momentum:

$$\overline{\lambda} = \frac{4\pi \int_0^\infty N_e(p)p^2 dp}{2\pi N_e \int_0^\infty N_e(p)p^2 \int_1^{-1} \sigma(x) \left(1 - \mu\frac{v}{c} \right) d\mu dp}. \qquad (2.29)$$

Now we evaluate the expression (2.29) for a Maxwellian gas.

• **Nonrelativistic limit $(h\nu \ll mc^2,\ k_B T_e \ll mc^2)$:** The Maxwellian momentum distribution gives:

$$N_e(p) = N_e \left(\frac{1}{2\pi mk_B T_e} \right)^{3/2} exp \left(-\frac{p^2}{2mk_B T_e} \right). \qquad (2.30)$$

Substituting Eqns. (2.30) and (2.26) into Eqn. (2.29), we find that

$$\frac{1}{\overline{\lambda}} = \sigma_T N_e \left[1 - 2\frac{h\nu}{mc^2} - 5 \left(\frac{h\nu}{mc^2} \right) \left(\frac{k_B T_e}{mc^2} \right) \right]. \tag{2.31}$$

• **Ultrarelativistic limit** $(h\nu \gg mc^2,\ k_B T_e \gg mc^2)$**:** The probability distribution for the momentum in this relativistic Maxwellian electron gas is given by the Maxwell-Juttner distribution:

$$N_e(p) = exp \left(-\frac{(p^2 c^2 + m^2 c^4)^{1/2}}{k_B T_e} \right). \tag{2.32}$$

Now, if we substitute Eqn. (2.32) into Eqn. (2.29) and write the cross section from Eqn. (2.27), we find that

$$\frac{1}{\overline{\lambda}} = \frac{3}{16}\sigma_T N_e \frac{mc^2}{h\nu} \frac{mc^2}{k_B T_e} \left[\ln \left(4\frac{h\nu}{mc^2} \frac{k_B T_e}{mc^2} \right) + 0.077 \right]. \tag{2.33}$$

• **Limit** $h\nu \gg mc^2$ **but** $k_B T_e \ll mc^2$**:** In this limit we will have,

$$\frac{1}{\overline{\lambda}} = \frac{3}{8}\sigma_T N_e \frac{mc^2}{h\nu} \left(\ln \frac{2h\nu}{mc^2} + 0.5 + \frac{k_B T_e}{mc^2} \right) \left(1 - \frac{3}{2}\frac{k_B T_e}{mc^2} \right). \tag{2.34}$$

We find that the mean free path $\overline{\lambda}$ with respect to Compton scattering will lengthen as the Maxwellian plasma temperature $(k_B T_e)$.

Energy Exchange between Plasma and Radiation during Scattering

When photons are scattered by electrons with a Maxwellian momentum distribution, the average relative change in the photon frequency per scattering will be

$$\frac{\overline{\Delta\nu}}{\nu} = \overline{\lambda} \int \left(\frac{\nu'}{\nu} - 1 \right) \left(1 - \mu\frac{v}{c} \right) \frac{d\sigma}{d\Omega'} N_e(p) p^2 dp d\Omega d\Omega', \tag{2.35}$$

where, $\frac{\nu'}{\nu}$ is expressed by Eqn. (2.16) and the photon mean free path $\overline{\lambda}$ by Eqn. (2.29).

For nonrelativistic electrons in thermal equilibrium, Eqn. (2.35) gives:

$$\left[\frac{<\nu' - \nu>}{\nu} \right]_{NR} = \frac{4k_B T_e - h\nu}{mc^2}. \tag{2.36}$$

If $k_B T_e > h\nu$, the photons may gain energy from the electrons. This is called *inverse Compton scattering.* On the other hand, for $h\nu > 4k_B T_e$, energy is transferred from photons to electrons via Compton scattering.

For ultrarelativistic limit, $\gamma \gg 1$, Eqn. (2.35) becomes,

$$\left[\frac{< \nu' - \nu >}{\nu} \right]_R \sim 16 \left(\frac{k_B T_e}{mc^2} \right)^2. \tag{2.37}$$

Compton Y Parameter

The spectrum resulting from repeated scatterings is usually calculated numerically using Monte Carlo techniques. Qualitatively, however, we can expect that the more scatterings that occur, the more the seed photon distribution becomes distorted. A useful parameter that measures the importance of scattering in a medium is the Compton Y parameter:

$Y \equiv$ (average fractional energy change per scattering) $\times$ (mean number of scattering).

The Y parameter in a finite media determines whether a photon will significantly change its energy in traversing the medium.

The mean number of scatterings is determined by the optical depth, $\tau = \sigma N_e D$, where D is the dimension of the scattering region. A value of $\tau \sim 1$ means that on average, a photon will scatter once before escaping the region. It can be shown that, the mean number of scatterings N_s is given by,

$$N_s \approx \tau^2, \qquad (\tau \gg 1),$$

and for a optically thin medium,

$$N_s \approx \tau, \qquad (\tau \ll 1).$$

For an order of magnitude estimate in a pure scattering medium it is sufficient to use:

$$N_s \approx \text{Max}(\tau, \tau^2). \tag{2.38}$$

Combining Eqns. (2.36), (2.37) and (2.38) we obtain expressions for the Compton Y parameter for relativistic and nonrelativistic thermal distribution of electrons:

$$Y_{NR} = \left[\frac{< \nu' - \nu >}{\nu} \right]_{NR} \times N_s = \frac{4k_B T_e - h\nu}{mc^2} \text{Max}(\tau, \tau^2), \tag{2.39a}$$

$$Y_R = \left[\frac{< \nu' - \nu >}{\nu} \right]_R \times N_s = 16 \left(\frac{k_B T_e}{mc^2} \right)^2 \text{Max}(\tau, \tau^2). \tag{2.39b}$$

Chapter 3

Monte Carlo Techniques

3.1   Introduction

Since the discovery of X-ray and γ-ray sources of cosmic origin, astrophysicists have tried to develop models that would explain the observed radiation spectra. The simplest model of a compact X-ray source is a cloud of hot plasma with a low-frequency ν photon source within it. The photons energy $h\nu$ is increased due to multiple scattering by hot electrons and it emerges from the cloud as hard X-ray or even γ-ray radiation. This change in the photon spectrum due to multiple scattering of photons by thermal electrons is called the *Comptonization* of radiation. This process is one of the chief mechanisms for producing hard radiation spectra in high-energy astrophysics. Radiation spectra of various compact sources (neutron stars, accretion disks around black holes, quasars, galactic nuclei, etc.) may be considered to be produced by Comptonization. The most efficient method for modeling such spectra is the Monte Carlo method.

The Monte Carlo method is a numerical method of solving mathematical problems by simulation of random variables. The Monte-Carlo method was conceived at the Los Alamos National Laboratory during the Manhattan Project by Nicholas Metropolis and S. Ulam, as a numerical method for solving the Boltzmann equation governing the neutron distribution function in fissile material. Since then it has found numerous other uses across many fields of science. To write this Chapter we have followed the books by: I. M. Sobol (1994) and Pozdnyakov, Sobol & Syunyaev (1983) (PSS83).

3.2   Modeling Random Variables

Before attempting to cope with specific problems by the Monte Carlo method one must describe how to model various random variables on a computer. Usually, three

means for obtaining random variables are considered: tables of random numbers, random number generators and the pseudo-random number method. In developing our Monte Carlo code we have used the pseudo-random number method to model the random variables. Here we give a brief description of the method.

3.2.1   Pseudo-random Numbers

A sequence of independent values $y_1, y_2, ...$ of the random variable y distributed uniformly on the interval $(0, 1)$ are called ordinary *random numbers*. Since the "quality" of random numbers used for computations is checked by special tests, one can ignore the means by which random numbers are produced, as long as they satisfy the tests.

Numbers obtained by a formula that simulate the values of the random variable y are called *pseudo-random numbers*. The word "simulate" means that these numbers satisfy a set of tests just as if they were independent values of y.

The advantages of the pseudo-random number method are evident. First, obtaining each number requires only a few simple operations, so the speed of generating numbers is of the same order as the computers work speed. Second, the program occupies only a few addresses in the RAM. Third, any of the numbers y_k can be reproduced easily. And finally, the "quality" of this sequence need to be checked only once; after that, it can be used many times in calculations of similar problems without taking any risk.

The single shortcoming of the method is the limited supply of pseudo-random numbers that it gives, since if the sequence of numbers $y_1, y_2, ...y_k, ...$ is computed by an algorithm of the form $y_k = F(y_{k-1})$ it must be periodic. In any address in RAM only a finite number of different numbers can be written. Thus, sooner or later one of the numbers, say y_L, will coincide with one of the preceding numbers, say y_l. Then clearly, $y_{L+1} = y_{l+1}, y_{L+2} = y_{l+2}, ...,$ so that there is a period $P = L - l$. The non periodic part of the sequence is $y_1, y_2, ...y_{L-1}$.

The most widespread procedure for obtaining pseudo-random numbers is the method of residues (also called the congruential method or the multiplicative method) proposed by D. H. Lehmer.

- **Method of residues**

A sequence of integers m_k is defined in which the initial number m_0 is fixed, and all subsequent numbers $m_1, m_2, ...$ are computed by one formula:

$$m_k \equiv gm_{k-1} \, (mod M) , \tag{3.1}$$

for $k = 1, 2, ...$; from the numbers m_k we calculate the pseudo-random numbers

$$y_k = \frac{m_k}{M}. \tag{3.2}$$

The integer g is called *multiplier*, and the integer M is referred to as the *modulus*.

Ordinary congruential generators are not suitable in our case: if the modulus is small, the period is small. It was proposed by Wichman and Hill to use in parallel three very short number generators,

$$m_k \equiv 171 m_{k-1} \, (mod\, 30269) \,,$$

$$m'_k \equiv 172 m'_{k-1} \, (mod\, 30307) \,,$$

$$m''_k \equiv 170 m''_{k-1} \, (mod\, 30323) \,, \tag{3.3}$$

and to consider as pseudo-random numbers the fractional parts

$$y_k = \left[\frac{m_k}{30269} + \frac{m'_k}{30307} + \frac{m''_k}{30323} \right]. \tag{3.4}$$

This is how the pseudo-random numbers have been computed in our investigations. The period of the sequence y_k is $P \approx 6.9 \times 10^{12}$. The initial values m_0, m'_0, m''_0 should not be selected at random. A good sequence can be obtained with $m_0 = 11$, $m'_0 = 23$, $m''_0 = 101$.

3.2.2   Method of Inverse Functions

This method is one of the basic procedures for modeling random variables. Here we want to find the values of a random variable whose distribution function is $F(x)$. Let $x = G(y)$ be the function inverse to the function $y = F(x)$; then the expression $\eta = G(\xi)$ will define a random variable with the distribution function $F(x)$.

Example 1: The free path λ of a photon in a homogeneous medium is a random variable conforming to the exponential law

$$P\{\lambda < x\} = 1 - e^{-x/\overline{\lambda}},$$

where $\overline{\lambda}$ is the mean free path. The method of inverse functions gives:

$$\xi = 1 - e^{-x/\overline{\lambda}},$$

$$\Rightarrow x = -\overline{\lambda}\ln(1 - \xi).$$

Since the random variable ξ and $1 - \xi$ has the same distribution, the expression for modeling the free path of an individual photon is given by:

$$\lambda = -\overline{\lambda} \ln(\xi).$$

Example 2: *Energy of Power-law photons or electrons:* Let us have a Power law energy distribution $F(E) = E^{-\alpha}$ between E_1 to E_2. The random variable whose values will be between E_1 and E_2 and satisfies the power law distribution function is given by:

$$\frac{\int_{E_1}^{E} F(E) dE}{\int_{E_1}^{E_2} F(E) dE} = \xi, \tag{3.5}$$

where, ξ is the random number distributed uniformly on the interval $(0, 1)$. From this equation we obtain the modeling expression:

$$E = \left[\xi \left(E_2^{1-\alpha} - E_1^{1-\alpha} \right) + E_1^{1-\alpha} \right]^{\frac{1}{1-\alpha}}. \tag{3.6}$$

3.2.3 Rejection Technique

Consider a random variable η defined by the condition

$$\eta = g(y_1, y_2, ..., y_m) \qquad \text{if} \qquad (y_1, y_2, ..., y_m) \in B, \tag{3.7}$$

where, B is some fixed region in $m-$dimensional space. To compute η from expressions of the type (3.7) we choose m random numbers $y_1, y_2, ..., y_m$ and test the selection criterion $(y_1, y_2, ..., y_m) \in B$. If it is satisfied, we compute $\eta = g(y_1, y_2, ..., y_m)$; otherwise we take a new group of random numbers $y_1, y_2, ..., y_m$ and test the criterion again.

Example: Let us consider a function $f(x)$ with two important properties: (i) $f(x)$ is single valued, and (ii) for each value of x we should have finite value of $f(x)$. To compute $f(x)$ we choose two random numbers ξ and μ uniform between $(0, 1)$. Any general point x, y can be written as,

$$x = x_1 + (x_2 - x_1)\xi,$$

$$y = y_1 + (y_2 - y_1)\mu,$$

where, y_1 and y_2 are respectively the minimum and maximum values of $f(x)$ in the region x_1 and x_2 (Fig. 3.1). Now if $y \leq f(x)$ we choose that x, otherwise if $y > f(x)$ we reject that value of x and again take new set of ξ and μ to repeat the process.
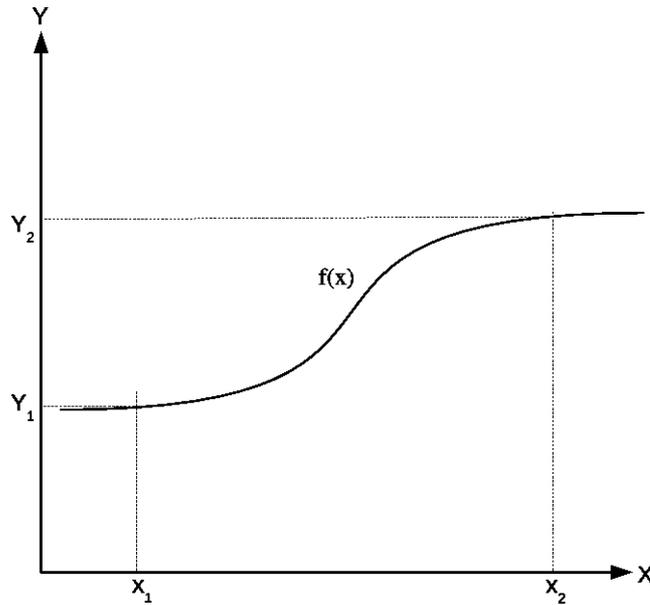
Figure 3.1: Schematic diagram to understand the rejection technique. Using this technique, one can choose random values of x between (x_1, x_2) according to the function $f(x)$.

3.2.4   Method of Superposition

Let us obtain values of a random variable η whose distribution function $F(x)$ can be represented as a superposition of distribution functions $F_m(x)$:

$$F(x) = \sum c_m F_m(x),$$

where all the $c_m > 0$, and $\sum c_m = 1$ (either finite or infinite number of terms). Let, $G_m(y)$ is the function inverse to $y = F_m(x)$. We introduce the random number α, which may take the values $\alpha = 1, 2, ...$ with probabilities $P\{\alpha = m\} = c_m$. To draw the values of η we use the following procedure:

We select two random numbers ξ_1, ξ_2, and using ξ_1 we draw a number α. From ξ_2 we now find the value of $\eta = G_\alpha(\xi_2)$. The distribution function of η will then be $F(x)$.

Example: Let us assume that the injected spectrum has two components: the Planck spectrum and the Power-Law spectrum. Also consider that n_1 and n_2 are the number of photons coming out of the source obeying Planck law and Power-law respectively (Fig. 3.2). We define the coefficient $\epsilon = \frac{n_1}{n_1+n_2}$. Now we choose a uniform random number ξ between $(0, 1)$.
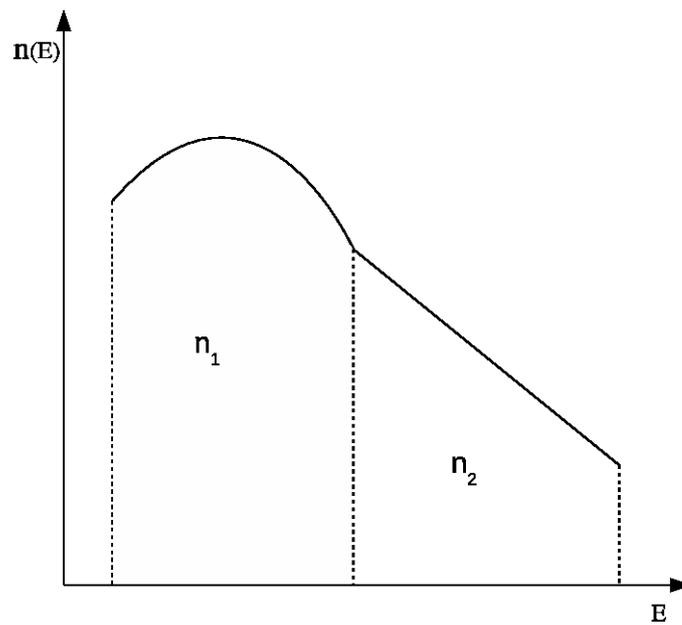
Figure 3.2: Schematic diagram to understand the method of superposition. See text for details.

<div align="center">

If, $\xi \leq \epsilon$ Planck spectrum,

If, $\xi > \epsilon$ Power Law.

</div>

In a similar way described above, we can take into account more than one physical process (e.g., pair production + Compton scattering). Here we have to consider the scattering cross sections of the processes. We have to define $\epsilon = \frac{\sigma_1}{\sigma_1 + \sigma_2}$.

<div align="center">

If, $\xi \leq \epsilon$ Process 1,

If, $\xi > \epsilon$ Process 2.

</div>

3.2.5   Multidimensional Modeling Functions

Rich opportunities are available in the simulation of random variables if we take advantage of a more general type of modeling function: $\eta = g(\xi_1, \xi_2), \eta = g(\xi_1, \xi_2, \xi_3), ...$

In general flows, the time intervals are independent random variables η with density

$$p(x) = \frac{a^m}{(m-1)!} x^{m-1} e^{-ax}, \qquad\qquad 0 < x < \infty. \qquad\qquad (3.8)$$

Since the integral

$$\Gamma(m) = \int_0^\infty x^{m-1} e^{-x} dx = (m-1)!$$

is called the *gamma-function*, the density (3.8) is called the *gamma-distribution*. It can be proved that for integers $m = n$ the random variable η, with density (3.8) can be modeled by the equation

$$\eta = -a^{-1} \ln(\xi_1, ..., \xi_n), \qquad\qquad (3.9)$$

while for half-integers $m = n + \frac{1}{2}$ the modeling formula becomes

$$\eta = -a^{-1} \left[\ln(\xi_1, ..., \xi_n) + (\ln \xi_{n+1}) \sin^2(2\pi \xi_{n+2}) \right]. \qquad\qquad (3.10)$$

3.3   Application of the Monte Carlo Technique to the Comptonization Problem

3.3.1   Energy of Planck Photons

At radiation temperature T_r the number density of photons having an energy $E = h\nu$ is expressed by

$$p(E) = \frac{1}{2\zeta(3)} b^3 E^2 (e^{bE} - 1)^{-1}, \qquad\qquad (3.11)$$

where $b = 1/k_B T_r$; $\zeta(3) = \sum_1^\infty m^{-3} = 1.202$ is the Riemann zeta function. The function $(e^{bE} - 1)^{-1}$ can be expanded in powers of e^{-bE}. Using the normalized densities

$$p_m(E) = \frac{1}{2} m^3 b^3 E^2 e^{-bmE}, \qquad\qquad (3.12)$$

we can rewrite $p(E)$ as,

$$p(E) = (1.202)^{-1} \sum_{m=1}^\infty m^{-3} p_m(E). \qquad\qquad (3.13)$$

This expression shows that $p(E)$ may conveniently be modeled by the superposition method: each of the densities $p_m(E)$ represents a gamma distribution (given in

Eqn. (3.8)) and would be modeled by the formula (3.16) (as from Eqn. (3.11) we see $m = 3$, an integer).

To draw a value for the energy $E = h\nu$ we select four random numbers $\xi_1, \xi_2, ..., \xi_4$. From ξ_1 we define an auxiliary random number α such that

$$\alpha = 1 \qquad \text{if} \qquad 1.202\xi_1 < 1, \tag{3.14}$$

$$\alpha = m \qquad \text{if} \qquad \sum_1^{m-1} j^{-3} \leq 1.202\xi_1 < \sum_1^m j^{-3}, \tag{3.15}$$

where $m = 2, 3, ...$; then from Eqn. (3.9) we set

$$h\nu = -\frac{k_B T_r}{\alpha} \ln(\xi_2 \xi_3 \xi_4). \tag{3.16}$$

3.3.2   Momentum of Relativistic Electrons

The number of Maxwellian electrons having momentum $\vec{p}$ is expressed by Eqn. (2.65)

$$N(\vec{p})d\vec{p} = exp[-(p^2 c^2 + m^2 c^4)^{1/2}/k_B T_e]d\vec{p}. \tag{3.17}$$

If all directions $\vec{p}$ are equally probable, the density of p will be proportional to

$$p^2 exp[-(p^2 c^2 + m^2 c^4)^{1/2}/k_B T_e].$$

Introducing the dimensionless energy $n = k_B T_e/mc^2$ and momentum $\eta = p/mc$, we have for density of η:

$$p(x) = B_2 x^2 exp\left(-\frac{1}{n}\sqrt{1 + x^2}\right), \tag{3.18}$$

where $0 < x < \infty$ and the normalizing constant B_2 is given in terms of the Macdonald function by

$$B_2 = \left[nK_2\left(\frac{1}{n}\right)\right]^{-1}.$$

- **Low-temperature case**

If $n \leq 0.29$ (equivalently, if $k_B T_e \leq 150$ keV), we select two random numbers ξ_1, ξ_2 and compute the auxiliary quantity

$$\xi' = -\frac{3}{2} \ln \xi_1.$$

Then if the selection criterion

$$\xi_2^2 < 0.151 \left(1 + n\xi'\right)^2 \xi' \left(2 + n\xi'\right) \xi_1,$$

is satisfied, we set

$$\eta = \left[n\xi' \left(2 + n\xi'\right)\right]^{1/2};$$

otherwise, we select new ξ_1, ξ_2.

- **High-temperature case**

For $n > 0.29$, or equivalently, for $k_B T_e \geq 150$ keV we select four random numbers $\xi_1, ..., \xi_4$ and compute the two quantities

$$\eta' = -n \ln(\xi_1 \xi_2 \xi_3),$$

$$\eta'' = -n \ln(\xi_1 \xi_2 \xi_3 \xi_4).$$

If $(\eta'')^2 - (\eta')^2 > 1$ we set $\eta = \eta'$; otherwise we draw new numbers $\xi_1, ..., \xi_4$.

3.3.3   Scattering Cross Section

The cross section

$$\sigma(x) = 2\pi r_e^2 \widehat{\sigma}(x), \tag{3.19}$$

for scattering of a photon by an electron is well established, but the conventional equation (Eqn. 2.61),

$$x\widehat{\sigma}(x) = \left(1 - \frac{4}{x} - \frac{8}{x^2}\right) \ln(1 + x) + \frac{1}{2} + \frac{8}{x} - \frac{1}{2(1 + x)^2}, \tag{3.20}$$

is inconvenient for calculations when $x \ll 1$ and is rather cumbersome to integrate. We therefore approximate $\widehat{\sigma}(x)$ to high accuracy by means of the simpler functions

$$\widehat{\sigma}(x) = \frac{1}{3} + 0.141x - 0.12x^2 + (1 + 0.5x)(1 + x)^{-2}, \qquad x \leq 0.5;$$

$$= [\ln(1 + x) + 0.06]x^{-1}, \qquad\qquad 0.5 \leq x \leq 3.5;$$

$$= [\ln(1 + x) + 0.5 - (2 + 0.076x)^{-1}]x^{-1}, \qquad 3.5 \leq x. \tag{3.21}$$

The error of this fit is no more than 1 percent. We need to evaluate the following function:

$$\Phi(x) = \int_0^x x\widehat{\sigma}(x)dx. \tag{3.22}$$

By integrating the approximations to $x\hat{\sigma}(x)$ we obtain the computation formulas

$$\Phi(x) = \frac{1}{6}x^2 + 0.047x^3 - 0.03x^4 + \frac{1}{2}x^2(1+x)^{-1}, \qquad 0 \le x \le 0.5;$$

$$= (1+x)\ln(1+x) - 0.94x - 0.00925, \qquad 0.5 \le x \le 3.5;$$

$$= (1+x)\ln(1+x) + 0.5x - 13.16\ln(2+0.076x) + 9.214, \qquad 3.5 \le x. \quad (3.23)$$

3.3.4   Photon Mean Free Path

A photon of energy $h\nu$ and with its momentum in direction Ω will have a mean free path given by Eqn. (2.65), where the scattering cross section $\sigma(x)$ and the function $N(\vec{p})$ have been defined above (Eqn. (3.20) and (3.17), respectively). Here,

$$x = H\gamma(1 - \hat{\Omega}.\vec{v}/c), \qquad (3.24)$$

with $H = 2h\nu/mc^2$. Since all directions of $\vec{p}$ are equally probable, we align the polar axis with $\hat{\Omega}$ and introduce spherical coordinates p, θ, ϕ to obtain the expression:

$$\bar{\lambda} = \frac{4\pi \int_0^\infty e^{-\gamma/n}p^2 dp}{2\pi N_e \int_0^\infty e^{-\gamma/n}p^2 dp \int_{-1}^1 \sigma(x)\left[1 - (v/c)\cos\theta\right]d(\cos\theta)}. \qquad (3.25)$$

The integration over $\cos\theta$ is readily converted to an integration over x, because if γ is fixed, $dx = -H\gamma(v/c)d\cos\theta$. Then we find that

$$\int_{-1}^1 \sigma(x)\left[1 - (v/c)\cos\theta\right]d(\cos\theta) = \frac{2\pi r_e^2}{(H\gamma)^2 v/c}\int_{H\gamma(1-v/c)}^{H\gamma(1+v/c)} x\hat{\sigma}(x)dx,$$

$$= \frac{2\pi r_e^2}{H^2\gamma\sqrt{\gamma^2-1}}\left[\Phi(x)\right]_{H\gamma^-}^{H\gamma^+}, \qquad (3.26)$$

where $\gamma^\pm = \gamma \pm \sqrt{\gamma^2-1}$. We substitute this expression into Eqn. (3.25) with

$$\pi r_e^2 N_e = \frac{3}{8}\sigma_T N_e = 0.375\sigma_T N_e, \qquad (3.27)$$

and change from an integration over p to an integration over γ (using, $p = mc\sqrt{\gamma^2-1}$). As a result we finally obtain the mean free path:

$$\bar{\lambda} = \frac{H^2 \int_1^\infty e^{-\gamma/n}\gamma\sqrt{\gamma^2-1}d\gamma}{0.375\sigma_T N_e \int_1^\infty e^{-\gamma/n}\left[\Phi(x)\right]_{H\gamma^-}^{H\gamma^+}d\gamma}. \qquad (3.28)$$

Both the integrals (numerator and denominator) are of the form

$$\int_1^\infty e^{-\gamma/n} \Psi(\gamma) d\gamma.$$

The change of variables

$$u = exp[(1 - \gamma)/n]$$

transforms the semi axis $(1, \infty)$ into the interval $(0, 1)$, and the resulting integral can be calculated from the rectangle formula:

$$\int_1^\infty e^{-\gamma/n} \Psi(\gamma) d\gamma = n e^{-1/n} \int_0^1 \Psi(1 - n \ln u) du$$

$$\approx \frac{n e^{-1/n}}{N_1} \sum_{m=1}^{N_1} \Psi \left(1 - n \ln \frac{m - \frac{1}{2}}{N_1} \right). \tag{3.29}$$

The factor $ne^{-1/n}$ occurs in both integrals and cancels out.

The final computation formulas are as follows: a) Abscissas of integration

$$\gamma_m = 1 - n \ln \left[(m - \frac{1}{2})/N_1 \right], m = 1, 2, ..., N_1. \tag{3.30}$$

b) The constant quantity

$$g = \frac{1}{0.375 \sigma_T N_e} \sum_{m=1}^{N_1} \gamma_m \sqrt{\gamma_m^2 - 1}. \tag{3.31}$$

c) The general equation

$$\bar{\lambda} = \frac{g H^2}{\sum_{m=1}^{N_1} [\Phi(x)]_{H\gamma_m^-}^{H\gamma_m^+}}. \tag{3.32}$$

d) Case $H \ll 1$: As $H \to 0$ the Eqn. (3.32) reduces to an indeterminate form, with $\lim_{H \to 0} \bar{\lambda} = (\sigma_T N_e)^{-1}$. As $\sigma(x) = \frac{1}{\bar{\lambda} \sigma_T N_e}$ so for $H \ll 1$, $\sigma(x) = 1$. Therefore, if the largest abscissa used in the numerical integration, $\gamma_1 = 1 + n \ln(2N_1)$, and the energy $H = 2h\nu/mc^2$ satisfy the condition

$$2\gamma_1 H \leq 0.01,$$

or equivalently,

$$h\nu \leq \frac{0.01 mc^2}{4\gamma_1}, \tag{3.33}$$

then we set $\sigma(x) = 1$. In our calculations we have adopted the value $N_1 = 300$.

3.3.5   Modeling Compton Scattering

• Selection of scattering electron

The probability density of the momenta $\vec{p}$ of the scattering electrons is proportional to the quantity $\sigma(x)(1 - \hat{\Omega}.\vec{v}/c)N(\vec{p})$ appearing in the Eqn. (3.25). In Sec. 3.3 we have modeled the momentum $\vec{p}$ for a Maxwellian density. After computing $\vec{v}$, x, and $\hat{\sigma}(x)$ (Sec. 3.3), we take one random number ξ and test the selection criterion:

$$\xi < 0.375\hat{\sigma}(x)(1 - \hat{\Omega}.\vec{v}/c). \tag{3.34}$$

If it is satisfied, $\vec{p}$ will be accepted; otherwise we choose a new $\vec{p}$.

• Choice of coordinate system

Let us choose the velocity vector

$$\vec{v^0} = v_1^0\hat{i} + v_2^0\hat{j} + v_3^0\hat{k}.$$

Assuming

$$\rho^2 = (v_1^0)^2 + (v_2^0)^2 > 0,$$

and introducing the unit vectors

$$\hat{w^0} = (v_2^0\hat{i} - v_1^0\hat{j})/\rho,$$

and

$$\hat{t^0} = (v_1^0 v_3^0\hat{i} + v_2^0 v_3^0\hat{j} - \rho^2\hat{k})/\rho,$$

which together with $\hat{v^0}$ form an orthonormal triad, the direction of the vector $\vec{\Omega'}$ may conveniently be expressed in the coordinate system $\hat{v^0}, \hat{w^0}$ and $\hat{t^0}$:

$$\vec{\Omega'} = \mu'\hat{v^0} + (1 - \mu'^2)^{1/2}(\cos\phi'\hat{w^0} + \sin\phi'\hat{t^0}),$$

where ϕ' denotes the azimuthal scattering angle, measured from the direction $\hat{w^0}$ in a plane perpendicular to $\hat{v^0}$. The components of $\vec{\Omega'}$ in the stationary coordinate system $\hat{i}, \hat{j}, \hat{k}$ can be written as:

$$\Omega_1' = \mu'v_1^0 + (1 - \mu'^2)^{1/2}\rho^{-1}(v_2^0\cos\phi' + v_1^0 v_3^0\sin\phi'), \tag{3.35}$$

$$\Omega_2' = \mu'v_2^0 + (1 - \mu'^2)^{1/2}\rho^{-1}(-v_1^0\cos\phi' + v_2^0 v_3^0\sin\phi'), \tag{3.36}$$

$$\Omega_3' = \mu'v_3^0 - (1 - \mu'^2)^{1/2}\rho\sin\phi'. \tag{3.37}$$

The scattering angle can then be computed from the relation

$$\vec{\Omega}.\vec{\Omega'} = \Omega_1\Omega'_1 + \Omega_2\Omega'_2 + \Omega_3\Omega'_3.$$

The joint distribution density of the random variables μ' and ϕ' is given by

$$p(\mu', \phi') = \frac{1}{\sigma}\frac{d\sigma}{d\Omega}.$$

Expression for the differential scattering cross section is given by Eqn. (2.56), and the change in frequency of a photon when it is scattered is given by Eqn. (2.52). The joint density can be written in product form:

$$p(\mu', \phi') = \frac{1}{\hat{\sigma}}p_1(\mu', \phi')Y, \tag{3.38}$$

where the normalized density

$$p_1(\mu', \phi') = \frac{1}{4\pi\gamma^2(1 - \mu'v/c)^2}, \tag{3.39}$$

and the functional factor Y is bounded:

$$Y = \left(\frac{x}{x'}\right)^2 X \le 2. \tag{3.40}$$

The factor $1/\hat{\sigma}(x)$ is independent of μ' and ϕ', and plays the role of a constant. X is given by Eqn. (2.57).

•Modeling algorithm

The representation (3.38) enables us to device a rejection technique for modeling random variables μ' and ϕ'. We assume that the quantities μ and x have already been computed.

a) We take two random numbers ξ_1, ξ_2 to compute a possible direction of scattering [for the density $p_1(\mu', \phi')$]:

$$\mu' = \frac{v/c + 2\xi_1 - 1}{1 + (v/c)(2\xi_1 - 1)}, \tag{3.41}$$

$$\phi' = 2\pi\xi_2. \tag{3.42}$$

(keeping in mind that these are not yet the final quantities).

b) We compute the vector $\vec{\Omega'}$, the scattering angle $\vec{\Omega}.\vec{\Omega'}$, and then the ratio:

$$\frac{x'}{x} = \left[1 + \frac{h\nu(1 - \vec{\Omega}.\vec{\Omega'})}{\gamma mc^2(1 - \mu'v/c)}\right]^{-1}. \tag{3.43}$$

We also compute the factor Y from Eqn. (3.40).

    c) We draw a random number ξ_3 and test the selection condition

$$2\xi_3 < Y. \tag{3.44}$$

If it is satisfied, the direction $\vec{\Omega'}$ is accepted, and the new photon energy will be

$$h\nu' = \frac{x'}{[2\gamma(1 - \mu'v/c)]}mc^2; \tag{3.45}$$

If instead

$$2\xi_3 \geq Y,$$

we return to step (a).

3.4 Results of a Sample Monte Carlo Simulation

We use the above Monte Carlo techniques to develop a simulation code which we will apply to solve different problems in situations of our interest.

3.4.1 Statement of the Problem

Let a spherical cloud of radius R contains a uniform density N_e of Maxwellian electrons at temperature $k_B T_e$. At the centre of the cloud there is a black hole of mass M. Within the sphere we place either a low-frequency blackbody source having temperature $T_r \ll T_e$, or a hard-radiation source with a power-law spectrum $I(E) \propto E^{-\alpha}$. The electrons are moving towards the black hole with a free fall velocity. We are trying to calculate the radiation emerging from the electron cloud.

3.4.2 Results and Discussions

The spectral variations are shown in Fig. 3.3 and Fig. 3.4. The mass of the black hole used in this simulation is $10 M_\odot$. The radius of the spherical electron cloud is $50 r_g$. In these two simulations we have used two different kinds of photon energy distributions and source geometry. For the first case (Fig. 3.3), source of soft photons is a disk (inner radius $2 r_g$ and outer radius $50 r_g$) at the equatorial plane of the cloud emitting photons that follow power-law ($E^{-\alpha}$) energy distribution with $\alpha = 1.5$. In Fig. 3.3 the variation of the intensity of the photons coming out of
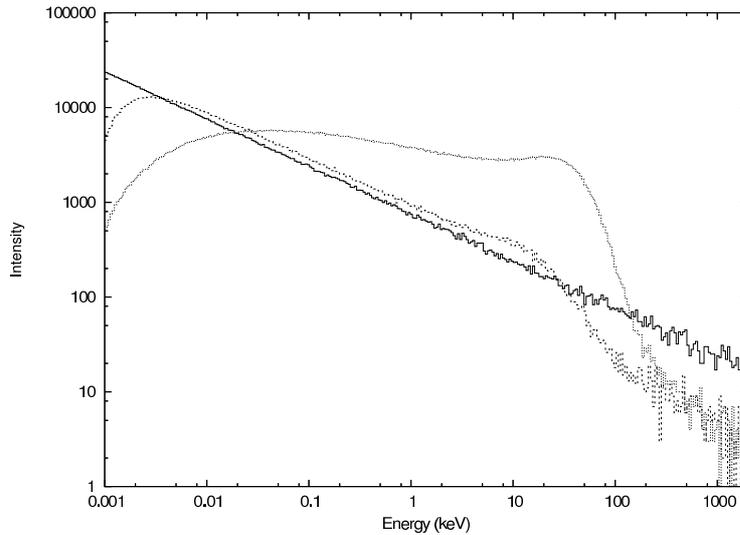
Figure 3.3: Variation of the intensity of the photons with energy. Power-law photons with $\alpha = 1.5$ are injected from a distributed source at the equatorial plane of the electron cloud with temperature $k_B T_e = 5$ keV. Change in the injected spectrum (solid curve) in presence (dotted) and absence (dashed) of the bulk velocity of the electrons are shown.
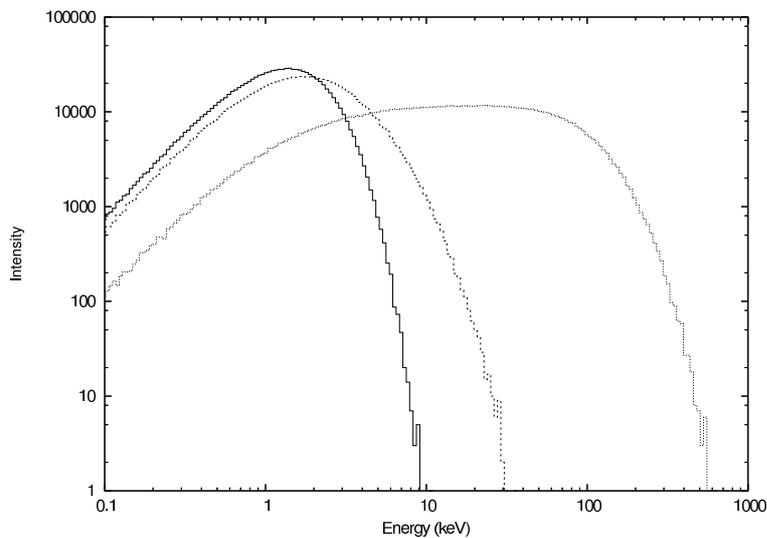

Figure 3.4: Variation of the output photon intensity with $k_B T_e$. Black Body photons with temperature 0.5 keV (solid curve) are injected into the cloud with temperatures 5 keV (dashed curve) and 50 keV (dotted curve) (see text for details).

the cloud is plotted against energy. The electron cloud has uniform temperature $k_B T_e = 5$ keV, throughout the cloud. The solid curve shows the injected spectrum, the dashed and the dotted curves are the output spectra in absence and in presence of the bulk velocity of the electrons, respectively. Fig. 3.4 shows the variation of the intensity with the energy when mono-energetic (temperature, $k_B T_p = 0.5$ keV) black body photons are injected isotropically from a point source (kept at a distance of $10 r_g$ from the black hole) inside the cloud. In this case the cloud temperature is 5 keV (dashed curve) and 50 keV (dotted curve). The solid curve shows the injected black body spectrum. The bulk velocity of the cloud has been kept zero in this case. In both the cases, electron number density at each point of the cloud is also kept constant at 9×10^{16}/cc. From these two plots we can see that an increase in the bulk velocity or temperature of the cloud increases the Comptonization of the photons. All these effects of thermal and bulk motion Comptonization will be discussed in the next Chapters.

Chapter 4

Thermal Comptonization in an Accretion Flow

4.1 Introduction

In Chapter 3, we have discussed that Monte Carlo simulation has been found to be an essential tool to understand the formation of spectrum in compact bodies (PSS83). The work of ST80 showed that the power-law component of a black hole spectrum is due to inverse Comptonization. More work (ST85) firmly established this. Hua & Titarchuk (1996) confirmed the conclusions drawn in ST80, ST85 and Titarchuk (1994) using a Monte Carlo simulation. Meanwhile, more efforts were made to understand the nature of the Compton cloud itself and generally it was believed that accretion disk coronas could be responsible for Comptonization.

While the general results of ST80 and ST85 are of great importance, the computations in the literature were done with a few specific geometries of the cloud, such as plane slabs or spherical blobs. In reality, the geometry *must be* more complex, simply because of the angular momentum of matter (C90 and references therein). Indeed, time dependent numerical simulations of sub-Keplerian flows (Molteni, Lanzafame & Chakrabarti, 1994; Molteni, Ryu & Chakrabarti, 1996) confirm the predictions in C90 and clearly show that the geometry of the flow close to a black hole, especially in the post-shock region, is more like a torus, very similar to a thick accretion disk conceived much earlier (e.g., PW80; Rees et al. 1982 and references therein). In the latter case, the radial velocity was ignored but the angular momentum was assumed to be sub-Keplerian, while in the simulations of Molteni et al. (1994) the radial velocity was also included. In CT95 and C97, theoretical computation of the spectra was made by using the post-shock region as the Comptonizing cloud and by varying the accretion rates in the Keplerian and sub-Keplerian components. Here too somewhat ideal geometry (cylindrical) was chosen so as to utilize the ST80 and ST85 results as far as the radiative transfer properties are concerned. A result with a real toroidal geometry can be handled only when the Monte Carlo simulations are used.

In the present Chapter, we attempt to solve the problem of spectral properties using a thick accretion disk of toroidal geometry as the Compton cloud which is supposed to be produced by the sub-Keplerian inflow. The outer boundary of the thick accretion disk is treated as the inner edge of the Keplerian disk. One positive aspect in treating the CENBOL in this manner is that the distribution of electron density and temperature can be obtained totally analytically. In a more realistic case, one needs to solve the coupled transonic flow solution with radiative transfer. This will be described in Chapter 6. The plan of this Chapter is the following. In the next Section, we discuss the geometry and hydrodynamic properties of the Compton cloud and the source of soft photons used in our simulation. In §4.3, the results of the simulations are presented and in §4.4, we draw conclusions.

4.2   The Electron Cloud and the Soft Photon Source

In Fig. 4.1, we present a cartoon diagram of our simulation set up. In this paradigm picture, the Compton cloud (CENBOL) is produced by the standing shock in the sub-Keplerian flow. CENBOL behaves like a boundary layer as it dissipates the thermal and bulk energy and produce hard X-rays and outflow/jets. The Keplerian disk is truncated and the inner edge is typically extended till the outer boundary of the CENBOL (shock location). However, in the soft states when the post-shock region is cooled down, the Keplerian disk can extend till the last stable circular orbit.

As the CENBOL is puffed up, its hot electrons intercept the soft photons and reprocess them via inverse Compton scattering. A photon originally emitted towards the CENBOL may undergo a single, multiple or no scattering with the hot electrons. The photons which enter the black holes are absorbed.

4.2.1   Thermodynamic Conditions Inside the Compton Cloud

Chakrabarti (1989) showed that centrifugal pressure supported Rankine-Hugoniot shock solutions exist for the stationary, axially symmetric and rotating adiabatic accretion flows around a black hole. In order to verify these results, Molteni, Lanzafame and Chakrabarti (1994) carried out a two dimensional numerical simulation and found that the shock is indeed formed and the post-shock region (CENBOL) has all the properties of a thick accretion disk (PW80). The simulation result is more realistic than a thick disk, since the flow also has a significant radial motion close to the horizon. Fig. 4.2 shows the equilibrium structure of the equipotential surfaces of a thick accretion disk for a barotropic matter in Schwarzschild geometry. Very far away from the black hole, the contours are almost spherical in shape since the
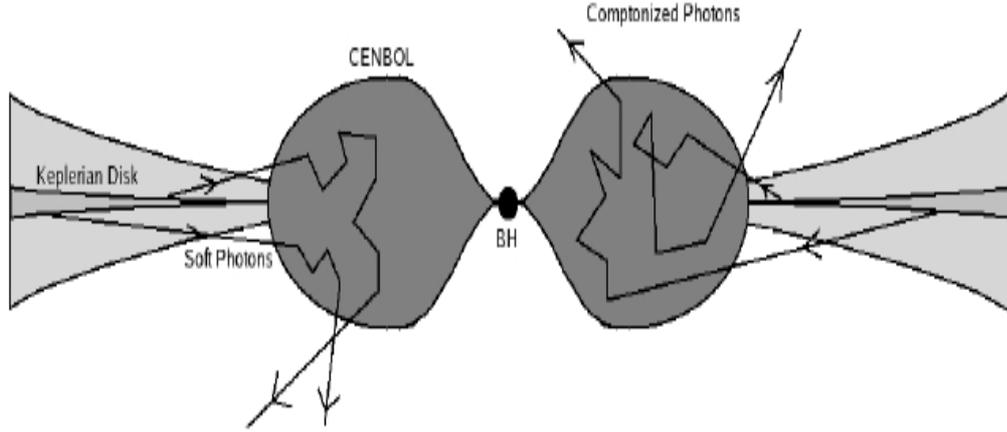
Figure 4.1: A cartoon diagram of the geometry of the Compton cloud used for the Monte Carlo Simulations presented in this Chapter. The puffed up post-shock region surrounds the black hole and it is surrounded by the Keplerian disk on the equatorial plane. A tenuous sub-Keplerian flow above and below the Keplerian disk is also present (CT95). Typical photon scattering paths are shown (Ghosh et al., 2009; hereafter GCL09).

effect of angular momentum is very weak as compared to gravity. The centrifugal barrier keeps the matter away from the axis of the disk, thus providing space for jet formation.

For simplicity, in the present Monte Carlo simulation, we assume the CENBOL to have the same analytical shape as an ideal thick disk (Fig. 4.3) and compute the matter density and temperature distribution using the prescription given in Chakrabarti, Jin and Arnett (1987). Here we assume that the disk is adiabatic and the specific angular momentum and specific entropy is constant throughout the disk. The equation of state is given by $p = K\rho^{\gamma}$, where p and ρ are the isotropic pressure and the matter density, respectively, γ is the adiabatic index and K is the entropy constant. The pressure p is considered to be contributed by the gas pressure and the radiation pressure. Thus,

$$p = p_{gas} + p_{rad}.$$
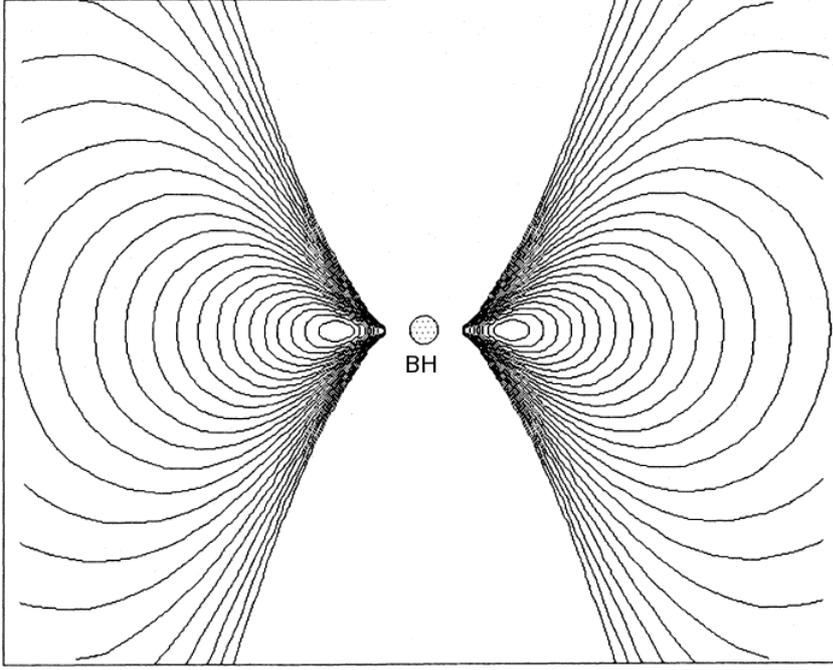
Figure 4.2: Typical structure of the equipotential contours for the thick accretion disk in the Schwarzschild geometry (Figure taken from Chakrabarti, Jin & Arnett, 1987).

For a fully ionized ($T > 10^4$ K) nondegenerate and nonrelativistic ideal gas we have

$$p_{gas} = \frac{T_e \rho \sqrt{r^2 - z^2}}{\mu m_p},$$

where μ is the mean molecular weight, T_e is the cloud temperature and m_p is the mass of the proton. The radiation pressure is given by

$$p_{rad} = \frac{1}{3}aT_e{}^4,$$

where a denotes the Stefan radiation density constant. Using the pseudo Newtonian potential $-\frac{1}{2(r-1)}$ (PW80), the effective potential due to the black hole is written as:

$$\phi(r, z) = \frac{\lambda^2}{2(r^2 - z^2)} - \frac{1}{2(r - 1)}. \tag{4.1}$$

As the disk is static (i.e., electrons have no radial velocity) we can always write in terms of the sound speed a_s:

$$\phi(r, z) = na_s{}^2 = \frac{\gamma p}{\rho}.$$
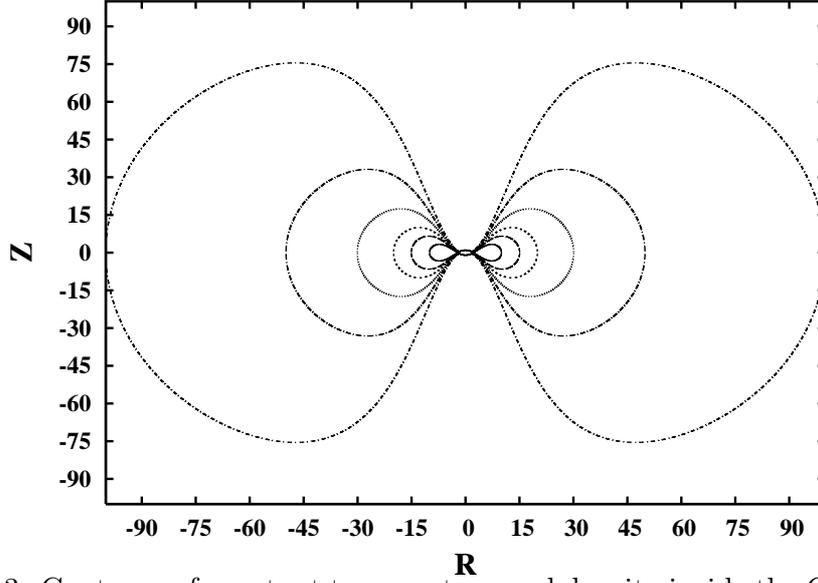
Figure 4.3: Contours of constant temperature and density inside the CENBOL. Each of them has been used as the outer boundary in our simulations. $R_{out} = 10$ (solid line), 15 (large-dashed line), 20 (dashed line), 30 (dotted line), 50 (large dashed-dot line) and 100 (dashed-dot line) (GCL09).

Using the above equations we calculate the distribution of temperature and number density of the electron cloud. The number density of electrons within the CENBOL, $n = \frac{\rho}{\mu m_p}$ is calculated from the matter density ρ, given by:

$$\rho(r, z) = \left[\frac{\phi(r, z)}{n \gamma K} \right]^n, \tag{4.2}$$

where, the entropy constant K is given by,

$$K(\beta, \mu) = \left[\frac{3}{a} \frac{1 - \beta}{\beta^4} \frac{(k_b)^4}{(\mu m_p)^4} \right]^{\frac{1}{3}}, \tag{4.3}$$

where, k_b is the Boltzmann constant and $\beta = \frac{p_{gas}}{p}$, denotes the ratio of the gas pressure to the total pressure. The temperature T_e of the electron cloud within CENBOL is given by,

$$T_e(r, z) = \left[\frac{\beta \mu m_p}{k_b} K \right] \rho^{\frac{1}{3}}. \tag{4.4}$$

The velocity, mass and distance scales are measured in units of c, the velocity of light, M_{bh}, the mass of the black hole and $r_g = 2GM_{bh}/c^2$, the Schwarzschild radius of the black hole. In this unit, the angular momentum of the disk is chosen to be

$\lambda = 1.9$. We have chosen the values of the parameters: $\beta = 0.5$, polytropic index $(n) = 3$ and $\mu = 0.5$. In the simulation we have varied the outer edge (R_{out}) of the CENBOL to different values (by varying ϕ) to change the size of the Compton cloud. The disk (Fig. 4.3) has a centre at 4 and the inner edge at 2.5. For a better understanding of the results, we calculated an effective electron temperature T_{eff} of the CENBOL using the prescription given in Sec. 2.4 of CT95.

4.2.2   Emission from a Keplerian Disk

The soft photons are produced from a Keplerian disk whose inner edge is at the outer edge (R_{out}) of the CENBOL, and the outer edge is at $500 r_g$. The source of soft photons have a multi-color blackbody spectrum coming from a standard (SS73) disk. As the disk is optically thick, the emission is black body type with the local surface temperature (Eqn. 1.9):

$$T(r) \approx 5 \times 10^7 (M_{bh})^{-1/2} (\dot{M}_{17})^{1/4} (2r)^{-3/4} \left[1 - \sqrt{\frac{3}{r}} \right]^{1/4} \text{K},$$

The total number of photons emitted from the disk surface is given by Eqn. (2.6),

$$n_\gamma(r) = \left[16\pi \left(\frac{k_b}{hc} \right)^3 \times 1.202057 \right] . [T(r)]^3 .$$

We divide the disk into different annuli each having an width of δr. The disk between radius r to $r + \delta r$ injects $dN(r)$ number of soft photons isotropically with black body temperature $T(r)$

$$dN(r) = 4\pi r \delta r H(r) n_\gamma(r), \tag{4.5}$$

where, $H(r)$ is the half height of the disk given by:

$$H(r) = 10^5 \dot{M}_{d17} \left[1 - \sqrt{\frac{3}{r}} \right] \text{cm}.$$

In the above equations, the mass of the black hole M_{bh} is measured in units of the mass of the Sun $(M_\odot)$, the accretion rate $\dot{M}_{17}$ is in units of 10^{17} gm/s. Unless otherwise stated, we chose $M_{bh} = 10$, accretion rate $\dot{m} = \frac{\dot{M}}{\dot{M}_{edd}} = 1$ and $\delta r = 0.5 r_g$. For the sake of completion of a simulation using a reasonable amount of computer time, we take a constant fraction of the number of photons (Eqn. 4.5) from each annulus (Table 4.2). Because of the number of photons we select is way below the actual number, the absolute value of accretion rate itself is not very meaningful.
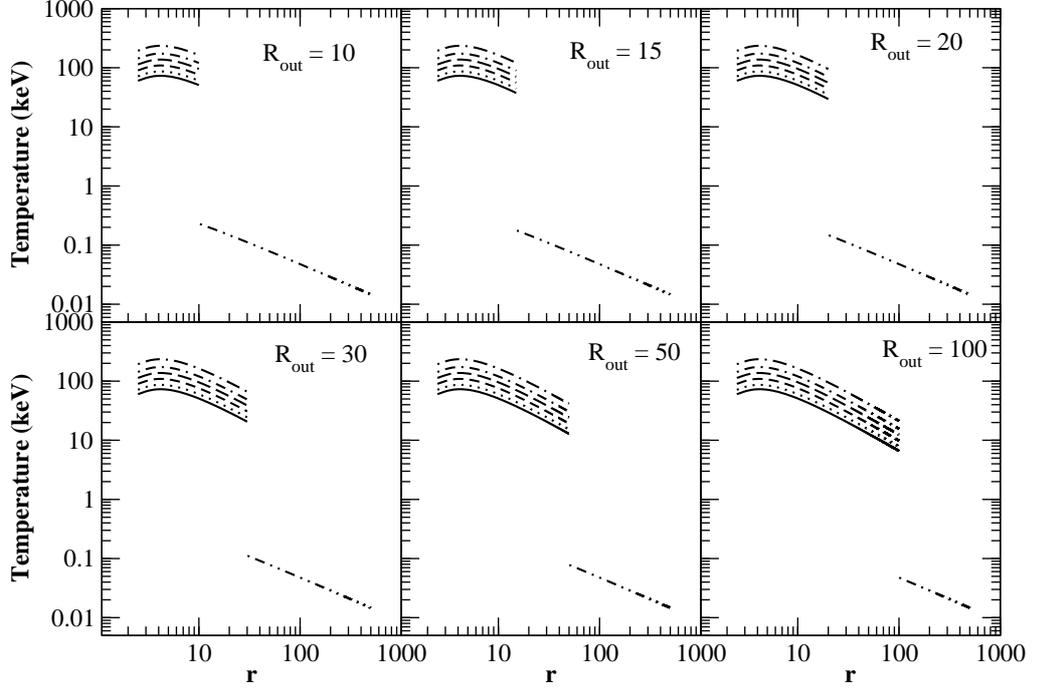
Figure 4.4: Temperature distribution (in keV) inside the disk and the CENBOL region for different CENBOL outer boundary (R_{out}) and various central densities. Table 4.1 gives the relation between the central densities and the line styles (GCL09).

However, the relative number of the intercepted photons and the number density of electrons inside CENBOL appears to be more important. The result also does not depend on the choice of δr as long as it is a fraction of a Schwarzschild radius. In Fig. 4.4, we show the distribution of the temperature (in keV) in the Keplerian disk and that in the CENBOL which we have used in our simulations. Different panels are for different values of the outer edge R_{out} (marked) of the CENBOL radius. We provide the effective temperature (T_{eff}) within the post-shock region in R_{out} in Table 4.1. These were obtained by changing the central density of the thick disk, which gave a temperature distribution inside CENBOL. Subsequently, CT95 was followed to obtain an effective temperature. In simulations, however, the actual temperature distribution was used.

Table 4.1 (GCL09)

Central electron number densities (n in cm^{-3}) and the effective temperatures (in keV) for various outer edge R_{out} of the CENBOL used in this Chapter.

n (cm^{-3}) $\downarrow R_{out} \rightarrow$	10	15	20	30	50	100	Line style
7×10^{19}	61	54	50	46	43	42	Solid
1×10^{20}	73	64	59	54	51	50	Dotted
2×10^{20}	91	80	74	68	65	63	Short dashed
5×10^{20}	115	101	93	86	81	79	Big dashed
9×10^{20}	145	128	118	109	102	99	Dash-dotted
2×10^{21}	197	173	160	147	139	135	Big dash-dotted

4.3   Simulation Procedure

In a simulation, we randomly generated a photon out of the Keplerian disk and using another set of random numbers we obtained its injected direction. With another random number we obtained a target optical depth τ_c at which the scattering takes place. The photon is followed within CENBOL till the optical depth reached τ_c. At this point a scattering is allowed to take place and the energy exchange is computed through Compton or inverse Comptonization (see Chapter 3 for details). The electrons are are assumed to obey relativistic Maxwell distribution inside CENBOL. The photon frequencies are also gravitationally red-shifted or blue shifted depending on its relative location change with respect to the black hole. The process is continued till the photon either leaves the CENBOL or is absorbed by the black hole.

4.4   Results and Discussions

In Table 4.2, we summarize all the cases for which the simulations have been presented in this Chapter. In Col. 1, various cases are marked. In Col. 2, the R_{out} and T_{eff} in keV are listed. In Cols. 3 we show the temperature (T_p) from the innermost annulus (R_{out}) of the Keplerian disk. Columns 4, 5, 6 and 7 show the total number of injected photons (N_{inj}), number of the photons intercepted by the CENBOL (N_{int}), number of photons which suffered Compton scattering (N_{cs}) and the number of photons captured (N_{cap}) by the black hole respectively. In Column 8 we calculated the percentage p of the total injected photons that have suffered scattering through CENBOL. In Column 9, we present the energy spectral index α ($I(E) \sim E^{-\alpha}$) obtained from our simulations.

Table 4.2: Summary of all the simulation cases presented in this Chapter (GCL09).

Case	R_{out}, T_{eff}	T_p	N_{inj}	N_{int}	N_{cs}	N_{cap}	p	α
1a	10, 61	0.227	115150710	3042538	3024733	17805	2.627	2.10
1b	10, 73	-do-	-do-	3043059	3025416	17643	2.627	1.90
1c	10, 91	-do-	-do-	3041990	3024452	17538	2.627	1.65
1d	10, 115	-do-	-do-	3046115	3028743	17372	2.630	1.40
1e	10, 145	-do-	-do-	3043849	3026646	17203	2.628	1.15
1f	10, 197	-do-	-do-	3042031	3025183	16848	2.627	0.90
2a	15, 54	0.177	101283949	4011191	4005770	5421	3.955	1.12
2b	15, 64	-do-	-do-	4011473	4006227	5246	3.955	0.99
2c	15, 80	-do-	-do-	4012125	4007312	4813	3.957	0.82
2d	15, 101	-do-	-do-	4013872	4009153	4719	3.958	0.70
2e	15, 127	-do-	-do-	4007883	4003407	4476	3.953	0.57
2f	15, 173	-do-	-do-	4011584	4007483	4101	3.957	0.45
3a	20, 50	0.147	91280716	4224551	4222011	2540	4.625	0.85
3b	20, 59	-do-	-do-	4222520	4219921	2599	4.623	0.75
3c	20, 74	-do-	-do-	4224950	4222666	2284	4.626	0.64
3d	20, 93	-do-	-do-	4221994	4219926	2068	4.623	0.54
3e	20, 118	-do-	-do-	4223468	4221663	1805	4.623	0.44
3f	20, 160	-do-	-do-	4222218	4220626	1592	4.623	0.34
4a	30, 46	0.111	77355270	4369685	4368926	759	5.648	0.65
4b	30, 54	-do-	-do-	4366959	4366302	657	5.645	0.56
4c	30, 68	-do-	-do-	4367505	4366932	573	5.645	0.46
4d	30, 86	-do-	-do-	4371154	4370665	489	5.650	0.40
4e	30, 109	-do-	-do-	4368390	4367963	427	5.647	0.35
4f	30, 147	-do-	-do-	4372356	4372014	342	5.652	0.29
5a	50, 43	0.078	60533079	4194919	4194781	138	6.930	0.56
5b	50, 51	-do-	-do-	4195709	4195582	127	6.931	0.50
5c	50, 65	-do-	-do-	4196096	4195988	108	6.931	0.44
5d	50, 81	-do-	-do-	4195788	4195715	73	6.931	0.38
5e	50, 102	-do-	-do-	4194298	4194244	54	6.929	0.32
5f	50, 139	-do-	-do-	4194327	4194282	45	6.929	0.28
6a	100, 42	0.048	39539601	3780685	3780669	16	9.562	0.42
6b	100, 50	-do-	-do-	3801929	3801919	10	9.615	0.30
6c	100, 63	-do-	-do-	3808845	3808843	2	9.633	0.24
6d	100, 79	-do-	-do-	3812567	3812565	2	9.642	0.19
6e	100, 99	-do-	-do-	3814646	3814644	2	9.648	0.17
6f	100, 135	-do-	-do-	3815355	3815353	2	9.650	0.13

In Fig. 4.5, we summarize the results of all the cases, bunching them in groups with the same CENBOL size. Different cases are marked in each panel. Curves (a) to (f) are from bottom to top respectively. Note that as T_{eff} is raised (a $\rightarrow$ f), the spectrum becomes harder. Also, as R_{out} is increased, the percentage p of photons intercepted is also increased as the CENBOL becomes bigger. However,

as the CENBOL size is increased, it becomes increasingly difficult to soften the spectrum with the same number of injected photons. Thus the spectrum becomes harder. This behavior matches with the earlier theoretical predictions (Fig. 6 of C97). All the spectra are angle-averaged.
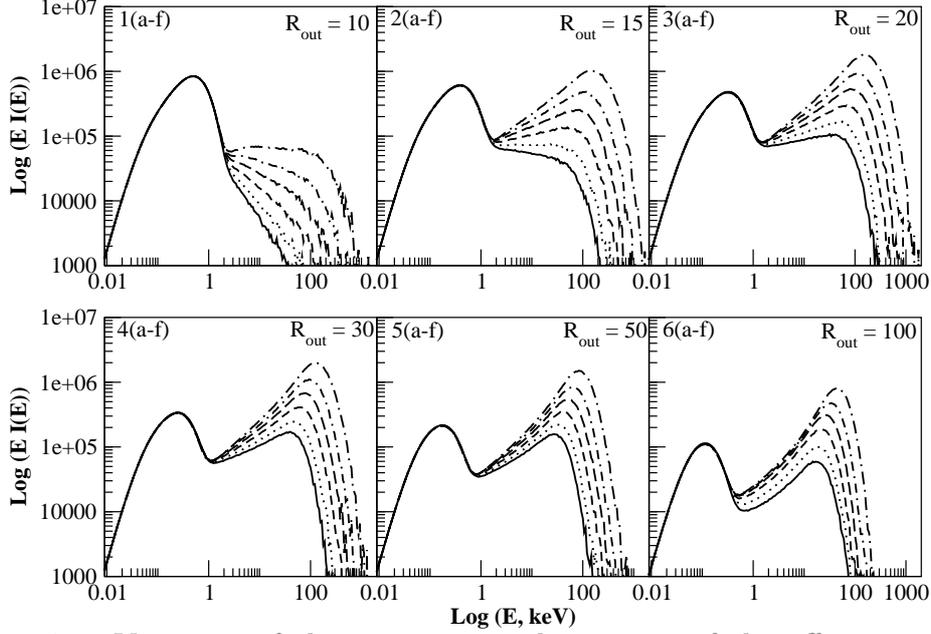

Figure 4.5: Variation of the spectrum with increase of the effective temperature (T_{eff}) of the CENBOL for a fixed CENBOL size R_{out}. Each panel marks the cases for which the spectrum is drawn. Curves for (a) to (f) are from bottom to top respectively along the direction of increasing density and effective temperature (GCL09).

In Fig. 4.6, we take one set, namely, Cases 3(a-f), for which $R_{out} = 20$ but the temperature distribution is varied which also changed T_{eff}. Here we draw each components, namely, the injected component (solid), the intercepted component (dotted) and the Comptonized component (dashed) separately. The net spectrum is shown as the dash-dotted curve. As we increase the temperature of the CENBOL, it becomes increasingly harder to cool the electrons, and thus the spectrum becomes harder. In Fig. 4.7, we show two typical cases (Cases 3a and 3f) in which we wish to demonstrate how the power-law component has been produced. The solid curve represents the injected photons. The dotted, dashed, dotdashed and double dot-dashed curves show contributions from photons which underwent 1, 2, 3 and 4 or
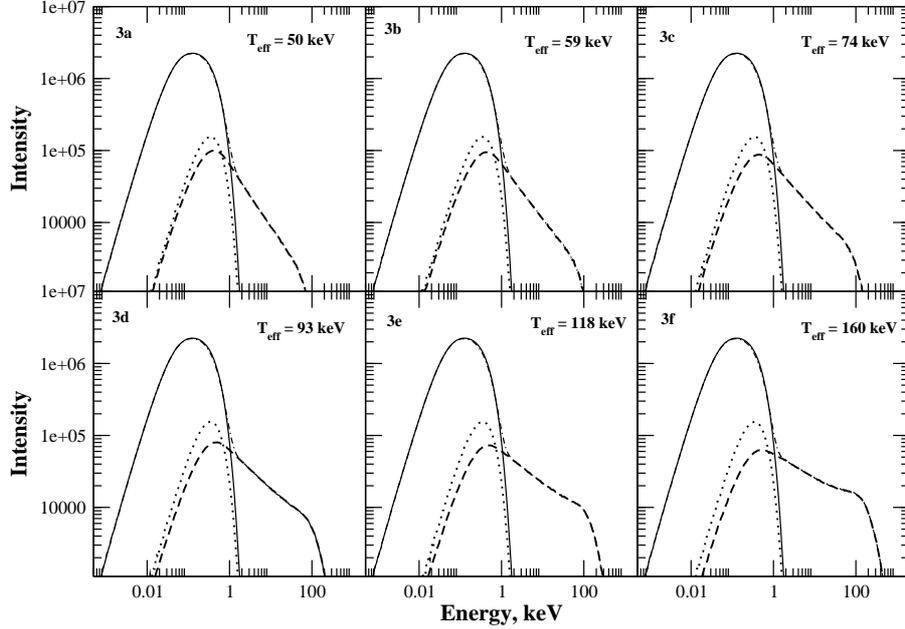
Figure 4.6: Components of the emerging spectrum with a Keplerian disk outside $R_{out} = 20$ and their variation with the effective temperature of the CENBOL. As the electron temperature becomes hotter, the spectrum also gets harder (GCL09).

above number of scattering respectively.

The spectral variation with the CENBOL size has been plotted in Figs. 4.8 and 4.9. Cases (1-6)a are shown in Fig. 4.8 and Cases (1-6)f are shown in Fig. 4.9. Solid, dashed, small-dashed, dotted, long-dashed and small dash-dotted curves are drawn for Cases 1, 2, 3, 4, 5 and 6, respectively. With the increase in size of the CENBOL, the spectrum becomes harder, although the optical depth weighted effective temperature becomes lower. The latter causes the cut-off energy to become lower as well.

In order to understand how the spectrum is influenced by the photons from different annuli, we compute the fraction of injected photons from each annulus which suffer scattering. In Fig. 4.10, we show the result for various CENBOL sizes. What we find is that when the CENBOL size is smaller, say, $R_{out} = 10$, only about 20% photons are intercepted from the nearest annulus, but the effect of the annuli close to the periphery is negligible. On an average, however, only 2.6% get intercepted (see Table 4.2). When the CENBOL size is bigger, say, $R_{out} = 100$,
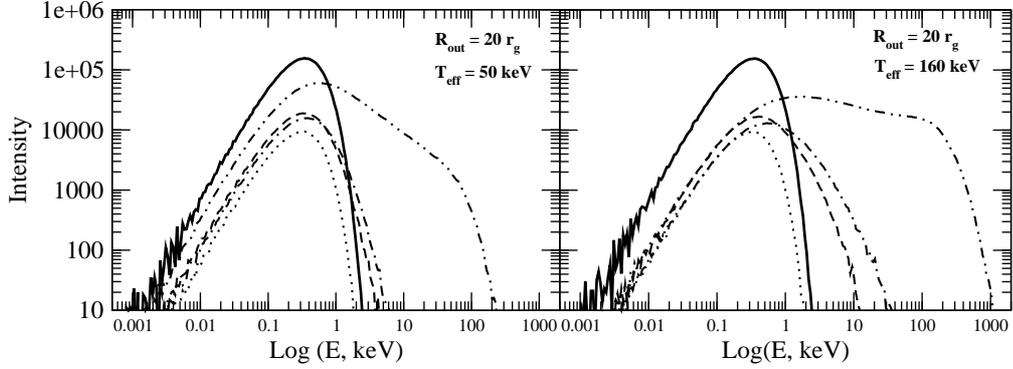
Figure 4.7: Components of the emerging spectra with a Keplerian disk outside $R_{out} = 20$. The solid curve is for the injected photons. The dotted, dashed, dot-dashed and double dot-dashed curves show contributions from photons with number of scattering 1, 2, 3 and 4 or higher respectively. Cases 3a (left) and 3f (right) are shown (GCL09).
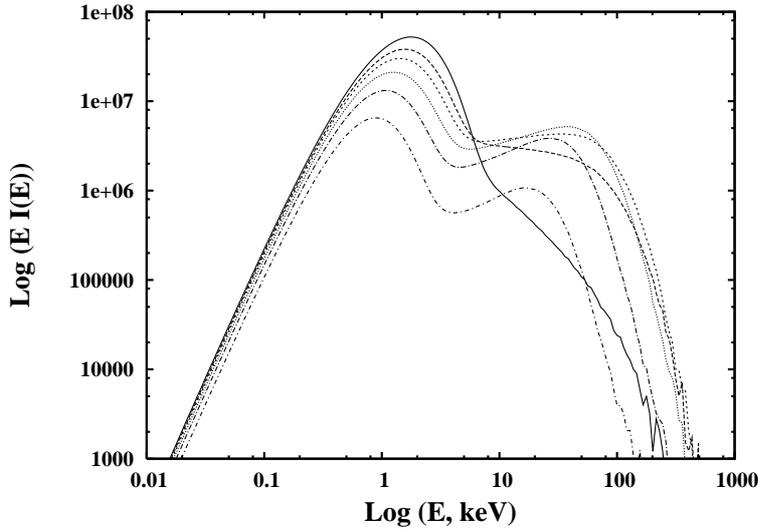

Figure 4.8: Variation of the spectrum with the CENBOL size is shown. The cases correspond to Cases (1-6)a which are drawn in solid, dashed, small-dashed, dotted, long-dashed and small dash-dotted curves respectively. See Table 4.2 for parameters. With increase in size of the CENBOL the spectrum becomes harder to cool, although the optical depth weighted effective temperature becomes lower. The latter causes the cut-off energy to become lower (GCL09).
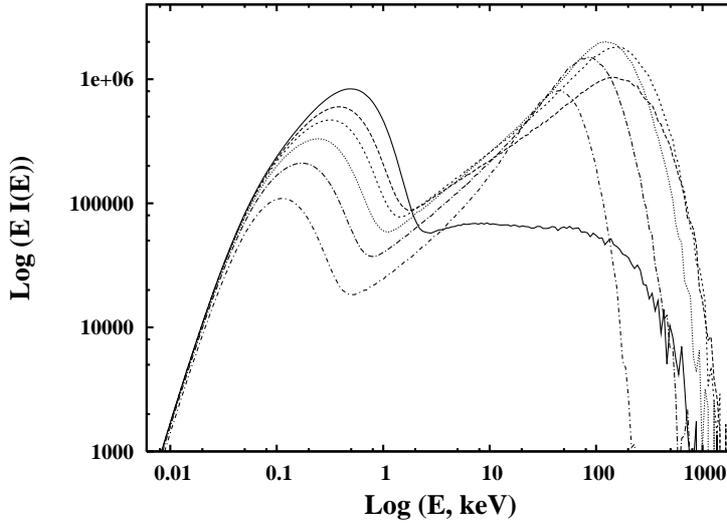
Figure 4.9: Same as Fig. 4.8. The cases correspond to Cases (1-6)f which are drawn in solid, dashed, small-dashed, dotted, long-dashed and small dash-dotted curves respectively. Table 4.2 lists all the parameters.

almost 50% of the photons from the annulus immediately outside the CENBOL gets intercepted and scattered. In this case, on an average, about 10% photons from the whole disk is scattered. From Table 4.2 we see that the nature of the above plot does not change for a particular CENBOL size even when the temperature is varied. So it is purely a geometric effect.

It is in general instructive to understand the behavior when the black hole mass is much higher. In this case, the effective temperature could be much lower and the accretion rate will also be generally lower. In Table 4.3, we show the cases which were run for a massive black hole. We chose the mass to be $10^9 M_\odot$ and the accretion rate $\dot{m} = 0.001$. For the sake of comparison with the earlier cases, we selected the CENBOL parameters exactly same as in Cases 5(a-f). In Fig. 4.11, we note that for super-massive black hole, the Keplerian photons are cooler. Nevertheless, the inverse Comptonization extends the spectra to very high energies. This is because the source of the energy is the hot electron cloud itself. The variation of α, the spectral index is given in the table and they are marginally softer compared to what was observed for smaller black holes (Table 4.2).
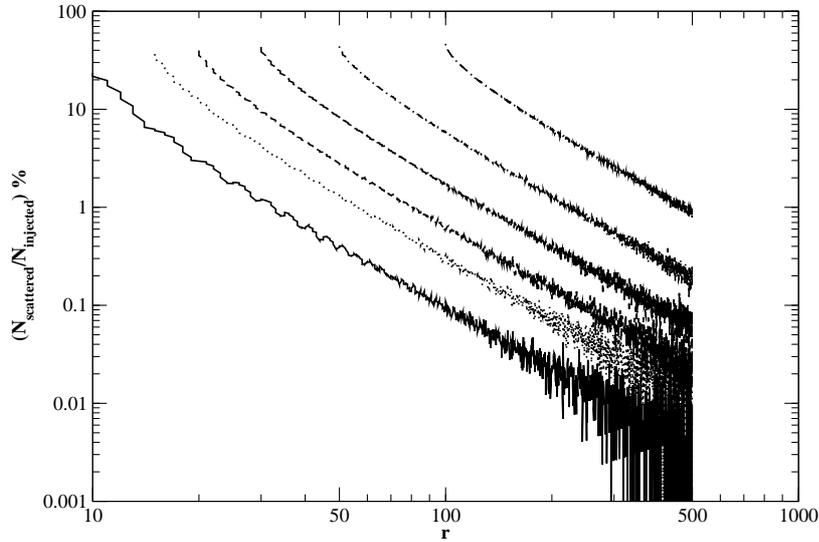
Figure 4.10: Ratio of the scattered photons and the injected photons for different annuli of the Keplerian disk. Cases (1-6)e are drawn from bottom to top. The result is insensitive to the effective temperature of the electrons and generally depends on the relative geometry (GCL09).
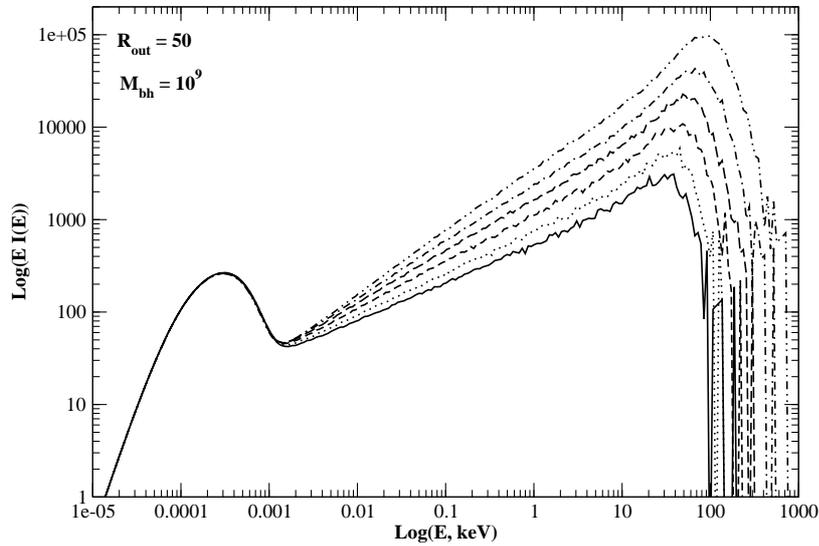

Figure 4.11: Plot of EI(E) for Cases 7(a-f) (presented in Table 4.3) are shown. For these simulations we considered $\dot{m} = 0.001$, $M_{bh} = 10^9 M_\odot$. Curves (a) to (f) are from bottom to top respectively (GCL09).

Table 4.3: Summary of the simulation cases for a massive black hole (GCL09).

Case	R_{out}, T_{eff}	T_p	N_{inj}	N_{int}	N_{cs}	N_{cap}	p	α
7a	50, 43	1.39E-4	34037468	2359549	2359463	86	6.932	0.59
7b	50, 51	-do-	-do-	2358802	2358725	78	6.930	0.55
7c	50, 65	-do-	-do-	2359201	2359145	57	6.931	0.50
7d	50, 81	-do-	-do-	2359354	2359313	41	6.931	0.44
7e	50, 102	-do-	-do-	2360152	2360114	38	6.934	0.39
7f	50, 139	-do-	-do-	2358340	2358314	26	6.929	0.32

In the present computation we assumed a stationary toroidal accretion disk. An inclusion of the radial component of velocity can produce an interesting effect, particularly visible when the spectral index is very high (in the so-called soft-state of the black hole). Here the electrons become so cold that the thermal Comptonization is ineffective and the power-law spectrum is dominated by the bulk motion Comptonization (CT95). This effect for spherical cloud has been demonstrated by Laurent & Titarchuk (1999) and can be considered to be a signature of a black hole candidate, since the radial velocity is high for infalling matter around such objects. In the next Chapter, we will show the results of the simulations incorporating the bulk velocity of the electron. We will also show the effects of the presence of an outflow along with the inflow. In presence of a rotational motion, preliminary results (Chakrabarti, Titarchuk, Kazanas & Ebisawa, 1996) show that the spectrum tends to become harder. Similarly, the outflow, which is generally believed to be formed out of the Compton cloud (here CENBOL) itself, can also Comptonize the injected photons and in certain situation could be very important.

Chapter 5

Effects of Thermal and Bulk Motion Comptonizations in Presence of an Outflow

5.1 Introduction

So far, we have only discussed the effects of thermal Comptonization on the soft photons injected into a static Compton cloud (Chapter 4). In the present Chapter, we will show the effects of the bulk velocity of the cloud on the emitted spectrum from an accretion disk. As discussed in Chapter 1, the accretion flow onto a black hole is necessarily transonic in nature. In the context of the spherical flows, Bondi (1952) solution of accretion and Parker (1959) solution of winds are clear examples of transonic flows. But they have only one sonic point. In presence of angular momentum, the flow may have two saddle type sonic points with a shock in between (C90, Chakrabarti, 1996a). The solutions with shocks have been extensively studied in both the accretion and the winds even when rotation, heating, cooling etc. are included (C90, Chakrabarti, 1996a). The study demonstrates that the accretion and the winds are inter-related, the outflows are generated from the post-shock region. Subsequently, in C99, Das & Chakrabarti (1999) and Das et al. (2001), the mass outflow rate was computed as a function of the shock strength and other flow parameters. Meanwhile, in the so-called two component advective flow (TCAF) model of CT95 and C97, the spectral states were shown to depend on the location and strength of the shock. Thus, C99 for the first time, brought out the relationship between the jets and outflows with the presence or absence of shocks, and therefore with the spectral states of a black hole candidate. This paves the way to study the relative importance between the Compton cloud and the outflow as far as the emerging spectrum is concerned.

Computation of the spectral characteristics have so far been done only for the advective accretion flows (CT95; Chakrabarti & Mandal, 2006) and the outflow or the base of the jet was not included. In the Monte-Carlo simulations of Laurent

& Titarchuk (2007), outflows in isolation were used, but not in conjunction with inflows. In GCL09, the results of Monte-Carlo simulations in a setup similar to that of CT95 was presented (Chapter 4). In the present Chapter (Ghosh, et al., 2010; hereafter GG10), we improve this and obtain the outgoing spectrum in presence of both inflows and outflows. We also include a Keplerian disk inside an advective flow which is the source of soft photons. We show how the spectrum depends on the flow parameters of the inflow, such as the accretion rates of the two components and the shock strength. The post-shock region being denser and hotter, it behaves like the so-called 'Compton cloud' in the classical model of ST80. This is the CENBOL region described in Chapter 1. The shock location (size of the Compton cloud) and its strength depends on the basic parameters of the flow, such as the specific energy, the accretion rate and the specific angular momentum. Thus, the basic Comptonized component of the spectrum is a function of the flow parameters. Since the intensity of soft photons determines the Compton cloud temperature, the result depends on the accretion rate of the Keplerian component also. In our result, we see the effects of the bulk motion Comptonization (CT95) because of which even a cooler CENBOL produces a harder spectrum. At the same time, the effect of down-scattering due the outflowing electrons is also seen, because of which even a hotter CENBOL causes the disk-jet system to emit lesser energetic photons. Thus, the net spectrum is a combination of all these effects.

In the next Section, we discuss the geometry of the soft photon source and the Compton cloud in our Monte-Carlo simulations. In §5.2, we present the variation of the thermodynamic quantities and other vital parameters inside the Keplerian disk and the Compton cloud which are required for the Monte-Carlo simulations. In §5.3, we describe the simulation procedure and in §5.4, we present the results of our simulations. Finally in §5.5, we make concluding remarks.

5.2   Geometry and Properties of the Flow

To simplify the geometry of the inflow-outflow configuration without sacrificing the salient features, we first assume the flow geometry as depicted in the cartoon diagram presented in Fig. 5.1. This is our simulation set up. The components of the hot electron clouds, namely, the CENBOL, the outflow and the sub-Keplerian flow, intercept the soft photons emerging out of the Keplerian disk and reprocess them via inverse-Compton scattering. An injected photon may undergo a single, multiple or no scattering at all with the hot electrons in between its emergence from the Keplerian disk and its detection by the telescope at a large distance. The photons which enter the black holes are absorbed. The CENBOL, though toroidal in nature, is chosen to be of spherical shape for simplicity. The sub-Keplerian inflow in the pre-
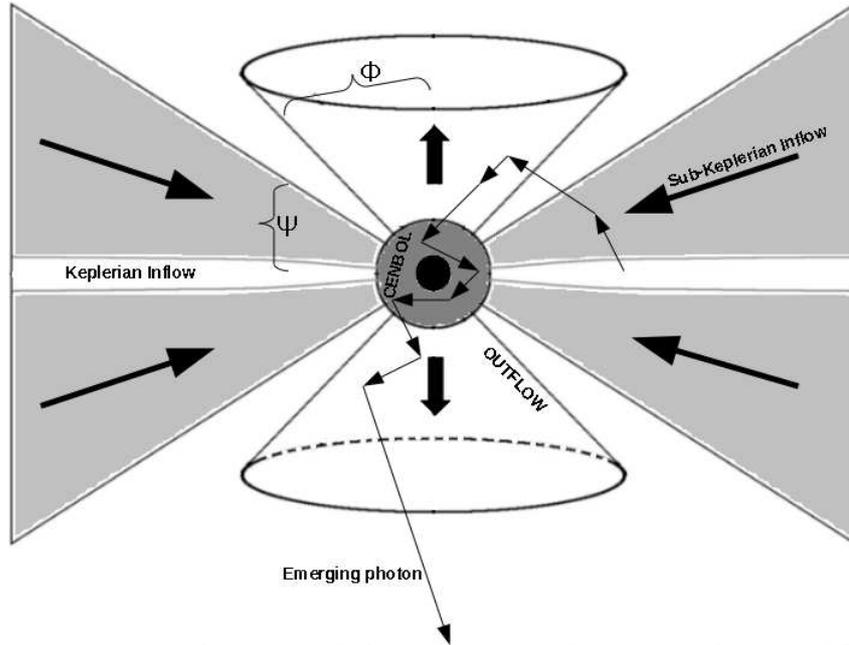
Figure 5.1: A cartoon diagram of the geometry of our initial case of Monte-Carlo simulation. The spherical inflowing post-shock region (CENBOL) surrounds the black hole. The Keplerian disk is on the equatorial plane and a sub-Keplerian halo is above and below. A diverging conical outflow is formed from the CENBOL. The zig-zag path of a typical photon is shown (GG10).

shock region is assumed to be of wedge shape of a constant angle Ψ. The outflow, which emerges from the CENBOL in this picture, is also assumed to be of constant conical angle Φ. In reality, inflow and outflow both could have somewhat different shapes, depending on the balance of the force components. However, the final result is not expected to be sensitive to such assumptions.

5.2.1   Compton Cloud and its Temperature, Density and Velocity

We assume the black hole to be non-rotating and we use the pseudo-Newtonian potential (PW80) to describe the geometry around the black hole. This potential is $-\frac{1}{2(r-1)}$ (Section 1.8). The velocity components and angular momenta are measured in units of c, the velocity of light and $r_g c$ respectively. For simplicity, we have chosen the Bondi accretion solution in pseudo-Newtonian geometry to describe both the accretion and winds. The equation of motion of the sub-Keplerian matter around

the black hole in the steady state is assumed to be given by,

$$u\frac{du}{dr} + \frac{1}{\rho}\frac{dP}{dr} + \frac{1}{2(r-1)^2} = 0.$$

Integrating this equation, we get the expression of the conserved specific energy as,

$$\epsilon = \frac{u^2}{2} + na^2 - \frac{1}{2(r-1)}. \tag{5.1}$$

Here P is the thermal pressure and a is the adiabatic sound speed, given by $a = \sqrt{\gamma P/\rho}$, γ being the adiabatic index and is equal to $\frac{4}{3}$ in our case. The conserved mass flux equation, as obtained from the continuity equation, is given by

$$\dot{m} = \Omega \rho u r^2, \tag{5.2}$$

where, ρ is the density of the matter and Ω is the solid angle subtended by the flow. For an inflowing matter, Ω is given by,

$$\Omega_{in} = 4\pi sin\Psi,$$

where, Ψ is the half-angle of the conical inflow. For the outgoing matter, the solid angle is given by,

$$\Omega_{out} = 4\pi(1 - cos\Phi),$$

where Φ is the half-angle of the conical outflow. From Eqn. (5.2), we get

$$\dot{\mu} = a^{2n} u r^2. \tag{5.3}$$

The quantity $\dot{\mu} = \frac{\dot{m}\gamma^n K^n}{\Omega}$ is the Chakrabarti rate (Chakrabarti, 1989, C90, 1996a) which includes the entropy, K being the constant measuring the entropy of the flow, and $n = \frac{1}{\gamma-1}$ is called the polytropic index. We take derivative of Eqns. (5.1) and (5.3) with respect to r. Eliminating $\frac{da}{dr}$ from both the equations, we get the gradient of the velocity as,

$$\frac{du}{dr} = \frac{\frac{1}{2(r-1)^2} - \frac{2a^2}{r}}{\frac{a^2}{u} - u}. \tag{5.4}$$

Solving this, we obtain the Bondi accretion and wind solutions in the usual manner (C90). Solution of Eqn. (5.4) gives the radial variation of velocity u. Using Eqn. (5.1), we find the radial variation of sound speed a. Finally, we get the temperature profile of the electron cloud (T_e) using $T_e = \frac{\mu a^2 m_p}{\gamma k_B}$, where $\mu = 0.5$ is the mean molecular weight, m_p is the proton mass and k_B is the Boltzmann constant. Using Eqn. (5.2), we calculate the mass density ρ, and hence, the number density variation of electrons inside the Compton cloud. We ignore the electron-positron pair production inside the cloud.

The flow is supersonic in the pre-shock region and sub-sonic in the post-shock (CENBOL) region. We chose this surface at a location (R_s), where the pre-shock Mach number $M = 2$. This location depends on the specific energy ϵ (C90). In our simulation, we have chosen $\epsilon = 0.015$ so that we get $R_s = 10$. We simulated a total of six cases. For Cases 1(a-c), we chose $\dot{m}_h = 1$, $\dot{m}_d = 0.01$ and for Cases 2(a-c), the values are listed in Table 5.2. The velocity variation of the sub-Keplerian flow is the inflowing Bondi solution (pre-sonic point). The density and the temperature of this flow have been calculated according to the above mentioned formulas. Inside the CENBOL, both the Keplerian and the sub-Keplerian components are mixed together. The velocity variation of the matter inside the CENBOL is assumed to be the same as the Bondi accretion flow solution reduced by the compression ratio due to the shock. The compression ratio (i.e., the ratio between the post-shock and pre-shock densities) R is also used to compute the density and the temperature profile of the Compton cloud and the jet. When the outflow is adiabatic, the ratio of the outflow to the inflow rate is (Das et al. 2001) given by,

$$R_{\dot{m}} = \frac{\Omega_{out}}{\Omega_{in}} \left(\frac{f_0}{4\gamma} \right)^3 \frac{R}{2} \left[\frac{4}{3} \left(\frac{8(R-1)}{R^2} - 1 \right) \right]^{3/2}. \tag{5.5}$$

Here we have used $n = 3$ for a relativistic flow. In Fig. 5.2 we have plotted the variation of $R_{\dot{m}}$ (in percentage) with R, for different opening angles Φ of the jet. For drawing Fig. 5.2, Ω_{in} is kept constant ($\Psi = 32°$). The angle Φ is varied from $30°$, $40°$, $50°$, $58°$ and $60°$, the corresponding curves are 1, 2, 3, 4 and 5, respectively. In our simulation, we have generally used $\Phi = 58°$ (Plot 4, Fig. 5.2). This is the highest value of Φ we can choose for our system because, for Φ more than $58°$ the disk would be evacuated (e.g., Plot 5, where for $\Phi = 60°$ maximum P_m is more than 100%). Thus we have chosen Φ to be smaller than this in order that steady jets are produced. The velocity variation inside the jet is obtained from the outflow branch of Bondi solution. Using P_m and the velocity of matter inside it we compute the density variation inside the jet.

5.2.2   Source of Soft Photons

The soft photons are produced from a Keplerian disk whose inner edge coincides with the CENBOL surface, while the outer edge is located at $500r_g$. The source of soft photons have the same multi-color blackbody spectrum as described in Section 4.2, coming from a standard SS73 disk. The soft photons are generated isotropically between the inner and outer edge of the Keplerian disk but their positions are randomized using the distribution function (Eqn. 4.5) of black body temperature $T(r)$. All the results of the simulations presented here have used the number of
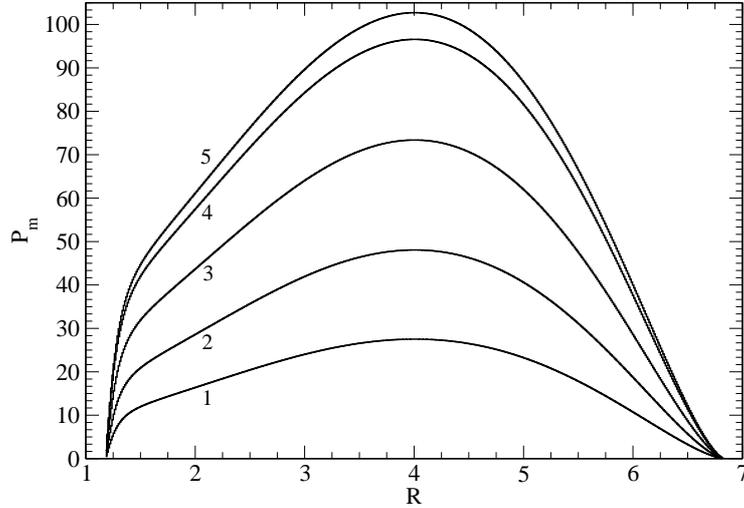
Figure 5.2: Percentage of matter $P_m = 100 \times R_{\dot{m}}$ inside the jet as a function of the compression ratio R of the inflow when the outflow is adiabatic. Plots 1-5 are for different jet angles (30°, 40°, 50°, 58° and 60°, respectively). In simulations presented in this Chapter, we have used the jet angle to be 58° (Plot 4).

injected photons to be 6.4×10^8. In the above equations, the mass of the black hole M_{bh} is measured in units of the mass of the Sun $(M_\odot)$, the disk accretion rate $\dot{M}_{d17}$ is in units of 10^{17} gm/s. We chose $M_{bh} = 10$ and $\delta r = 0.5 r_g$.

5.3   Simulation Procedure

In a given simulation, we assume a Keplerian disk rate and a sub-Keplerian halo rate to be given. The specific energy of the halo determines hydrodynamic properties (such as number density of the electrons and the velocity variation) and the thermal properties of matter. Since we chose the PW80 potential, the radial velocity is not exactly unity at $r = 1$, the horizon, but it becomes unity just outside. In order not to over-estimate the effects of bulk motion Comptonization which is due to the momentum transfer of the moving electrons to the horizon, we shift the horizon just outsize $r = 1$ where the velocity is unity. The shock location of the CENBOL is chosen where the Mach number $M = 2$ for simplicity and the compression ratio at the shock is assumed to be a free parameter. These simplifying assumptions are not expected to affect our conclusions. Photons are generated from the Keplerian disk according to the prescription in SS73 as mentioned before and are injected into the

sub-Keplerian halo, the CENBOL and the outflowing jet.

Generally, the same simulation procedure as in Chapter 4 is used, except that we are now counting also those photons which were scattered at least once by the outflow. To highlight our point, we are especially choosing the cases when the jet could play a major role in shaping the spectrum.

5.4   Results

5.4.1   When the Outflow is Present

First, we consider the cases where the outflow is present. In Figs. 5.3(a-c) we present the velocity, electron number density and temperature variations as a function of the radial distance from the black hole for specific energy $\epsilon = 0.015$. $\dot{m}_d = 0.01$ and $\dot{m}_h = 1$ were chosen. Three cases were run by varying the compression ratio R. These are given in Col. 2 of Table 5.1. The corresponding percentage of matter going in the outflow is also given in Col. 2. In the left panel, the bulk velocity variation is shown. The solid, dotted and dashed curves are the same for $R = 2$ (Case 1a), 4 (Case 1b) and 6 (Case 1c) respectively. The same line style is used in other panels. The velocity variation within the jet does not change with R, but the density (in the unit of cm^{-3}) does (middle panel) as the amount of matter inside the jet changes with R. The doubledot-dashed line gives the velocity variation of the matter within the jet for all the above cases. The arrows show the direction of the bulk velocity (radial direction in accretion, vertical direction in jets). The last panel gives the temperature (in keV) of the electron cloud in the CENBOL, jet, sub-Keplerian and Keplerian disk. Big dash-dotted line gives the temperature profile inside the Keplerian disk.

Table 5.1: Summary of the simulation parameters where outflow is present (GG10).

Case	R, P_m	N_{int}	N_{cs}	N_{cenbol}	N_{jet}	N_{subkep}	N_{cap}	p	α
1a	2, 58	2.7E8	4.0E8	1.4E7	7.5E7	8.4E8	3.4E5	63	0.43
1b	4, 97	2.7E8	4.1E8	2.4E6	1.3E8	8.6E8	3.3E5	65	1.05
1c	6, 37	2.7E8	4.0E8	5.4E7	4.8E7	8.3E8	3.1E5	62	-0.4

In Table 5.1, we summarize the parameters of all the Cases. We present the corresponding results in Fig. 5.3(a-c). In Col. 1, various Cases are marked. In Col. 2, the compression ratio (R) and percentage P_m of the total matter that is going out as outflow (Fig. 5.2) are listed. In Col. 3, we show the total number of photons (out of the total injection of 6.4×10^8) intercepted by the CENBOL and jet (N_{int}) combined. Column 4 gives the number of photons (N_{cs}) that have suffered
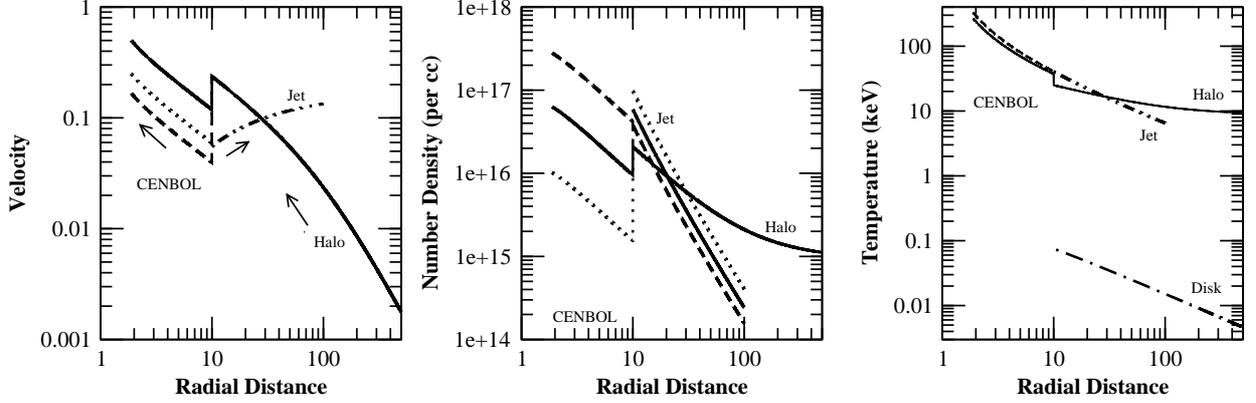
Figure 5.3: **(a-c)**: Velocity (left), density (middle) and the temperature (right) profiles of Cases 1(a-c) as described in Table 5.1 are shown with solid ($R = 2$), dotted ($R = 4$) and dashed ($R = 6$) curves. $\dot{m}_d = 0.01$ and $\dot{m}_h = 1$ were used (GG10).

scattering inside the flow. Columns 5, 6 and 7 show the number of scatterings which took place in the CENBOL (N_{cenbol}), in the jet (N_{jet}) and in the pre-shock sub-Keplerian halo (N_{subkep}) respectively. A comparison of them will give the relative importance of these three sub-components of the sub-Keplerian disk. The number of photons captured (N_{cap}) by the black hole is given in Col. 8. In Col. 9, we give the percentage p of the total injected photons that have suffered scattering through CENBOL and the jet. In Col. 10, we present the energy spectral index α ($I(E) \sim E^{-\alpha}$) obtained from our simulations.

In Fig. 5.4, we show the variation of the spectrum in the three simulations presented in Figs. 5.3(a-c). The dashed, dash-dotted and doubledot-dashed lines are for $R = 2$ (Case 1a), $R = 4$ (Case 1b) and $R = 6$ (Case 1c) respectively. The solid curve gives the spectrum of the injected photons. Since the density, velocity and temperature profiles of the pre-shock, sub-Keplerian region and the Keplerian flow are the same in all these cases, we find that the difference in the spectrum is mainly due to the CENBOL and the jet. In the case of the strongest shock (compression ratio $R = 6$), only 37% of the total injected matter goes out as the jet. At the same time, due to the shock, the density of the post-shock region increases by a factor of 6. Out of the three cases, the effective density of the matter inside the CENBOL is the highest and that inside the jet is the lowest in this case. Again, due to the
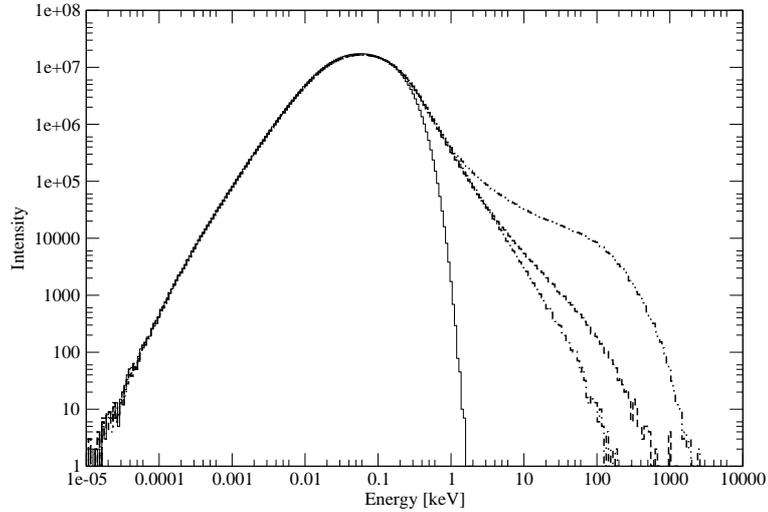
Figure 5.4: Variation of the emerging spectrum for different compression ratios. The solid curve is the injected spectrum from the Keplerian disk. The dashed, dash-dotted and doubledot-dashed lines are for $R = 2$ (Case 1a), $R = 4$ (Case 1b) and $R = 6$ (Case 1c) respectively. The disk and halo accretion rates used for these cases are $\dot{m}_d = 0.01$ and $\dot{m}_h = 1$. See, text for details (GG10).

shock, the temperature increases inside the CENBOL and hence the spectrum is the hardest. Similar effects are seen for moderate shock ($R = 4$) and to a lesser extent, the low strength shock ($R = 2$) also. When $R = 4$, the density of the post-shock region increases by the factor of 4 while almost 97% of total injected matter (Fig. 5.2) goes out as the jet reducing the matter density of the CENBOL significantly. From Table 5.1 we find that the N_{cenbol} is the lowest and N_{jet} is the highest in this case (Case 1b). This decreases the up-scattering and increases the down-scattering of the photons. This explains why the spectrum is the softest in this case. In the case of low strength shock ($R = 2$), 57% of the inflowing matter goes out as jet, but due to the shock, the density increases by a factor of 2 in the post-shock region. This makes this case similar to a non-shock case as far as the density is concerned, but with a little higher temperature of the CENBOL due to the shock. So the spectrum with the shock would be harder than when the shock is not present. The disk and the halo accretion rates used for these cases are $\dot{m}_d = 0.01$ and $\dot{m}_h = 1$.

In Figs. 5.5(a-c), we show the components of the emerging spectrum for all the three cases presented in Fig. 5.4. The solid curve is the intensity of all the photons which suffered at least one scattering. The dashed curve corresponds to the photons those suffered their last scattering from the CENBOL region and the dash-dotted

curve is for the photons those suffered last scattering in the jet region. We find that the spectrum from the jet region is softer than the spectrum from the CENBOL. As N_{jet} increases and N_{cenbol} decreases, the spectrum from the jet becomes softer because of two reasons. First, the temperature of the jet is lesser than that of the CENBOL, so the photons get lesser amount of energy from thermal Comptonization making the spectrum softer. Second, the photons are down-scattered by the outflowing jet which eventually make the spectrum softer. We note that a larger number of photons are present in the spectrum from the jet than the spectrum from the CENBOL, which shows the photons have actually been down-scattered. The effect of down-scattering is larger when $R = 4$. For $R = 2$ also there is significant amount of down scattered photons. But this number is very small for the case $R = 6$ as N_{cenbol} is much larger than N_{jet} so most of the photons get up-scattered. The difference between total (solid) and the sum of the other two regions gives an idea of the contribution from the sub-Keplerian halo located in the pre-shock region. In our choice of geometry (half angles of the disk and the jet), the contribution of the pre-shock flow is significant. In general it could be much less. This is especially true when the CENBOL is further out.

We now turn our attention to the effect of the variation of jet-angle on the output spectrum. In Fig. 5.6b, we have plotted the spectra for three different jet angles [$\Phi = 30°$ (dashed curve), $50°$ (dash-dotted curve) and $58°$ (solid curve)], keeping $\Psi = 32°$ and $R = 4$, fixed. Parameters used for the simulation: $\epsilon = 0.015$. $\dot{m}_d = 0.01$ and $\dot{m}_h = 1$. The temperature and velocity distribution of the remain same for all these three cases, only difference the change in Φ makes is in the density of the matter inside the CENBOL. In Fig. 5.6a we plot the density variation with radial distance. The line styles for $\Phi = 30°$, $50°$ and $58°$ are same as Fig. 5.6b. Here, dotted plot gives the density inside the jet for all the three cases. With the decrease in jet angle the density of the infalling matter inside the CENBOL increases, thus increasing the number of upscattered photons which makes the spectrum harder.

5.4.2   When the Outflow is Absent

Let us now consider the cases where the jet is absent ($R = 1$). In Figs. 5.7(a-c), we show the velocity (left), number density of electrons (middle) and temperature (right) profiles of Cases 2(a-c) as described in Table 5.2. Here we have fixed $\dot{m}_d = 1.5$ and $\dot{m}_h$ is varied: $\dot{m}_h = 0.5$ (solid), 1 (dotted) and 1.5 (dashed). To study the effects of bulk motion Comptonization, the temperature of the electron cloud has been kept low for these cases. The temperature profile in the different cases has been chosen according to the Fig. 3b of CT95. In the absence of any shock ($R = 1$) the Keplerian disk extends up to the marginally stable orbit ($3r_g$). The temperature profile of the
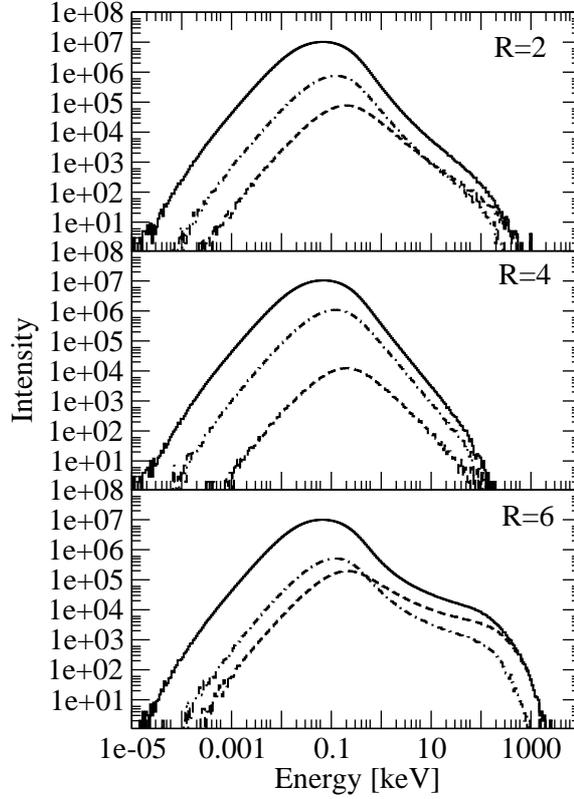
Figure 5.5: **(a-c)**: Variation of the components of the emerging spectrum with the shock strength (R). The dashed curves correspond to the photons emerging from the CENBOL region and the dash-dotted curves are for the photons coming out of the jet region. The solid curve is the spectrum for all the photons that have suffered scatterings. See, the text for details (GG10).

Keplerian disk for the above cases has been marked as 'Disk'.

Table 5.2: Summary of the simulation parameters where outflow is absent (GG10).

Case	$\dot{m}_h$, $\dot{m}_d$	N_{int}	N_{cs}	N_{ms}	N_{subkep}	N_{cap}	p	α_1, α_2
2a	0.5, 1.5	1.1E6	2.1E8	7.4E5	3.1E8	1.7E5	33.3	-0.09, 0.4
2b	1.0, 1.5	1.2E6	3.4E8	1.0E6	6.9E8	2.0E5	52.7	-0.13, 0.75
2c	1.5, 1.5	1.3E6	4.2E8	1.3E6	1.1E9	2.3E5	64.9	-0.13, 1.3

In Table 5.2, we summarize the results of simulations where we have varied $\dot{m}_d$, for a fixed value of $\dot{m}_h$. In all of these cases no jet comes out of the CENBOL (i.e., $R = 1$). In the last column, we listed two spectral slopes α_1 (from 10 to 100 keV)
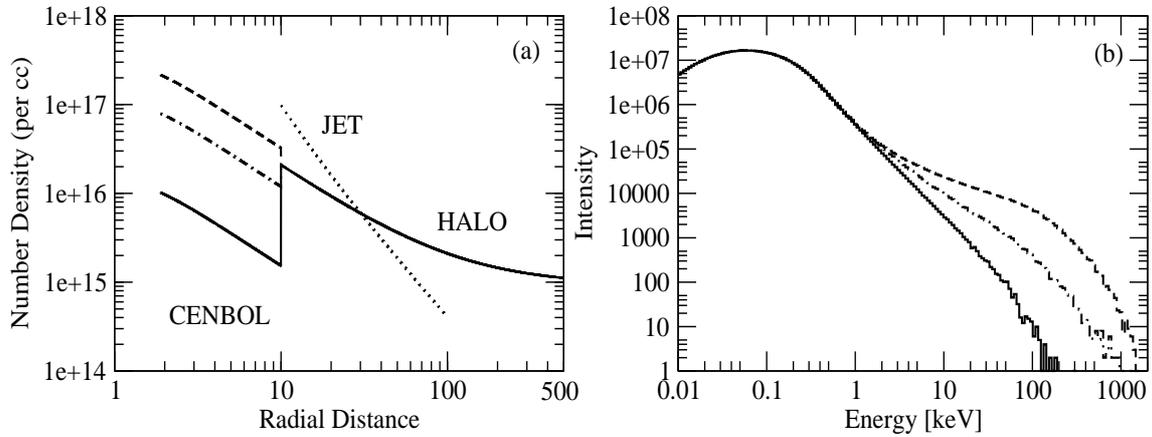
Figure 5.6: **(a-b)**: (b) The variation of the output spectrum if we vary the Jet angle is shown. Here, the dashed, dash-dotted and solid plots are for $\Phi = 30°$ and $50°$ and $58°$, respectively. Compression ratio R is 4 in all three cases. (a) The density variation with the change in Φ. Parameters and the line styles are same as the right panel. The dotted plot shows the density variation inside the outflow. See, the text for details.
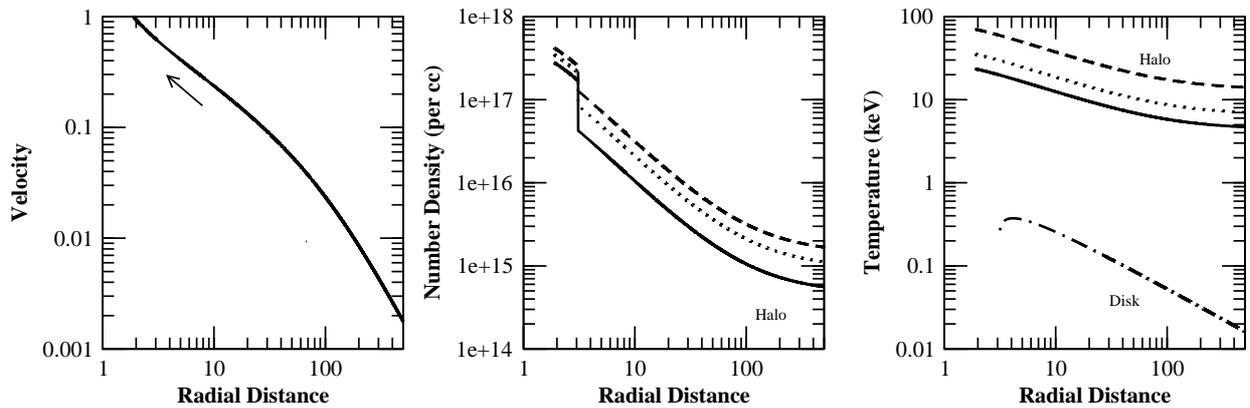

Figure 5.7: **(a-c)**: Velocity (left), density (middle) and the temperature (right) profiles of Cases 2(a-c) as described in Table 5.2 are shown with solid ($\dot{m}_h = 0.5$), dotted (1) and dashed (1.5) curves. $\dot{m}_d = 1.5$ was used throughout. Velocities are the same for all the disk accretion rates (GG10).
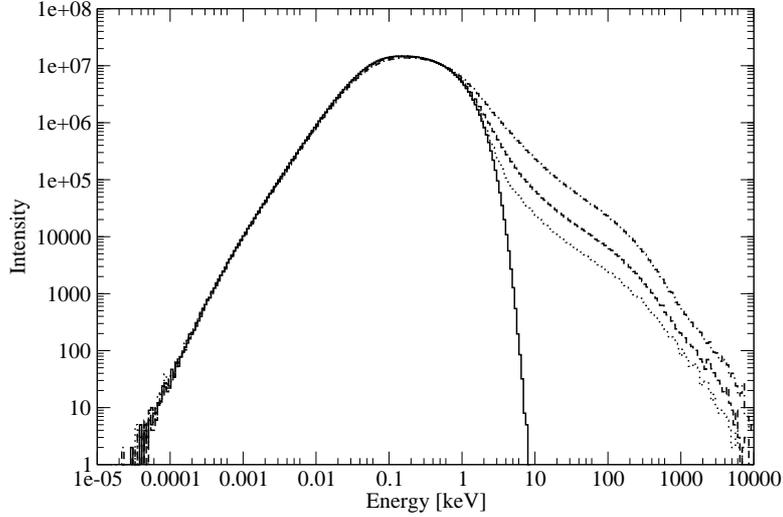
Figure 5.8: Bulk motion Comptonization spectrum. Solid (Injected), dotted ($\dot{M}_h =$ 0.5), dashed ($\dot{M}_h = 1$), dash-dotted ($\dot{M}_h = 1.5$). $\dot{M}_d = 1.5$ for all the cases. Keplerian disk extends up to $3.1r_g$. Table 5.2 summarizes the parameters used and the simulation results for these cases.

and α_2 (due to the bulk motion Comptonization). Here, N_{ms} represents the photons that have suffered scattering between $r_g = 3$ and the horizon of the black hole.

In Fig. 5.8, the emerging spectrum due to the bulk motion Comptonization when the halo rate is varied is shown. The solid curve is the injected spectrum (modified black body). The dotted, dashed, and dash-dotted curves are for $\dot{m}_h = 0.5$, 1 and 1.5 respectively. $\dot{m}_d = 1.5$ for all the cases. Table 5.2 summarizes the parameter used and the results of the simulation. As the halo rate increases, the density of the CENBOL also increases causing a larger number of scattering. From Fig. 5.7a, we noticed that the bulk velocity variation of the electron cloud is the same for all the four cases. Hence, the case where the density is maximum, the photons got energized to a very high value due to repeated scatterings with that high velocity cold matter. As a result, there is a hump in the spectrum around 100 keV energy for all the cases. We find the signature of two power-law regions in the higher energy part of the spectrum. The spectral indices are given in Table 5.2. It is to be noted that α_2 increases with $\dot{m}_h$ and becomes softer for high $\dot{m}_h$. Our geometry here at the inner edge is conical which is more realistic, unlike a sphere (perhaps nonphysically so) in Laurent & Titarchuk (2001). This may be the reason why our slope is not the same as in Laurent & Titarchuk (2001) where $\alpha_2 = 1.9$.
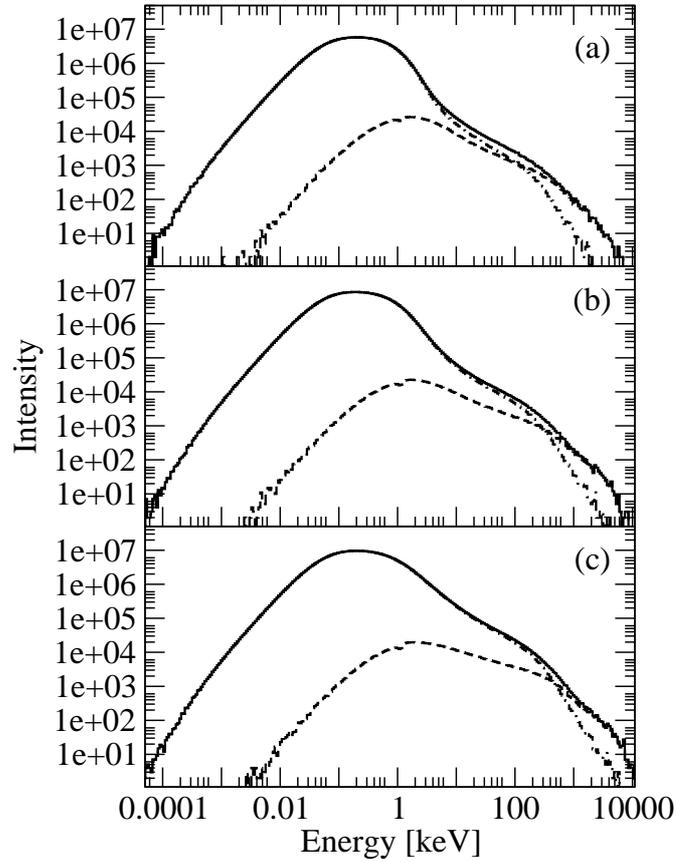
Figure 5.9: Components of the emerging spectrum for the Cases 2(a-c). Solid curves are the spectra of all the photons that have suffered scattering. The dashed and dash-dotted curves are the spectra of photons which are emitted from inside and outside of the marginally stable orbit $(3r_g)$ respectively. The photons from inside the marginally stable radius are Comptonized by the bulk motion of the infalling matter. Here the jet is absent.

In Figs. 5.9(a-c), we present the components of the emerging spectra. As in Fig. 5.5, solid curves are the spectra of all the photons that have suffered scattering. The dashed and dash-dotted curves are the spectra of photons emitted from inside and outside of the marginally stable orbit $(3r_g)$ respectively. The photons from inside the marginally stable radius are Comptonized by the bulk motion of the converging infalling matter and produces the power-law tail whose spectral index is given by α_2 (Table 5.2).

In the next Chapter we will present the results of a coupled Monte Carlo and hydrodynamic simulation. The hydrodynamic code self consistently simulates the temperature, density and velocity of the matter inside the accretion disk at each time step and the Monte Carlo code simulates the spectrum of the photons that are coming out of the electron cloud at that particular time. Here, no adhoc geometry of the Compton cloud has been assumed. The geometry of the flow is also dictated by the hydrodynamic simulation.

Chapter 6

Effects of Compton Cooling on Hydrodynamic and Spectral Properties

6.1 Introduction

In Chapters 4 and 5 we have considered steady state geometries of the accretion disk and simulated the spectrum for them. In realty one should do a time dependent simulation, where the hydrodynamics of the flow changes due to the radiative transfer in the accretion disk and the time dependence of the output spectra can be observed. Given that the two component flows have been found to be useful to understand the spectral and timing properties (Chapter 1), it will be important to carry out the numerical simulations of radiative flows around black holes which also include shocks. So far, however, only bremsstrahlung or pseudo-Compton cooling have been added into the time-dependent flow (MSC96; Chakrabarti et al. 2004). In the present Chapter, we present the time dependent simulation results which includes both hydrodynamics and radiative transfer (Ghosh et al. 2011). We use the low angular momentum halo along with a Keplerian disk. We find how the Comptonization affects the temperature distribution of the flow and how this in turn affects the dynamics of the flow as well. So far, our solutions have been steady. We obtain the outgoing spectrum of radiation as well.

In the next Section, we discuss the geometry of the soft photon source and the Compton cloud in our Monte-Carlo simulations. The variation of the thermo-dynamic quantities and other vital parameters inside the Keplerian disk and the Compton cloud which are required for the Monte-Carlo simulations are given in §6.2. In §6.3, we describe the simulation procedure and in §6.4, we present the results of our simulations.

6.2   System Description

We present cartoon diagrams of our simulation set up for (a) spherical Compton cloud (halo) with zero angular momentum (specific angular momentum $\lambda = 0$) and (b) rotating Compton cloud (halo) with a specific angular momentum $\lambda = 1$ in Figs. 6.1(a-b). In the first case (a), we have the electron cloud within a sphere of radius $R_{in} = 200r_g$, the Keplerian disk resides at the equatorial plane. The outer edge of this disk is assumed to be at $R_{out} = 300r_g$ and it extends up to the marginally stable orbit $R_{ms} = 3r_g$. At the centre of the sphere, a black hole of mass $10M_\odot$ is located. The spherical matter is injected into the sphere from the radius R_{in} from all directions. It intercepts the soft photons emerging out of the Keplerian disk and reprocesses them via Compton or inverse Compton scattering. In the second case (b), due to the presence of the angular momentum of the flow, the spherical symmetry of the flow is lost. Because of the centrifugal barrier, the matter slows down at some point on its way to the central black hole. The other parameters of the Keplerian disk and the halo are the same as in (a).

6.2.1   Distribution of Temperature and Density inside the Compton Cloud

A realistic accretion disk is expected to be three-dimensional. However, assuming axisymmetry, we can reduce one degree of freedom and make it a two dimentional problem. We have calculated the flow dynamics in two dimensions using a finite difference method which uses the principle of Total Variation Diminishing (TVD) to carry out hydrodynamic simulations (see, Ryu, Chakrabarti & Molteni, 1997 and references therein; Giri et al. 2010). At each time step, we carry out Monte-Carlo simulation to obtain the cooling/heating due to Comptonization. We incorporate the cooling/heating of each grid while executing the next time step of hydrodynamic simulation. The numerical calculation for the two-dimensional flow has been carried out with 900×900 cells in a $200r_g \times 200r_g$ box. We chose the units in a way that the outer boundary (R_{in}) is chosen to be unity and the matter density is normalized to become unity. We assume the black hole to be non-rotating and we use the pseudo-Newtonian potential $-\frac{1}{2(r-1)}$ (PW80) to calculate the flow geometry around a black hole (Here, r is in the unit of Schwarzschild radius $r_g = 2GM/c^2$). Velocities and angular momenta are measured in units of c, the velocity of light and $r_g c$ respectively. In Figs. 6.2(a-b) we show the snapshots of the density and temperature (in keV) profiles obtained in a steady state purely from our hydrodynamic simulation. The density contour levels are drawn for 0.65-1.01 (levels increasing by a factor of 1.05) and 1.01-66.93 (successive level ratio is 1.1). The temperature contour levels are
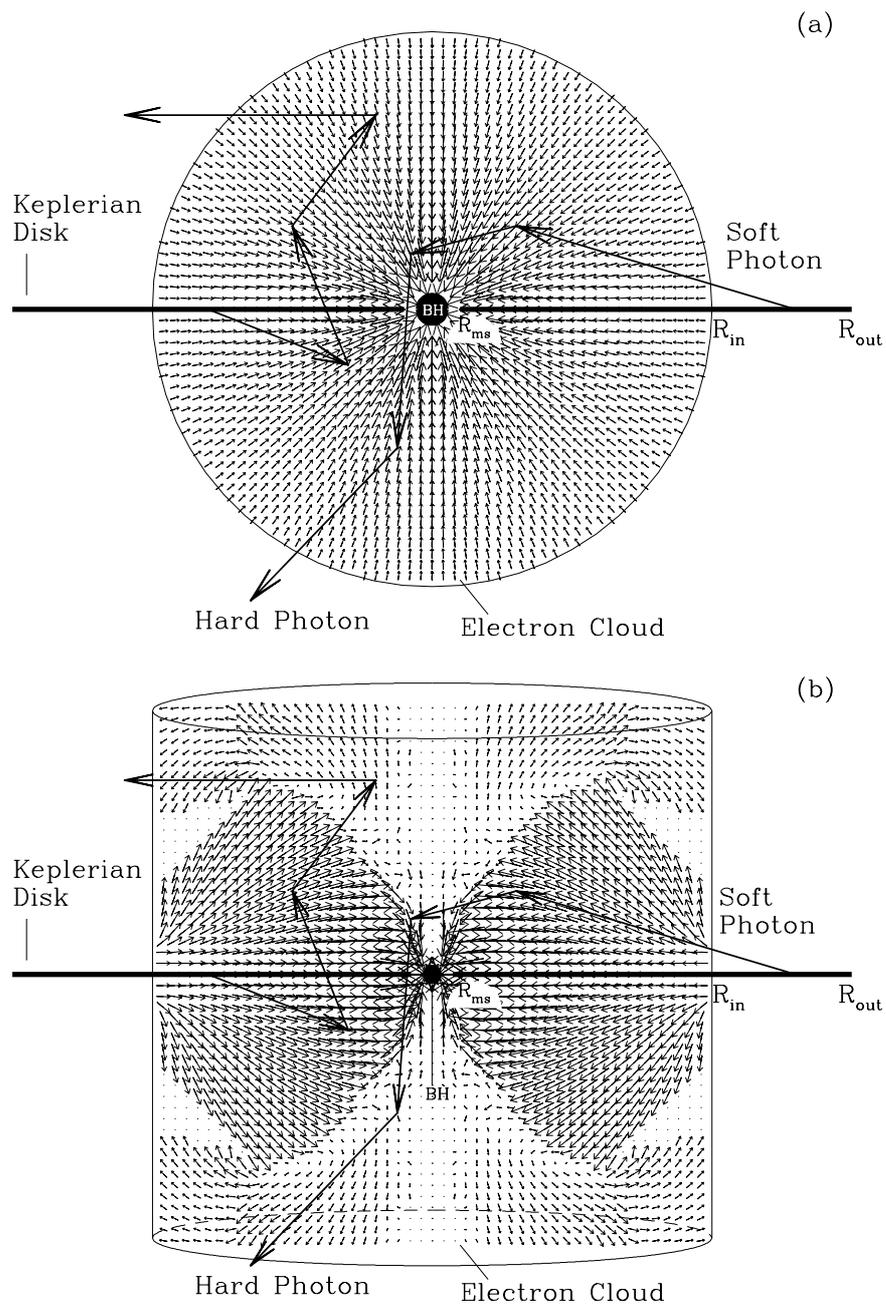
Figure 6.1: Schematic diagram of the geometry of our Monte Carlo simulations for (a) $\lambda = 0$ and for (b) $\lambda = 1$. Zigzag trajectories and velocity vectors are typical paths followed by the photons and the velocity vectors of the infalling matter inside the cloud (Ghosh et al. 2011).
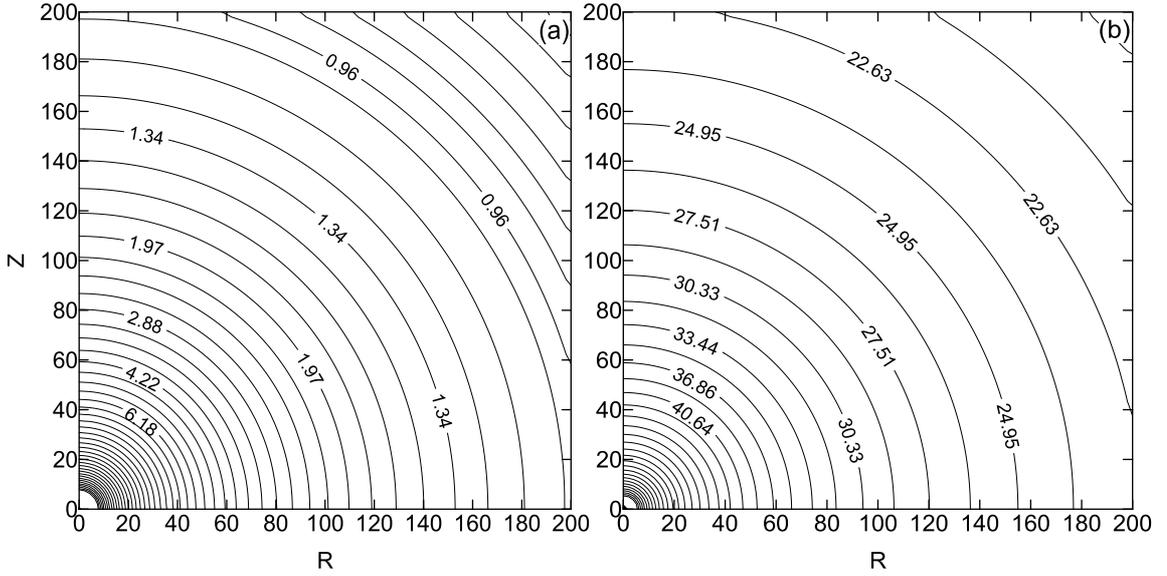
Figure 6.2: Density (a) and temperature (b) contours inside a spherical halo in the absence of Compton cooling. Here, densities are in normalized unit and temperatures are in keV. $\lambda = 0$ is chosen. See text for details (Ghosh et al. 2011).

drawn for 16.88-107.8 (successive level ratio is 1.05).

6.2.2   Properties of the Keplerian Disk

The soft photons are produced from a Keplerian disk whose inner edge has been kept fixed at the marginally stable orbit R_{ms}, while the outer edge is located at R_{out} ($300r_g$). The source of soft photons have a multicolor blackbody spectrum coming from a standard (SS73) disk. Hydrodynamic properties of the Keplerian disk is the same as described in Sec. 5.2. In the Monte-Carlo simulation, we incorporated the directional effects of photons coming out of the Keplerian disk with the maximum number of photons emitted in the z-direction and minimum number of photons are generated along the plane of the disk. Thus, in the absence of photon bending effects, the disk is invisible as seen edge on. The position of each emerging photon is randomized using the distribution function $dN(r) = 4\pi r \delta r H(r) n_\gamma(r)$, (Eqn. 4.5). We chose the mass of black hole $M_{bh} = 10$ in the rest of the Chapter.

6.3   Simulation Procedure

For a simulation, we assume a Keplerian disk rate ($\dot{m}_d$) and a sub-Keplerian halo rate ($\dot{m}_h$) to be given. The specific energy (ϵ) of the halo provides the hydrodynamic (e.g., number density of the electrons and the velocity variation) and the thermal properties of matter. Since we chose the PW80 potential, the radial velocity is not exactly unity at $r = 1$, the horizon, but it becomes unity just outside. In order not to over estimate the effects of bulk motion Comptonization (CT95) which is due to the momentum transfer of the moving electrons to the horizon, we kept the highest velocity to be 1. We use the absorbing boundary condition at $r = 1.5$ ($\lambda = 0$ case) and $r = 2.5$ ($\lambda = 1$ case). These simplifying assumptions do not affect our conclusions, especially because we are studying inviscid flow and the specific angular momentum is constant. Photons are generated from the Keplerian disk as mentioned before and may be intercepted by the sub-Keplerian halo (sphere in Fig. 6.1a and cylinder in Fig. 6.1b).

The propagation of the photon inside the electron cloud, condition for a photon to scatter with an electron, choosing the photon and electron energy and the change in photon momentum after the scattering all these processes are implemented in the Monte Carlo code by the same procedure as described in Secs. 4.2 & 5.2.

We take a steady state flow profile from a hydrodynamics code to start the Monte Carlo simulation. When a photon interacts with an electron via Compton or inverse-Compton scattering, it loses or gains some energy (ΔE). At each grid of the code we compute ΔE. We modify the energy from the flow by this amount and continue the hydrodynamic code with this modified energy. This, in turn, modify the hydrodynamic profile. Thus the Monte Carlo code for radiative transport and TVD code for hydrodynamics are coupled. In case the final state is steady, the temperature of the cloud would be reduced progressively to a steady value from the initial state where no cooling was assumed.

6.3.1   Coupling of the Hydrodynamic and Radiative Transfer Codes

Once a steady state is achieved in the non-radiative hydro-code, we compute the spectrum using the Monte Carlo code. This is the spectrum in first approximation. To include cooling in the coupled code, we follow these steps: (a) we calculate the velocity, density and temperature profiles of the electron cloud from the output of the hydro-code. (b) Using the Monte Carlo code we calculate the spectrum. (c) Electrons are cooled (heated up) by the inverse-Compton (Compton) scattering. We calculate the amount of the heat loss (gain) by the electrons and its new temperature and energy distributions and (d) taking the new temperature and energy profiles

as initial condition, we run the hydro-code for a period of time. Subsequently, we repeat the steps (a-d). In this way, we get an opportunity to see how the spectrum is modified as the iterations proceed. The iterations stop when two successive steps produce virtually the same temperature profile and the emitted spectrum.

Calculation of the Compton Cooling using Monte Carlo Code:

For the Monte Carlo simulation, we divide the Keplerian disk in different annuli of width $D(r) = 0.5$. Each annulus is characterized by its central temperature $T(r)$. The total number of photons emitted from the disk surface of each annulus can be calculated using Eqn. (4.5). This total number comes out to be $\sim 10^{39-40}$ for $\dot{m}_d = 1.0$. In reality, one cannot inject this much number of photons in Monte Carlo simulation because of the limitation of the computation time. So we replace this large number by a low number of bundles, say, $N_{comp}(r) \sim 10^7$ and calculate a weightage factor

$$f_W = \frac{dN(r)}{N_{comp}(r)}.$$

Clearly, from each annulus, the number of photons in a bundle will vary. This is computed exactly and used to compute the change of energy due to Comptonization. When this injected photon is inverse-Comptonized (or, Comptonized) by an electron in a volume element of size dV, we assume that f_W number of photons has suffered similar scatterings with the electrons inside the volume element dV. If the energy loss (gain) per electron in this scattering is ΔE, we multiply this amount by f_W and distribute this loss (gain) among all the electrons inside that particular volume element. This is continued for all the 10^7 bundles of photons and the revised energy distribution is obtained.

Computation of the Temperature Distribution after Cooling

Since the hydrogen plasma considered here is ultra-relativistic ($\gamma = \frac{4}{3}$ throughout the hydrodynamic simulation), the thermal energy per particle is $3k_BT$ where k_B is Boltzmann constant, T is the temperature of the particle. The electrons are cooled by the inverse-Comptonization of the soft photons emitted from the Keplerian disk. The protons are cooled because of the Coulomb coupling with the electrons. Total number of electrons inside any box with the centre at location (ir, iz) is given by,

$$dN_e(ir, iz) = 4\pi r n_e(ir, iz) dr dz, \tag{6.1}$$

where, $n_e(ir, iz)$ is the electron number density at (ir, iz) location, and dr and dz represent the grid size along r and z directions respectively. So, the total thermal energy in any box is given by $3k_BT(ir, iz)dN_e(ir, iz) = 12\pi r k_B T(ir, iz)n_e(ir, iz)drdz$,

where $T(ir, iz)$ is the temperature at (ir, iz) location. We calculate the total energy loss (gain) ΔE of electrons inside the box according to what is presented above and subtract that amount to get the new temperature of the electrons inside that box as

$$k_B T_{new}(ir, iz) = k_B T_{old}(ir, iz) - \frac{\Delta E}{3 d N_e(ir, iz)}. \tag{6.2}$$

6.3.2   Details of the Hydrodynamic Simulation Code

To model the initial injection of matter, we consider an axisymmetric flow of gas in the Psudo-Newtonian gravitational field of a black hole of mass M_{bh} located at the centre in the cylindrical coordinates $[R, \theta, z]$. We assume that at infinity, the gas pressure is negligible and the energy per unit mass vanishes. As mentioned before, the gravitational field of the black hole can be described by PW80 potential. We have assumed a polytropic equation of state for the accreting (or, outflowing) matter, $P = K\rho^\gamma$, where, P and ρ are the isotropic pressure and the matter density respectively, γ is the adiabatic index (assumed in this work to be constant throughout the flow, and is related to the polytropic index n by $\gamma = 1 + 1/n$) and K is related to the specific entropy of the flow s. The details of the code is described in Ryu, Molteni & Chakrabarti (1997) and in Giri et al. (2010). When we couple with cooling, K itself will change. However, it remains constant in between two successive Monte-Carlo coupling of inclusion of the cooling.

Our computational box occupies one quadrant of the R-Z plane with $0 \leq R \leq 200$ and $0 \leq z \leq 200$. The incoming gas enters the box through the outer boundary, located at $R_{in} = 200$. We have chosen the density of the incoming gas $\rho_{in} = 1$ for convenience since, in the absence of self-gravity and cooling, the density is scaled out, rendering the simulation results valid for any accretion rate. As we are considering only the energy flows while keeping the boundary of the numerical grid at a finite distance, we need the sound speed a (i.e., temperature) of the flow and the incoming velocity at the boundary points. For the spherical flow with zero angular momentum (Bondi flow), we have taken the boundary values from standard pseudo-Bondi solution. We injected the matter from both the outerboundary of R and z coordinate. In order to mimic the horizon of the black hole at the Schwarzschild radius, we placed an absorbing inner boundary at $r = 1.5 r_g$, inside which all material is completely absorbed into the black hole. For the background matter (required to avoid division by zero) we used a stationary gas with density $\rho_{bg} = 10^{-6}$ and sound speed (or temperature) the same as that of the incoming gas. Hence the incoming material has a pressure 10^6 times larger than that of the background matter. All the calculations were performed with 900×900 cells, so each grid has a size of 0.22 in units of the Schwarzschild radius. For $\lambda = 1$ case, the matter was injected from

the outerboundary of R coordinate.

All the simulations are carried out assuming a stellar mass black hole. The procedures remain equally valid for massive/super-massive black holes. We carry out the simulations till several thousands of dynamical time-scales are passed. In reality, this corresponds to a few seconds in physical units.

6.4   Results and Discussions

In Table 6.1, we summarize all the cases for which the simulations have been presented in this Chapter. In Column 1, various cases are marked. Columns 2 gives the angular momentum (λ) and the specific energy (ϵ) of the flow. The Keplerian disk rate ($\dot{m}_d$) and the sub-Keplerian halo rate ($\dot{m}_h$) are listed in Column 3. The number of soft photons, injected from the Keplerian disk (N_{inj}) for various disk rates can be found in Column 4. Columns 5 lists the number of photons (N_{sc}) that have suffered at least one scattering inside the electron cloud. The number of photons (N_{unsc}), escape from the cloud without any scattering are listed in Column 6. Columns 7 and 8 give the percentages of injected photons that have entered into the black hole (N_{bh}) and suffered scattering ($p = \frac{N_{sc}}{N_{inj}}$), respectively. The cooling time (t_0) of the system is defined as the expected time for the system to lose all its thermal energy with the particular flow parameters (namely, $\dot{m}_d$ and $\dot{m}_h$). We calculate $t_0 = E/\dot{E}$ in each time step, where, E is the total energy content of the system and $\dot{E}$ is the energy gain or loss by the system in that particular time step. Column 9 lists the cooling time in sec for each case. We present the energy spectral index α $[I(E) \sim E^{-\alpha}]$ obtained from our simulations in the last column.

6.4.1   Compton Cloud with Zero Angular Momentum ($\lambda = 0$)

First we discuss the results corresponding to the Cases 1(a-d) of Table 6.1. In Fig. 6.3(a-d) we present the changes in density distribution as the disk accretion rates are changed: $\dot{m}_d =$ (a) 1, (b) 2, (c) 5 and (d) 10 respectively. We notice that as the accretion rate of the disk is enhanced, the density distribution losses its spherical symmetry. In particular, the density at a given radius is enhanced in a conical region along the axis. This is due to the cooling of the matter by Compton scattering. To show this, in Fig. 6.4(a-d) we show the temperature contours of the same four cases. The contours are marked with temperatures. We notice that the temperature is reduced along the axis (where the optical depth as seen by the soft photons from the Keplerian disk is higher) drastically after repeated Compton scattering.
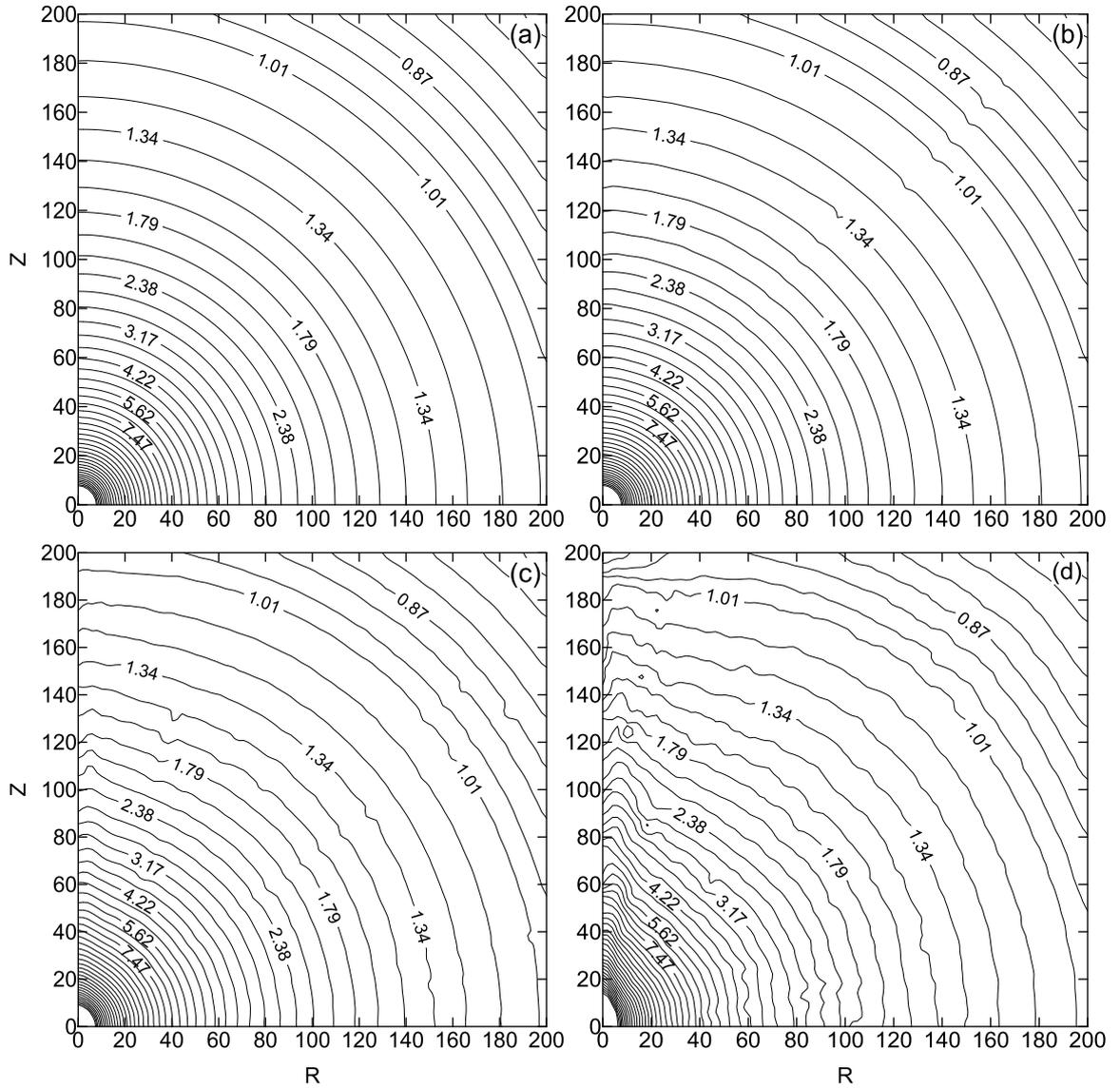
Figure 6.3: Changes in the density distribution in presence of cooling. $\lambda = 0$ and $\dot{m}_h = 1$ for all the cases. Disk accretion rate $\dot{m}_d$ used are (a) 1, (b) 2, (c) 5 and (d) 10 respectively (Cases 1(a-d) of Table 6.1). The density contours are drawn using the same contour levels as in Fig. 6.2a (Ghosh et al. 2011).
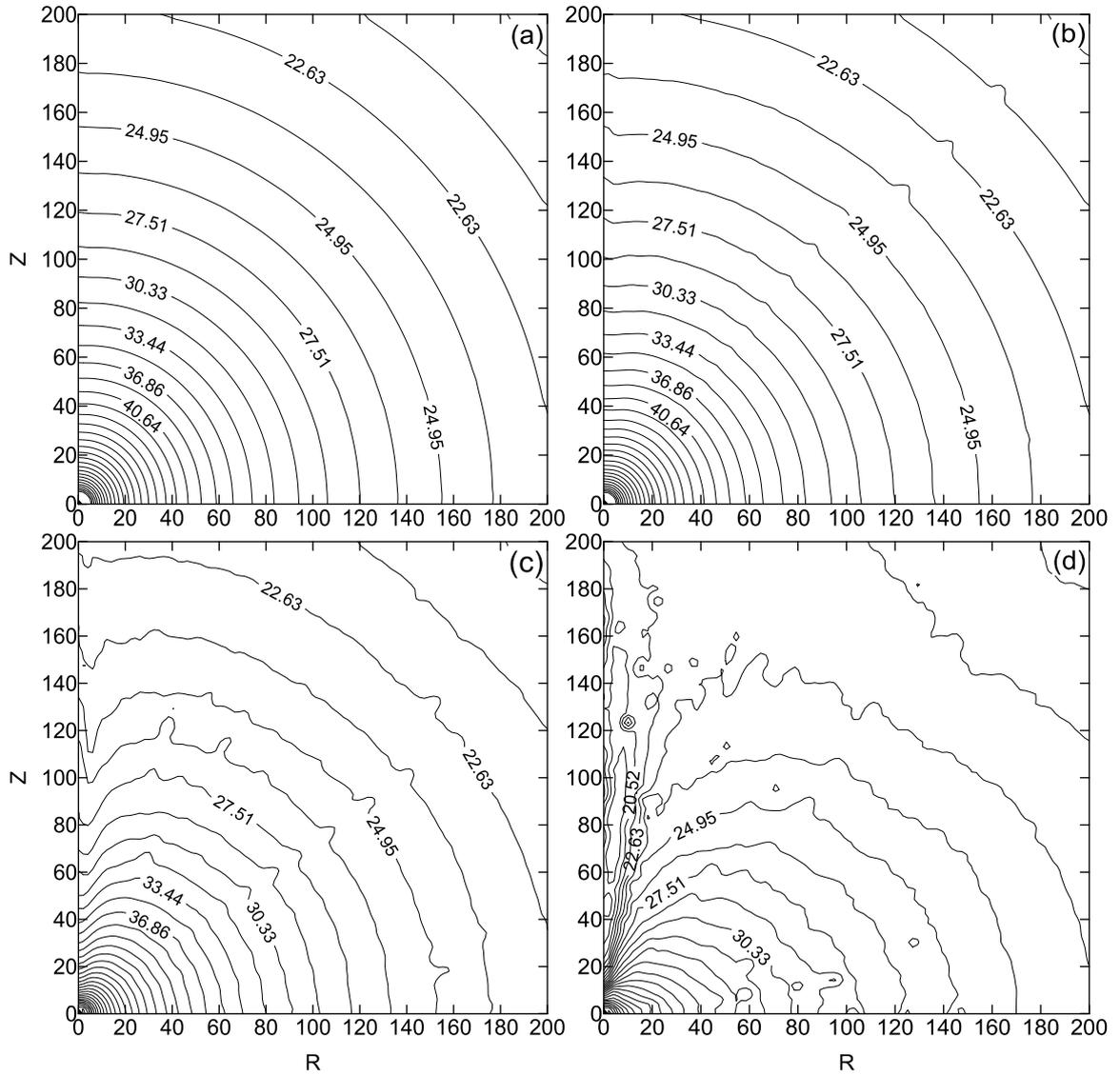
Figure 6.4: Change in the temperature distribution in presence of cooling. $\lambda = 0$ and $\dot{m}_h = 1$ for all the cases. Disk accretion rate $\dot{m}_d$ is (a)1, (b)2, (c)5 and (d)10 respectively (Cases 1(a-d) of Table 6.1). Contours are drawn using the same levels as in Fig. 6.2b (Ghosh et al. 2011).

Table 6.1: Summary of all the simulations presented in §6.4.1 and §6.4.2 (Ghosh et al. 2011).

Case	λ, ϵ	$\dot{m}_d, \dot{m}_h$	N_{inj}	N_{sc}	N_{unsc}	N_{bh} [%]	p [%]	t_0 [sec]	α
1a	0, 22E-4	1, 1	4.3E40	8.7E39	3.5E40	0.12	20.03	228.3	1.15, 0.99
1b	0, 22E-4	2, 1	1.5E41	2.9E40	1.2E41	0.12	20.02	63.6	1.30, 1.0
1c	0, 22E-4	5, 1	7.3E41	1.5E41	5.9E41	0.12	19.94	12.4	1.40, 0.96
1d	0, 22E-4	10, 1	2.5E42	5.0E41	2.0E42	0.12	19.82	4.2	1.65, 0.90
1e	0, 22E-4	1, 0.5	4.3E40	4.7E39	3.9E40	0.07	10.89	380.0	1.57
1f	0, 22E-4	1, 2	4.3E40	1.5E40	2.8E40	0.23	34.32	118.9	1.1
1g	0, 22E-4	1, 5	4.3E40	2.6E40	1.8E40	0.50	59.01	48.0	0.7
1h	0, 22E-4	1, 10	4.3E40	3.3E40	1.1E40	0.70	75.52	35.1	0.45
2a	1, 3E-4	1, 1	6.3E40	1.2E40	5.1E40	0.29	19.20	79.7	0.88
2b	1, 3E-4	2, 1	2.1E41	4.1E40	1.7E41	0.28	19.28	21.9	0.94
2c	1, 3E-4	5, 1	1.0E42	1.9E41	8.1E41	0.28	19.21	4.3	1.03
2d	1, 3E-4	10, 1	3.6E42	6.9E41	2.9E42	0.29	18.94	1.4	1.17
2e	1, 3E-4	10, 0.5	3.6E42	3.9E41	3.2E42	0.19	10.77	1.9	1.37
2f	1, 3E-4	10, 1.5	3.6E42	9.3E41	2.7E42	0.37	25.49	1.1	1.01
2g	1, 3E-4	10, 2	3.6E42	1.1E42	2.5E42	0.44	30.76	0.9	0.95
2h	1, 3E-4	10, 5	3.6E42	1.8E42	1.7E42	0.69	51.07	0.7	0.59

In Fig. 6.5 and Fig. 6.6, we show the hydrodynamic and radiative properties. In Fig. 6.5a, we show the sonic surfaces. The lowermost curve corresponds to theoretical solution for an adiabatic flow (e.g., C90). Other curves from the bottom to top are the iterative solutions for the Case 1d mentioned above. As the disk rate is increased, the cooling increases the Mach number along the axis at a give distance. Of course, there are other effects: The cooling causes the density to go up to remain in pressure equilibrium. In Fig. 6.5b, the Mach number variation is shown. The lower most curve (marked 1) from theoretical consideration. Plots 2-4 are the variation of Mach number with radial distance along the equatorial plane, along the diagonal and along the vertical axis respectively. In Fig. 6.6a, the average temperature of the spherical halo is plotted with iteration time until almost steady state is reached. The cases are marked on the curves. We note that as the injection of soft photons is increased, the average temperature of the halo decreases drastically. In Fig. 6.6b, we have plotted the energy dependence of the photon intensity. We find, as we increase the disk rate, keeping the halo rate fixed, number of photons coming out of the cloud in a particular energy bin increases and the spectrum becomes softer. This is also clear from Table 6.1, N_{inj} increases with $\dot{m}_d$, increasing α. We find the signature of double slope in these cases. As the disk rate increases, the second slope becomes steeper. This second slope is the signature of bulk motion Comptonization. As $\dot{m}_d$ increases, the cloud becomes cooler (Fig. 6.6a) and the power-law tail due to the bulk motion Comptonization (CT95) becomes prominent.
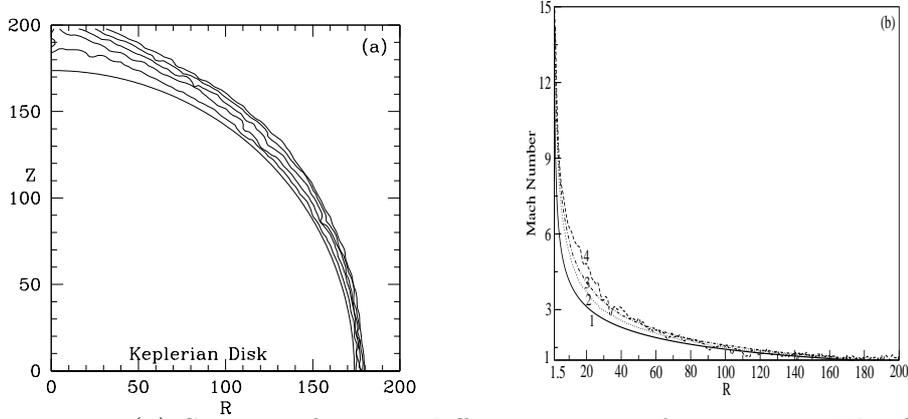
Figure 6.5: (a) Sonic surfaces at different stages of iterations. The final curve represents the converged solution. The initial spherical sonic surface become prolate spheroid due to the presence of the Keplerian disk at the equatorial plane. Parameters are for Case 1d (Table 6.1). (b) Mach number variation as a function of distance after a complete solution of the radiative flow is obtained. Plot no. 1 corresponds to the solution from adiabatic Bondi flow. Plots 2-4 are the solutions along the equatorial plane, the diagonal and the axis of the disk. Parameters are for Case 1d (Table 6.1) (Ghosh et al. 2011).

In Fig. 6.7a, we show the variation of the energy spectrum with the increase of the halo accretion rate, keeping the disk rate ($\dot{m}_d = 1$) and angular momentum of the flow ($\lambda = 0$) fixed. The dotted, dashed, dash-dotted, double dot-dashed and double dash-dotted curves show the spectra for $\dot{m}_h = 0.5, 1, 2, 5$ and 10 respectively. The spectrum becomes harder for higher values of $\dot{m}_h$ as it becomes difficult to cool. The injected multicolor blackbody spectrum supplied by the Keplerian disk is shown (solid line). The spectrum becomes harder for higher values of $\dot{m}_h = 1$ as it is difficult to cool a higher density matter with the same number of injected soft photons. In Fig. 6.7b, we show the directional dependence of the spectrum. For $\lambda = 0$, $\dot{m}_h = 2$, $\dot{m}_d = 1$ (Case 1f Table 6.1). The solid, dotted and dashed curves are for observing angles (a) 2°, (b) 45° and (c) 90° respectively. All the angles are measured with respect to the rotation axis (z-axis). As expected, the photons arriving along the Z-axis would be dominated by the soft photons from the Keplerian disk while the power-laws would dominate the spectrum coming edge-on.

We now study the dependence of the spectrum on the time delay between injected and outgoing photons. Depending on number of scatterings suffered and length of the path traveled, different photons spend different times inside the Compton cloud.
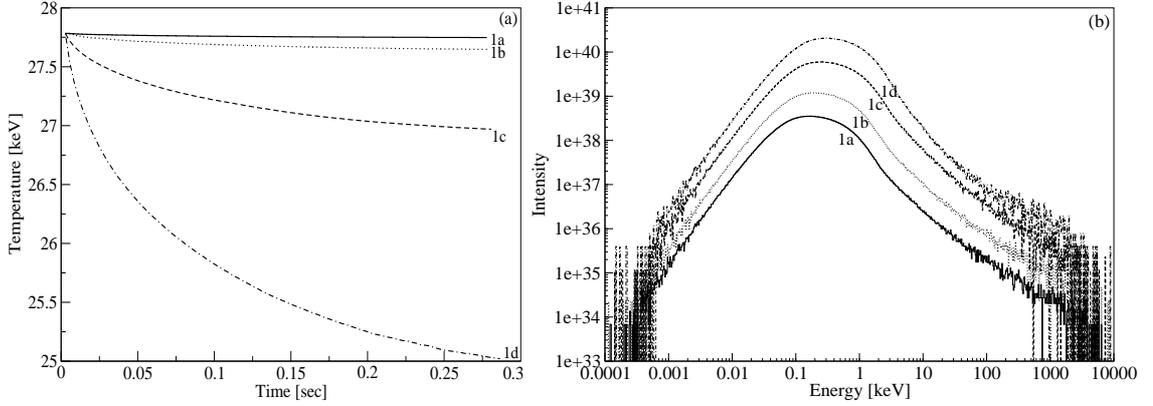
Figure 6.6: (a) Variation of the average temperature of the Compton cloud as the iteration proceeds when the disk accretion rate is varied. $\dot{m}_h = 1$. The solid, dotted, dashed and dash-dotted plots are for $\dot{m}_d = 1, 2, 5$ and 10 respectively. Case numbers (Table 6.1) are marked. With the increase of disk rate, the temperature of the Compton cloud converges to a lower temperature. (b) Variation of the spectrum with the increase of disk accretion rate. Parameters are the same as in (c). With the increase in $\dot{m}_d$, the intensity of the spectrum increases due to the increase in N_{inj} (see Table 6.1). The spectrum is softer for the higher value of $\dot{m}_d$. Spectral slopes for each of these spectra are listed in Table 6.1 (Ghosh et al. 2011).

The energy gain or loss by any photon depends on this time. Fig. 6.8a shows the spectrum of the photons suffering different number of scatterings inside the cloud. Here the numbers 1, 2, 3, 4, 5 and 6 show the spectrum for 6 different ranges of number of scatterings. Plot 1 shows the spectrum of the photons that have escaped from the cloud without suffering any scattering. This spectrum is nearly the same as the injected spectrum, only difference is that it is Doppler shifted. As the number of scattering increases (spectra 2, 3 and 4), the photons get more and more energies via inverse Compton scattering with the hot electron cloud. For scatterings more than 19, the high energy photons start loosing energy through Compton scattering with the relatively lower energy electrons. Components 5 and 6 show the spectra of the photons suffering 19-28 scatterings and the photons suffering more than 28 respectively. Here the flow parameters are: $\dot{m}_d = 1$, $\dot{m}_h = 10$ and $\lambda = 0$ (Case 1h Table 6.1).

In Fig. 6.8b, we plot the spectrum emerging out of the electron cloud at four different time ranges. In the simulation, that the photons take 0.01 to 130 ms to come out of the system. We divide this time range into 4 suitable bins and plot their spectrum. Case 1h of Table 6.1 is considered. We observe that the spectral slopes
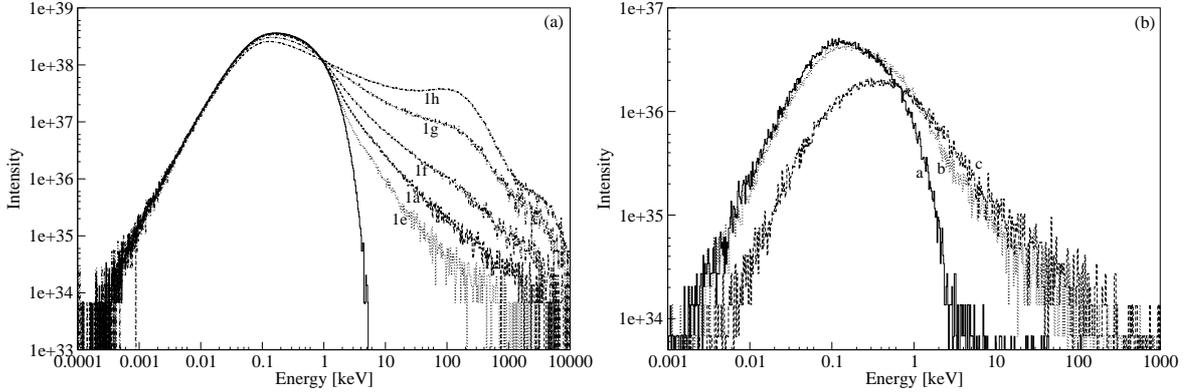
Figure 6.7: (a) Variation of the spectrum with the increase of the halo accretion rate, keeping the disk rate ($\dot{m}_d = 1$) and angular momentum of the flow ($\lambda = 0$) fixed. The dotted, dashed, dash-dotted, double dot-dashed and double dash-dotted curves show the spectra for $\dot{m}_h = 0.5$, 1, 2, 5 and 10 respectively. The injected multicolor blackbody spectrum supplied by the Keplerian disk is shown (solid line). (b) Directional variation in the spectrum: $\lambda = 0$, $\dot{m}_h = 2$, $\dot{m}_d = 1$ is shown. The solid, dotted and dashed curves are for observing angles 2°, 45° and 90° respectively. All the angles are measured with respect to the rotation axis (z-axis) (Ghosh et al. 2011).

and intensities of the four spectra are different. As the photons spend more and more time inside the cloud, the spectrum gets harder (plots 1, 2 and 3). However, very high energy photons which spend maximum time inside the cloud lose some energy to the relatively cooler electrons before escaping from the cloud. Thus, the spectrum 4 is actually the spectrum of Comptonized photons.

6.4.2   Compton Cloud with Very Low Angular Momentum ($\lambda = 1.0$)

We now turn our attention to the case where the cloud is formed by a low angular momentum flow. In this case, the flow is already axisymmetric and due to the centrifugal force, a weak shock wave, or at least a pressure wave would be formed. In Fig. 6.9(a-b), we show the contours of constant density (Fig. 6.9a) and temperature (Fig. 6.9b) when no radiative transfer is included. Here the specific angular momentum of $\lambda = 1$ was chosen. Density contour levels are drawn from 0.001-55.35 (successive level ratio is 1.5), 55.35-73.73 (successive level ratio is 1.1). Temperature contour levels are drawn from 2.3-11.64 (successive level ratio is 1.5), 11.64-64.71 (successive level ratio is 1.1). We note that a shock has been formed which bends
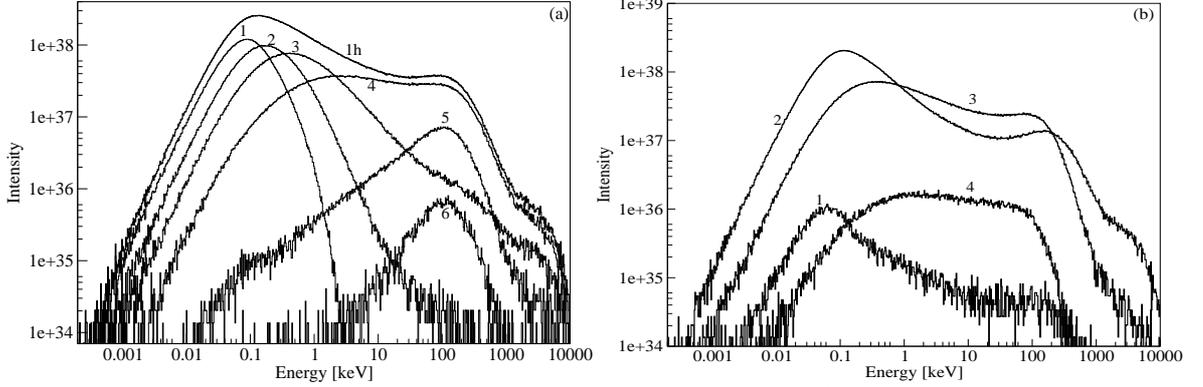
Figure 6.8: Intensity spectra emerging from the cloud (a) after suffering various number of scatterings and (b) at four different times immediately after the injection of soft photons. Case 1h is assumed. In the left panel (a), the spectra of the photons suffering 0, 1-2, 3-6, 7-18, 19-28 and more than 29 scatterings are shown by the plots 1, 2, 3, 4, 5 and 6 respectively, within the cloud. Curve 1h is the net spectrum for which these components are drawn. As the number of scattering increases, the photons gain more and more energy from the hot electron cloud through inverse Comptonization process. In Panel b, the spectra of the photons spending 0.01-1, 1-40, 40-100 and more than 100 ms time inside the electron cloud are marked by 1, 2, 3 and 4 respectively (Ghosh et al. 2011).

outwards away from the equatorial plane (Ryu, Chakrabarti & Molteni, 1997; Giri et al., 2010.).

In Fig. 6.10(a-d), we show the results of placing a Keplerian disk in the equatorial plane. The inner edge is located at $3r_g$, the marginally stable orbit. Here, $\dot{m}_h = 1$ and $\dot{m}_d =$ (a) 1, (b) 2, (c) 5 and (d) 10 respectively (Cases 2(a-d) of Table 6.1). The densities used to draw the contours are the same as that in Fig. 6.9a. As the Keplerian disk rate is increased, the intensity of soft photons interacting with the high optical depth (post-shock) region is increased. In Fig. 6.10d, we observe that the conical region around the axis is considerably cooler. Thus, the density around the shock is enhanced. However, most importantly, with the increase in disk accretion rate, i.e., cooling, the shock location moves in closer to the black hole. This result has been already demonstrated in the context of the bremsstrahlung cooling (MSC96) inside the sub-Keplerian flow.

In Fig. 6.11(a-d), we present the corresponding temperature distribution. The parameters are the same as in Fig. 6.10(a-d) and the temperatures used to draw the contours are the same as that in Fig. 6.9b. The Comptonization in the shocked
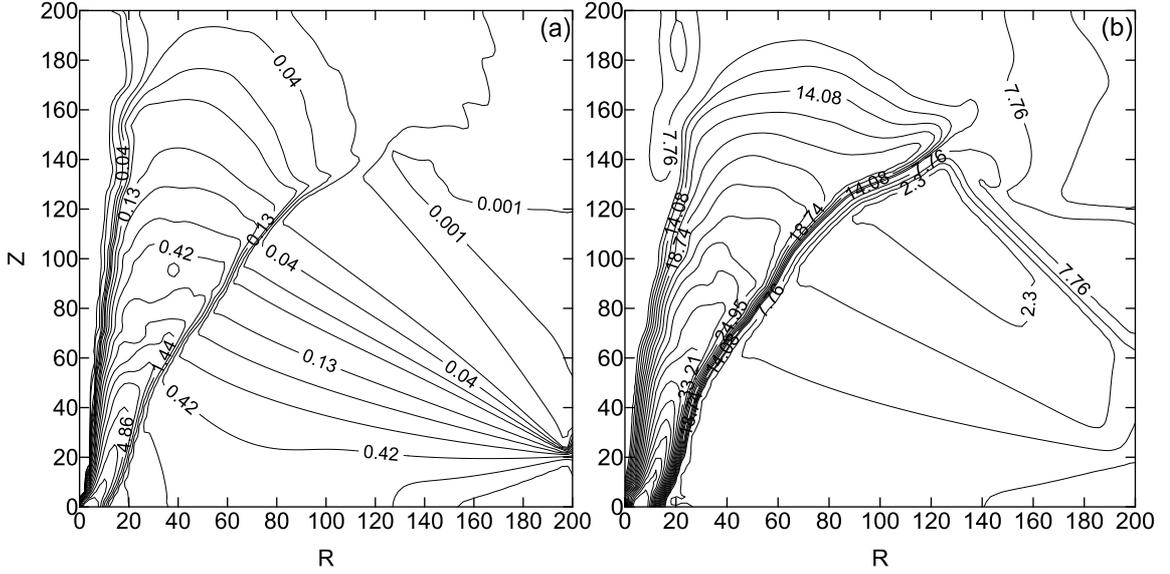
Figure 6.9: Density (a) and temperature (b) contours inside the halo ($\lambda = 1.0$) in the absence of Compton cooling. Densities are in normalized unit and temperatures are in keV. See, text for details (Ghosh et al. 2011).

region cools it down considerably. Otherwise, not enough visible changes in the thermodynamic variables are seen. To understand the detailed effects of the radiative transfer on the dynamics of the flow, we take the differences in the pressure and velocity at each grid point of the flow for Cases 1d and 2d of Table 6.1.

In Fig. 6.12(a-b), we show the difference between the results of a purely hydro-dynamical flow and the results by taking the Comptonization into account. Fig. 6.12a is for the flow with no angular momentum and Fig. 6.12b is drawn for the specific angular momentum $\lambda = 1$. The contours are of constant $\Delta P = P_c - P_a$, where P is the pressure and the subscripts c and a represent the pressure with and without cooling respectively. The arrows represent the difference in velocity vectors in each grid. As expected, in both the cases the changes are maximum near the axis. The fractional changes in pressures and velocities are anywhere between ~ 0 (outer edge) and $\sim 25\%$ (inner edge and near the axis). Because of the shifts of the shock location towards the axis, the variation of the velocity is also highest in the vicinity of the shock. Thus we prove that not only the symmetry is lost by the insertion of an axisymmetric soft photon source, the cooling process also plays a major role in deciding the dynamics of the flow.

We now turn our attention to the dynamical variables and the spectral behavior of the rotating flow. In Fig. 6.13a, we show the variation of the average temperature
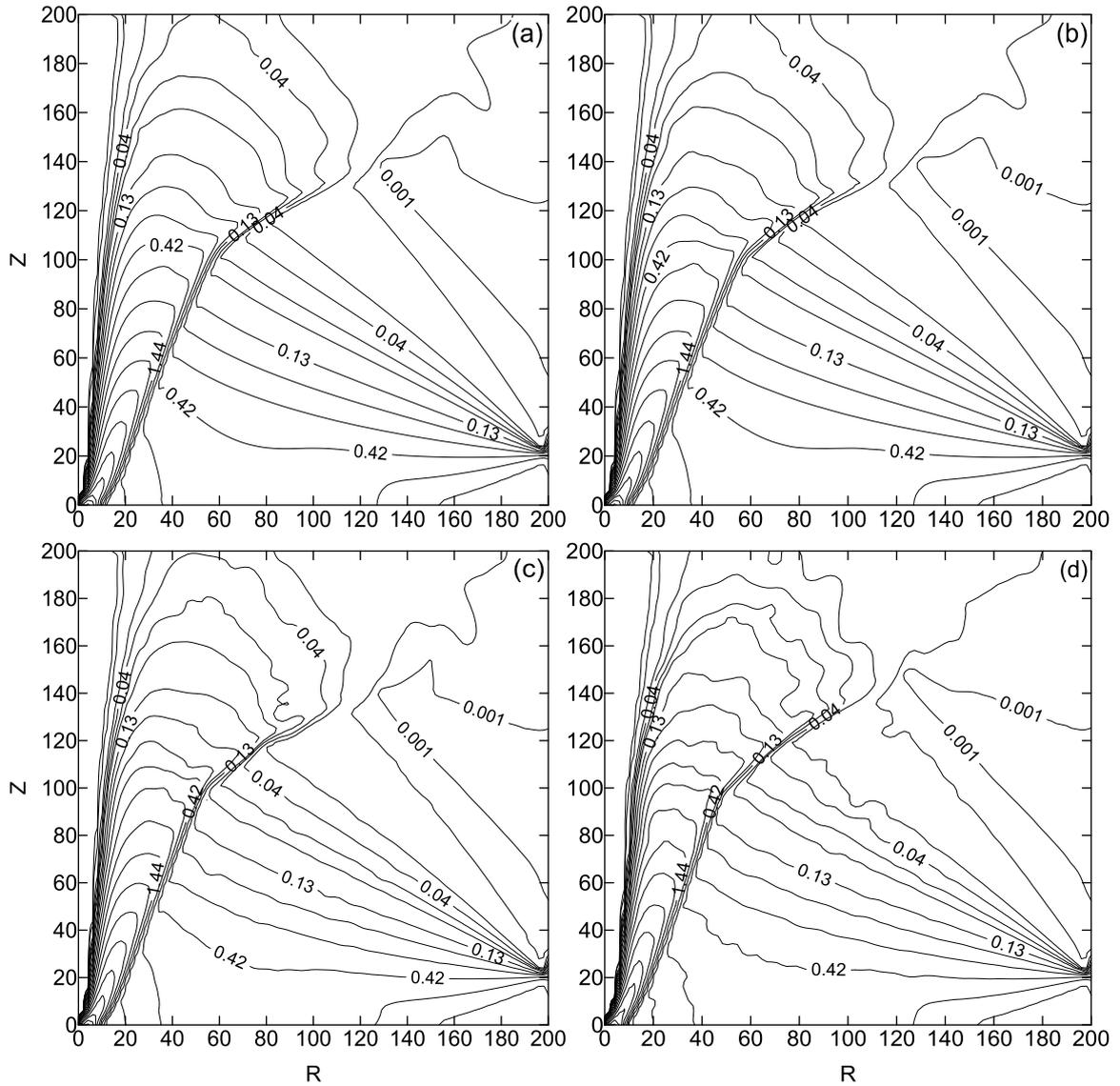
Figure 6.10: Change in the density contours in presence of cooling ($\lambda = 1$). See, text for details. The conical region between the axis and shock wave becomes denser as the accretion rate of the Keplerian disk is increased (Ghosh et al. 2011).
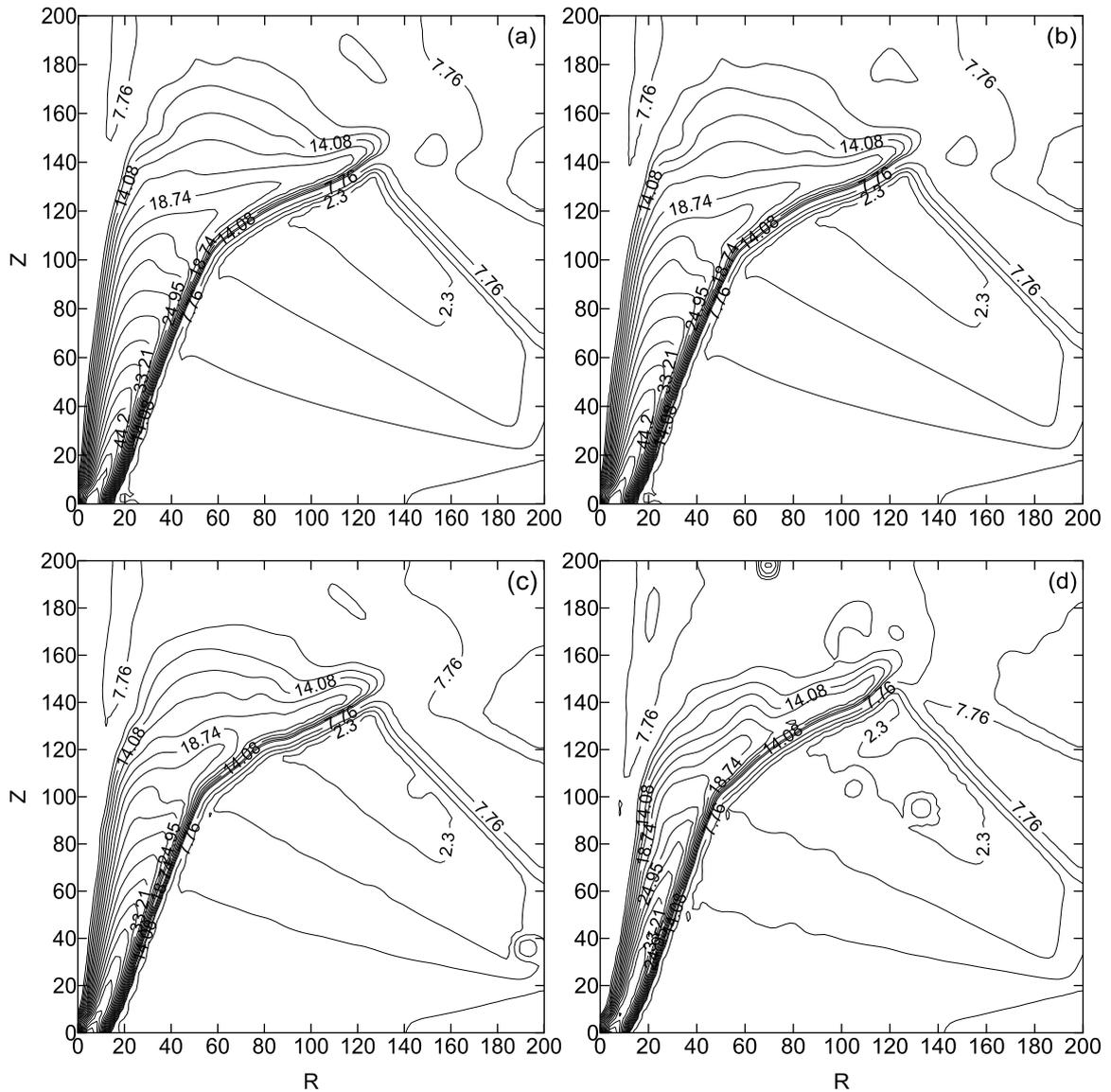
Figure 6.11: Change in the temperature contours in presence of cooling. The parameters are the same as in Fig. 6.10(a-d). The temperature values used to draw the contours are the same as in Fig. 6.9b. Note that the shock shifts closer to the axis with the increase in disk accretion rate (Ghosh et al. 2011).
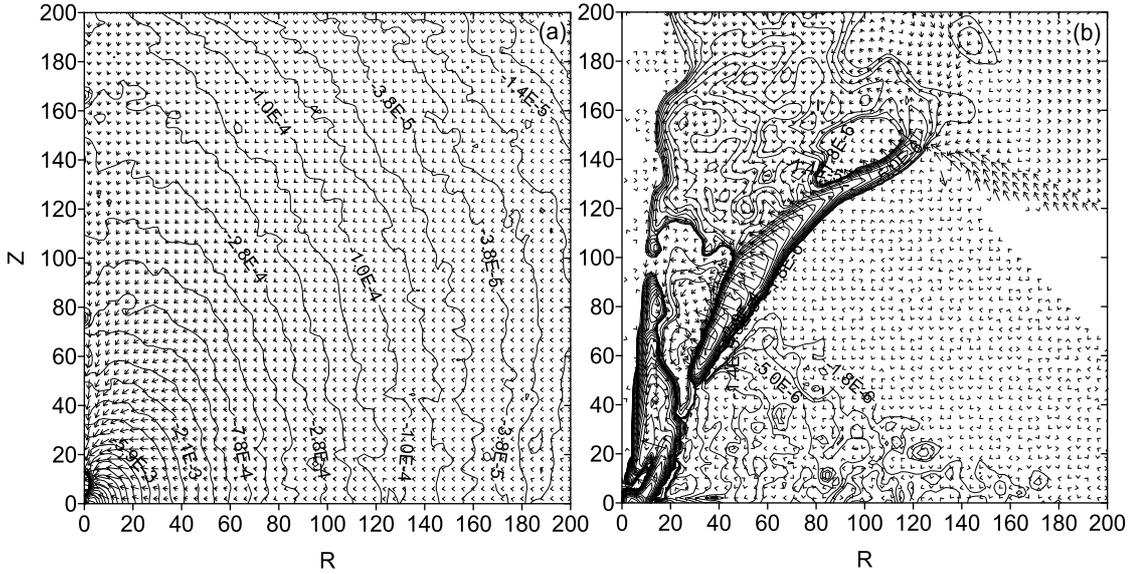
Figure 6.12: Difference in pressure and velocities between the flow with Comptonization and without Comptonization. Other parameters remain exactly the same. The cases are (a) Case 1d and (b) Case 2d of Table 6.1 respectively (Ghosh et al. 2011).

of the Compton cloud with iteration time of the coupled code (Cases 2(a-d), Table 6.1). With the increase of disk rate, the temperature of the Compton cloud saturates at lower temperature. Fig. 6.13b shows the effect of the decrease in cloud temperature due to the increase of disk rate over the spectrum. The spectrum becomes softer as we increase the disk rate, keeping the halo rate fixed.

In Fig. 6.14 we show the effects of increasing the electron number density (due to the increase of $\dot{m}_h$) for a fixed disk rate. The spectrum becomes harder as we increase the halo rate keeping the number of injected soft the photons the same.

We observe that the emerging spectrum has a bump, especially at higher accretion rates of the halo, at around 100 keV (e.g. the spectra marked 1g, 1h in Fig. 6.7a and the spectrum marked 2h in Fig. 6.14). A detailed analysis of the emerging photons having energies between 50 to 150 keV is done to see where in the Compton cloud they were produced. In Fig. 6.15a, we present the number of scatterings inside different spherical shells within the electron cloud suffered by these photons (50 < E < 150 keV) before leaving the cloud. Parameters used: $\dot{m}_d = 1$, $\dot{m}_h = 10$ and $\lambda = 0$. The light and dark shaded histograms are for the cloud with and without bulk velocity components, respectively. We find that the presence of bulk motion of the infalling electrons pushes the photons towards the hotter and denser [Figs. 6.2(a-b)] inner region of the cloud to suffer more and more scatterings. We find that the photons responsible for the bump suffered the maximum number
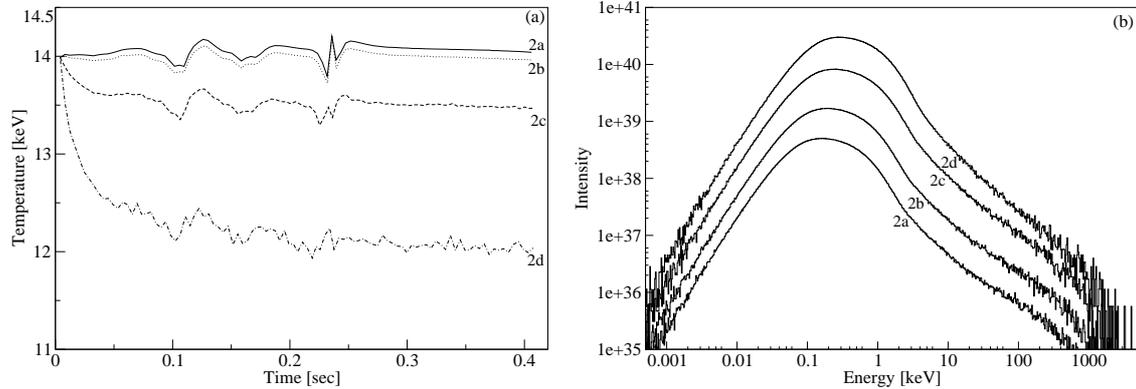
Figure 6.13: Variation of the (a) average temperature of the Compton cloud with iteration time and (b) spectrum with the increase of disk accretion rate. $\lambda = 1$ and $\dot{m}_h = 1$ are used. The solid, dotted, dashed and dash-dotted plots are for $\dot{m}_d = 1$, 2, 5 and 10 respectively. With the increase in the disk rate, the temperature of the Compton cloud saturates at lower temperature. The solid, dotted, dashed and dash-dotted curves show the spectrum for $\dot{m}_d = 1$, 2, 5 and 10 respectively. The spectrum is softer for higher value of $\dot{m}_d$ (Ghosh et al. 2011).
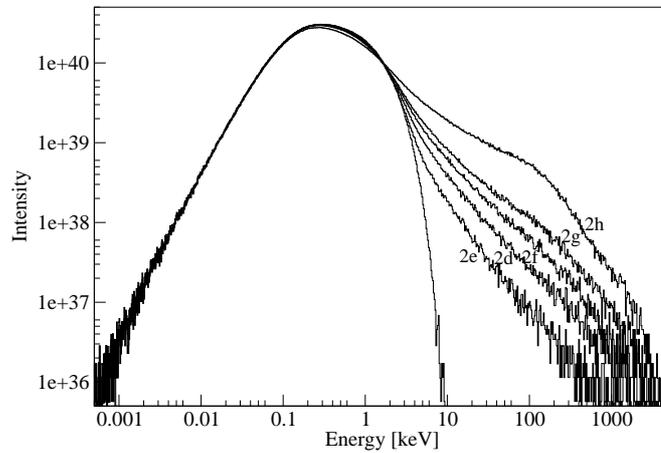
Figure 6.14: Variation of the spectrum with the increase of the halo accretion rate, keeping the disk rate ($\dot{m}_d = 10$) and angular momentum of the flow ($\lambda = 1$) fixed. The case number for which the spectra is drawn is marked in the plot. The unmarked plot is the injected spectrum. The spectrum becomes harder for the higher values of $\dot{m}_h$ (Ghosh et al. 2011).
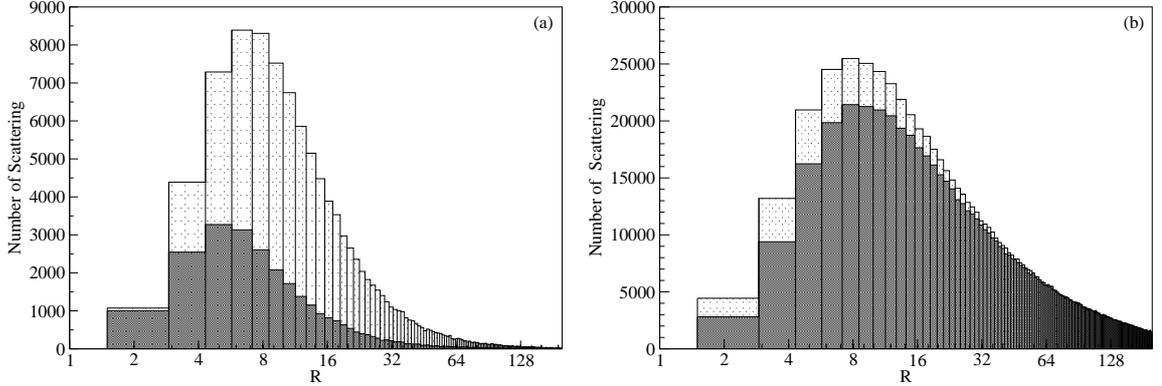
Figure 6.15: Number of scatterings inside the spherical shell between R to $R + \delta R$ ($\delta R \sim 1.4$). The light and dark shaded histograms are for the cloud with and without bulk velocity, respectively. (a) Only the photons emerging from the cloud with energies E, where 50 keV $< E <$ 150 keV, are considered here. (b) All the photons emerging from the cloud are considered here. Parameters used: $\dot{m}_d = 1$, $\dot{m}_h = 10$ and $\lambda = 0$ (Ghosh et al. 2011).

of scatterings around 8 r_g. From the temperature contours, we find that the cloud temperature around 8 r_g is $\sim$ 100 keV. In Fig. 6.15b, we consider all the outgoing photon energies. The inflowing bulk velocity of the electrons push the photons to the inner region of the accretion disk. Thus the photons that come out of the electron cloud suffer more scatterings in presence of the bulk velocity. As the effects of bulk velocity become more dominant, the difference between the two histograms also increases.

In Fig. 6.16, we explicitly show the effects of the bulk velocity on the spectrum. We note that the bump disappears when the bulk velocity of the electron cloud becomes zero (Curve marked 2). This fact shows that the region around 8 r_g behaves more like a black body emitter, which creates the bump. Since the photons are suffering large number of scatterings near this region (8 r_g), most of them emerge from the cloud with the characteristic temperature of the region. The effect of bulk velocity in this region is to force the photons to suffer larger number of scatterings. This bump vanishes for lower density cloud (low $\dot{m}_h$) as the photons suffer lesser number of scatterings. The photons which are scattered close to the black hole horizon and escape without any further scattering, produce the high energy tail in the output spectrum. Curve 3 of Fig. 6.16 shows the intensity spectrum of Case 1h (Table 6.1), when there are zero bulk velocity inside 3 r_g. We find that in the absence of bulk velocity inside 3 r_g, the high energy tail in the Curve 1h vanishes.
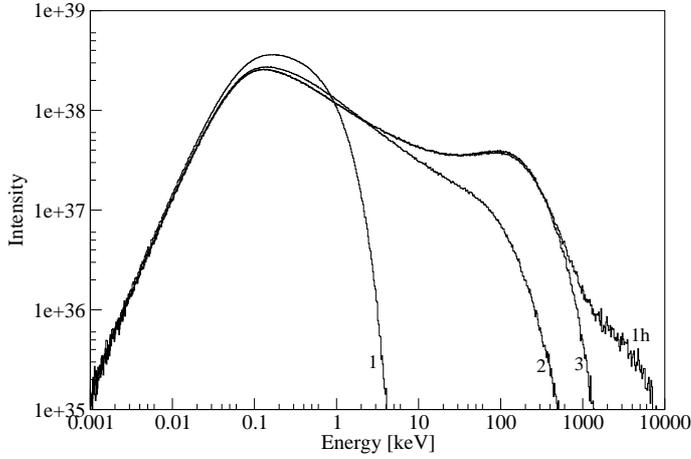
Figure 6.16: The spectrum for Case 1h of Table 6.1. The curves marked 2 and 3 give the spectra when the bulk velocity of the electron is absent for the whole cloud and for the cloud inside 3 r_g, respectively. The curve marked 1 gives the injected spectrum for the Case 1h of Table 6.1. The bulk motion Comptonization of the photons inside the 3 r_g radius creates the hard tail. The bump near 100 keV is a combined effect of the temperature and bulk velocity of rest of the cloud (Ghosh et al. 2011).

This is the clear signature of the presence of bulk motion Comptonization near the black hole horizon.

6.4.3   Compton Cloud with $\lambda = 1.5$

Let us now increase the specific angular momentum of the flow to $\lambda = 1.5$. In the case of non-dissipative flows in a vertical equilibrium, a flow is not supposed to form a shock wave (C90). However, when cooling is present we see that a shock has been formed due to the centrifugal barrier. In Fig. 6.17(a-b), we have shown the contours of constant density (Fig. 6.17a) and temperature (Fig. 6.17b) in absence of Compton cooling. Density contour levels are drawn from $0.001 - 0.03$ (successive level ratio is 5), $0.03 - 0.06$ (successive level ratio is 2), $0.06 - 0.68$ (successive level ratio is 1.5), $0.68 - 20.46$(successive level ratio is 1.3). Temperature contour levels are drawn from $2.3 - 11.64$ (successive level ratio is 1.5), $11.64 - 64.71$ (successive level ratio is 1.1), $64.71 - 346.21$ (successive level ratio is 1.15). We note that a shock stronger than the case $\lambda = 1$, has been formed which bends outwards away from the equatorial plane. The specific energy ϵ for the simulations presented in
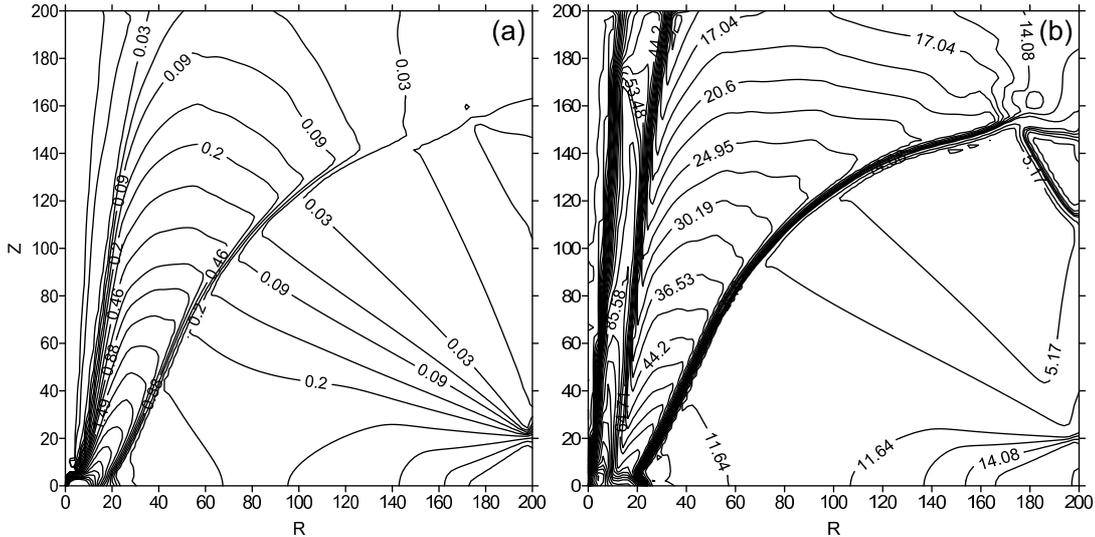
Figure 6.17: Same as Fig. 6.9(a-b) but for $(\lambda, \epsilon) = (1.5, 0.0007)$. Densities are in normalized unit and the temperatures are in keV. See, text for the values of the contour levels.

this Section is 0.0007.

In Figs. 6.18(a-b) and 6.19(a-b) we show the effects of the inclusion of a Keplerian disk at the equatorial plane. We find that the shock location is shifted inwards due to the Compton cooling. In Fig. 6.20 we have shown the variation of the location of the shock at the equatorial plane with the iteration time. We notice that the shock has been formed at a lower radius for $\dot{m}_d = 10$ than the $\dot{m}_d = 1$ case. This happens because for a higher disk rate the Compton cloud becomes cooler and the size of the Compton cloud becomes smaller. In Fig. 6.21 the variation of the average temperature of the cloud as the time goes, is shown. The cloud becomes cooler as the disk rate increases.

In Fig. 6.22 we plot the variation the spectral slope α with time for $\dot{m}_d = 1$ and $\dot{m}_d = 10$ keeping the halo rate $\dot{m}_h = 1$ fixed. We see that the spectrum becomes softer as the disk rate increases.

In Fig. 6.23, the variation of ratio of outflowing matter to injected matter with time when $\dot{m}_d$ is increased keeping $\dot{m}_h$ fixed is shown. The outflow rate decreases due to the increase in disk rate. We have also verified that the outflow rate increases with the increase in the specific angular momentum of the flow (Giri et al., 2010).

We now turn our attention to the variation of the shock location (Fig. 6.20). We find that the shock is oscillating in both the cases. In Fig. 6.24 we have plotted the power density spectrum (PDS) for these two cases. The PDS gives the frequency
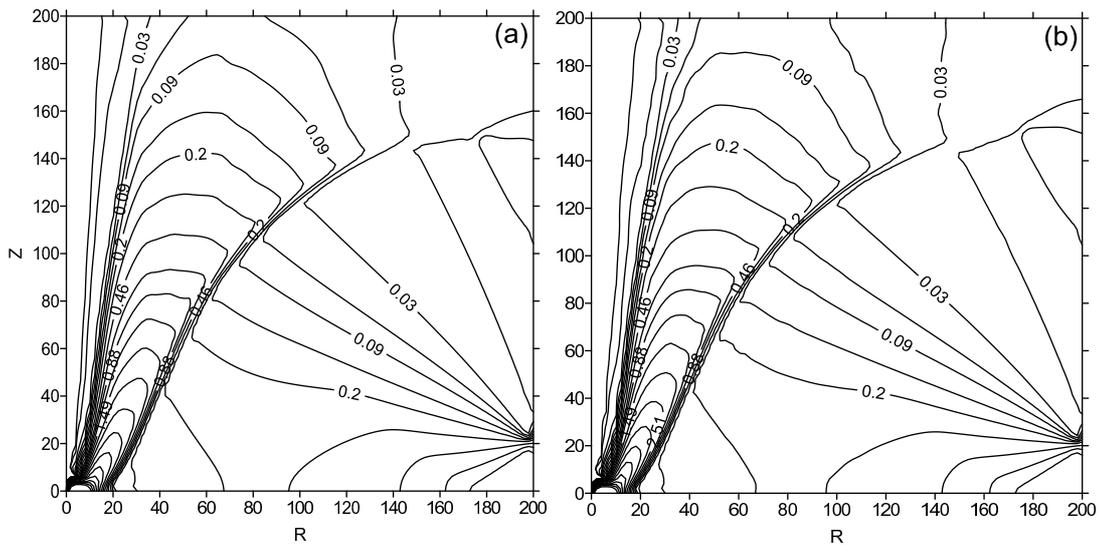
Figure 6.18: Change in the density contours in presence of cooling ($\lambda = 1.5$). The accretion rate of the halo is fixed $\dot{m}_h = 1$. (a) $\dot{m}_d = 1$ (b) $\dot{m}_d = 10$. Due to the increase of disk rate (N_{inj}), the size of the post shock Compton cloud decreases. The density values used to draw the contours are same as in Fig. 6.17a.
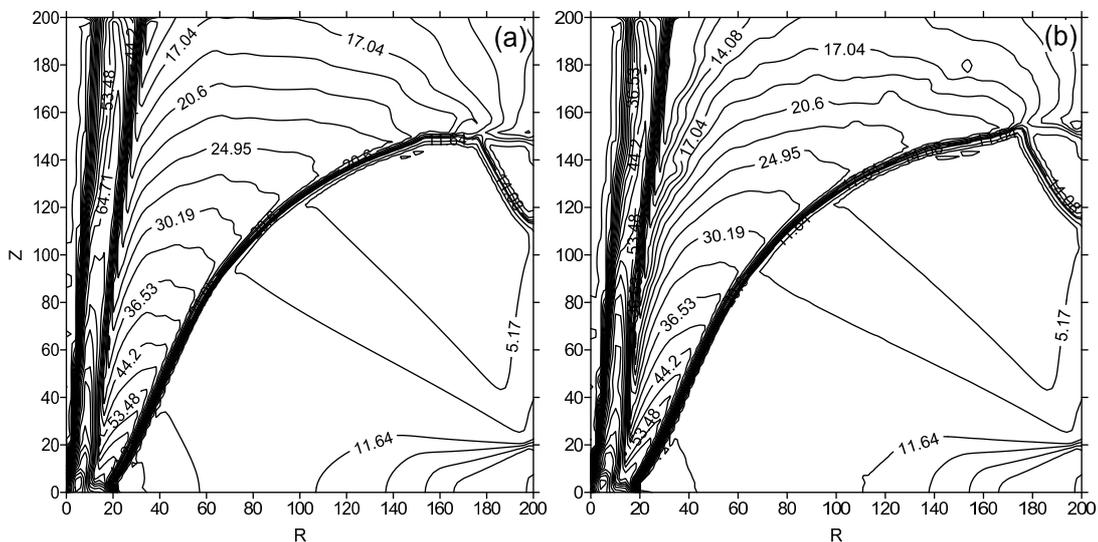

Figure 6.19: Change in the temperature contours in presence of cooling. The parameters are the same as in Fig. 6.18(a-b).
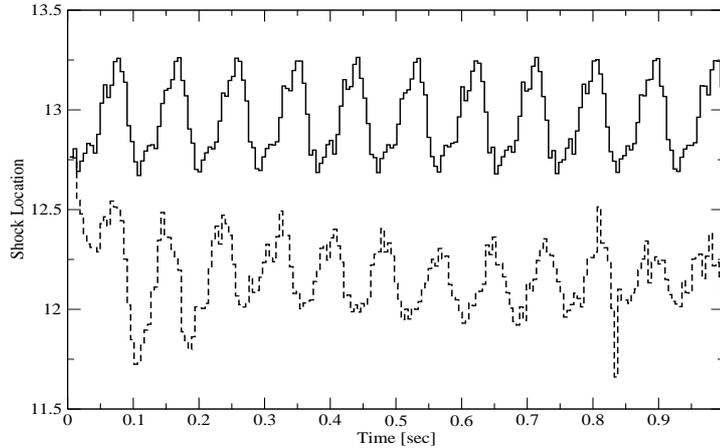
Figure 6.20: Variation of the shock locations with iteration time. Parameters used: $\dot{m}_d = 1$ (solid curve), $\dot{m}_d = 10$ (dotted curve). $\dot{m}_h = 1$ for both the cases.

of oscillation for $\dot{m}_d = 1$ to be $\nu_{QPO} = 10$ Hz. The oscillation frequency slightly increases for the $\dot{m}_d = 10$ case. We also note that for the higher disk rate, the amplitude of the QPO has a lower value.

6.5   Fate of the Jet and the High Angular Momentum Flows in Presence of Cooling

So far, we have concentrated on the spectral properties of disk-jet system with passive velocity distribution. We also studied low angular momentum systems which do not produce very strong jets. However, in a realistic system, the angular momentum close to the black hole could be around the marginally stable and bound values ($\sim 1.83 - 2$ in our units).

Physically, when the angular momentum is increased, the shocks can form at a larger radii. With the increase of cooling (Keplerian disk rate) the shock moves closer to the black hole. The shock oscillations occur as before (previous Section), but the oscillations damp out as the cooling is increased. The post-shock region also collapses with the increase in cooling (Garain, Ghosh and Chakrabarti, 2012). Most interestingly, since the formation of the jet is from CENBOL in this model, our result clearly shows that the outflow rate is greatly reduced as the cooling rate is increased. This quenching of jet the phenomenon directly shows that correlation between the spectral states and the outflow rates (Garain, Ghosh and Chakrabarti, 2012).
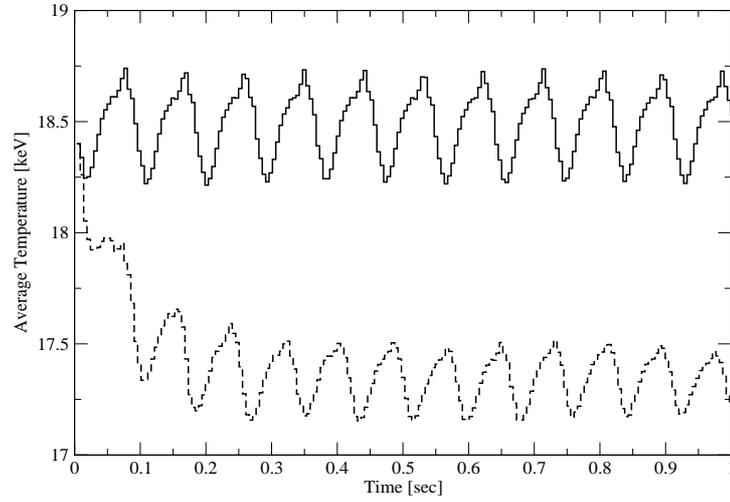
Figure 6.21: Same as Fig. 6.13(a) but for $(\lambda, \epsilon) = (1.5, 0.0007)$. With the increase in disk rate the average temperature of the cloud decreases.
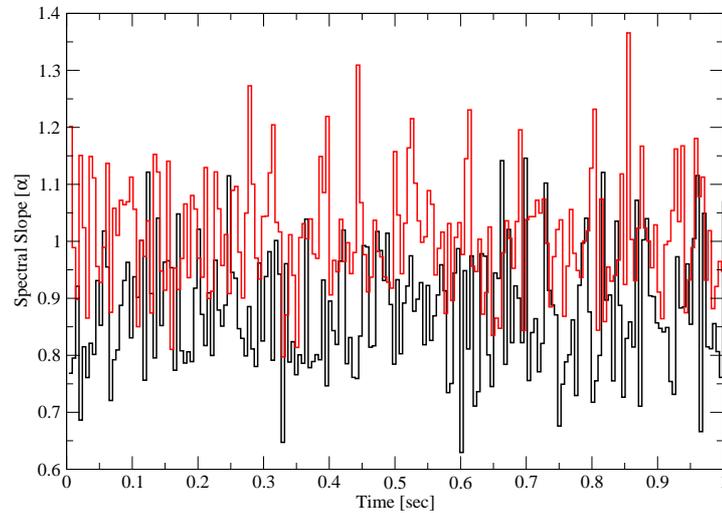

Figure 6.22: Variation of the spectral slope α with iteration time. Parameters used: $\dot{m}_d = 1$ (black curve), $\dot{m}_d = 10$ (red curve). $\dot{m}_h = 1$ for both the cases. As $\dot{m}_d$ increases the spectrum becomes softer.
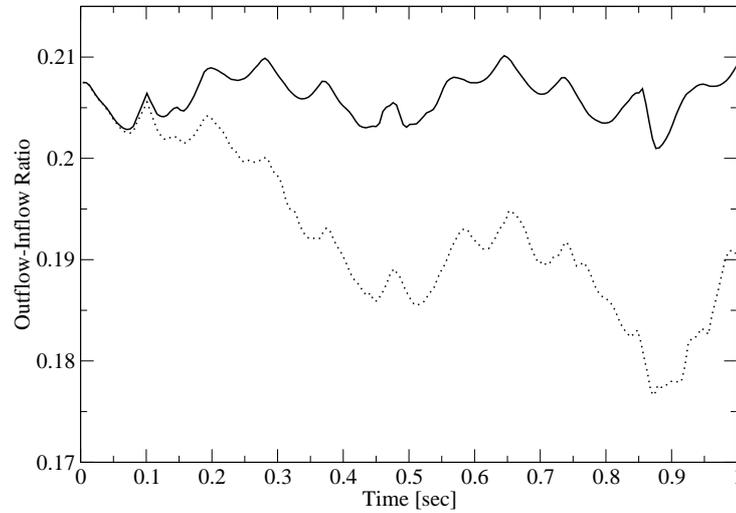
Figure 6.23: Variation of the ratio between outflow and inflow rate with iteration time. Parameters used: $\dot{m}_d = 1$ (solid curve), $\dot{m}_d = 10$ (dotted curve). $\dot{m}_h = 1$ for both the cases. For the same halo profile, as the number of soft photons increases (due to the increase in disk rate) the outflow rate decreases.
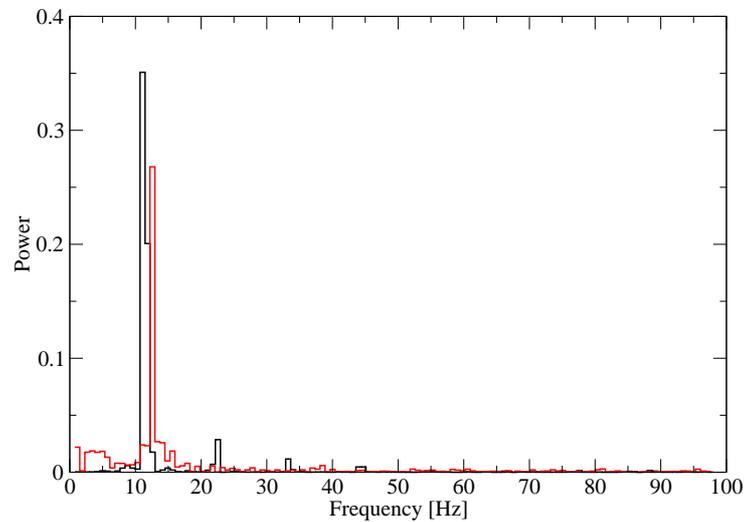

Figure 6.24: Power density spectra of the time variation of the shock locations are shown. Parameters used: $\dot{m}_d = 1$ (black curve), $\dot{m}_d = 10$ (red curve). $\dot{m}_h = 1$ for both the cases. As the disk rate increases, the post shock region oscillates at a slightly higher frequency but with a lower power.

Chapter 7

Conclusions and Future Plans

So far, we described the developement of a radiative transfer Monte Carlo code and presented its applications to various astrophysical problems. We started with a brief introduction of 'compact objects' and also presented a simple classifications of such objects based on their mass limit. We mentioned the importance of accretion process around a compact object and briefly described the history of the observational evidences from black holes. In Section 1.4 we have discussed the spectral properties of galactic and extragalactic black holes in X-rays and their possible origin. There are quite a few accretion disk models present in the literature. We have listed some of the basic accretion disk models in Sections 1.5 and 1.6, starting from Bondi flow to TCAF. In this Thesis, we have mainly focused on the spectral properties of the radiations coming from an accretion disk. The processes responsible for the emission of radiation from an accretion flow has been listed in Section 1.7. A black hole system is general relativistic in nature. In our work we have used a pseudo-Newtonian potential which mimics the space time of a Schwarzschild black hole.

The mechanisms responsible for the emission of radiations from an accretion disk are discussed in details in Chapter 2. We have started with the black body radiation and calculated the total number of photons generated from a black body at temperatute T. Next we discuss in detail the Compton scattering process between an electron and a photon. We calculate the probability of a photon to be scattered and the energy exchange between an electron and a photon due to the scattering.

In Chapter 3, we discuss the Monte Carlo techniques through which we have incorporated the radiative transfer into our code. We have shown the results of some simple Monte Carlo simulations at the end of Chapter 3.

In Chapter 4, we have presented several results of Monte Carlo simulation of Comptonization by hot electron clouds which surround the black hole in the form of a toroidal shaped centrifugal pressure dominated boundary layer. The soft photons are supplied by a Keplerian disk which reside just outside this cloud. We verify several of

the previously reported conclusions obtained by theoretical methods. We find that for a given supply of the injected soft photons, the spectrum can become harder (i.e., spectral index α can go down) when either the optical depth is increased (electron number density goes up) and/or the electron temperature is increased. Furthermore, we found how the spectral shape changes when the Compton cloud expands and shrinks. We compute exactly what fraction of the photons are intercepted and processes and compute the percentage of scattered photons as functions of the flow variables. These results would be valuable to interpret the observational results from black hole candidates, especially when the spectral index is found to be changed.

In Chapter 5, we have extended the results of our previous work on Monte-Carlo simulations. We include the outflow in conjunction with the inflow. The outflow rate is self-consistently computed from the inflow rate using the well-known considerations present in the literature (Das et al. 2001 and references therein). We compute the effects of the thermal and the bulk motion Comptonization on the soft photons emitted from a Keplerian disk around a black hole by the post-shock region of a sub-Keplerian flow which surrounds the Keplerian disk. A shock in the inflow increases the CENBOL temperature, increases the electron number density and reduces the bulk velocity. Thermal Comptonization and bulk motion Comptonization inside the CENBOL increases photon energy. However, the CENBOL also generates the outflow of matter which down-scatters the photons to lower energy. We show that the thermal Comptonization and the bulk motion Comptonization are possible in both the accretion and the outflows. While the converging flow up-scatters the radiation, the outflow down-scatters. However, the net effect is not simple. The outflow parameters are strongly coupled to the inflow parameters and thus for a given inflow and outflow geometry, the strength of the shock can also determine whether the net scattering by the jets would be significant or not. Sometimes the spectrum may become very complex with two power-law indices, one from thermal and the other from the bulk motion Comptonization. Since the volume of the jet may be larger than that of the CENBOL, sometimes the number of scatterings suffered by softer photons from the electrons in the jet may be high. However, whether the CENBOL or the jet emerging from it will dominate in shaping the spectrum strongly depends on the geometry of the flow and the strength of the shock. We also found that the halo can Comptonize and harden the spectrum even without the CENBOL.

Chapter 4 and Chapter 5 contained the results of the simulations where a particular geometry of the electron cloud is assumed (toroidal electron cloud in Chapter 4 and spherical inflow in conjunction with a conical jet in Chapter 5). In Chapter 6, we have shown the results of the Monte Carlo simulations, where no such geometry for the Compton cloud is assumed. The geometry and the hydrodynamics of the flow is

now simulated at each iteration time step by a Total Variation Diminishing (TVD) code and is used as the initial conditions in the radiative transfer code. We have included the effects of Compton cooling into the Monte Carlo code. The coupled Monte Carlo-TVD code simulates the spectra and hydrodynamics of the accretion disk around a stellar mass black hole. In Section 6.3, we describe the procedure to couple the hydrodynamic and the radiative transfer code. Our major conclusions in this Chapter are: first, in the presence of an axisymmetric disk which supplies soft photons to the Compton cloud, even an originally spherically symmetric accreting Compton cloud becomes axisymmetric. This is because, due to the higher optical depth, there is a significant cooling near the axis of the intervening accreting halo between the disk and the axis. Second, due to the cooling effects close to the axis, the pressure drops significantly, which may change the flow velocity up to 25 per cent. Third, this effect becomes more for low angular momentum flows which produce shock waves close to the axis. The post-shock region cools down and the outflow falls back to the disk. This shows that the Chakrabarti & Manickam (2000) mechanism of the effects of Comptonization of outflows does take place. Fourth, the emitted spectrum is direction-dependent. The spectrum along the axis shows a large soft bump, while the spectrum along the equatorial plane is harder. Fifth, we also find that photons which spend more time (up to 100 ms in the case considered) inside the Compton cloud produce harder spectrum as they scatter several times However, if they spend too much (above 100 ms) time, they transfer their energies back to the cooler electrons while escaping. These results would be valuable for interpreting the timing properties of the radiation from black hole candidates.

At the end of Chapter 6, we have shown some simulation results which we obtained using the coupled Monte Carlo-TVD simulation for an accretion disk having a higher angular momentum than the previously presented cases. Here a shock has been generated because of the centrifugal barrier. The shock location oscillates with time and the oscillation gives rise to the Quasi Periodic Oscillation. We find the spectral slope also changing during the oscillation of the shock.

In this Thesis, we have worked with zero or very low angular momentum accretion flows only. In future we will extend our simulations for those cases where strong shocks are present. In presence of cooling an oscillating shock may stop oscillation or a steady shock may start oscillating. We like to study the spectral properties for those systems. In future we will include synchrotron and bremsstrahlung radiation in our code. Stochastic magnetic fields would produce synchrotron radiations everywhere and thus the soft photon source would be distributed. We will also carry out satellite data analysis and fit our simulated spectra, time lag/lead, angle dependent spectral properties etc. with observed results.

The entire work of this Thesis has been done in the Schwarzschild black hole

geometry using pseudo-Newtonian potential. However, since black holes form out of rotating collapsing stars and sometimes collapse is induced by the rotating accretion matter, it is not unlikely that many, if not all, of the black holes are actually Kerr type. In future, we shall continue our work in Kerr geometry and look for tell tale signatures of the rotation parameter of the black hole.

Bibliography

Agrawal, P. C. et al., 1972, *Ap. Sp. Sci.*, **18**, 408

Blandford, R. D. & McKee, C. F., 1982, *Astrophys. J.*, **255**, 419

Bondi, H., 1952, *MNRAS*, **112**, 195

Case, G. L. et al., 2005, *ChJAA*, **5**, 341

Chakrabarti, S. K., 1985, *Astrophys. J.*, **288**, 1

Chakrabarti, S. K., Jin, L. & Arnett, W. D., 1987, *Astrophys. J.*, **313**, 674

Chakrabarti, S. K., 1989, *Astrophys. J.*, **347**, 365

Chakrabarti, S. K., 1990, *Theory of Transonic Astrophysical Flows*, (World Scientific: Singapore) (C90)

Chakrabarti, S. K. & Molteni, D., 1993, *Astrophys. J.*, **417**, 671

Chakrabarti, S. K. & Titarchuk, L. G., 1995, *Astrophys. J.*, **455**, 623 (CT95)

Chakrabarti, S. K., 1996a, *Phys. Rep.*, **266**, 229

Chakrabarti, S. K. 1996b, *Astrophys. J.*, **464**, 664

Chakrabarti, S. K., 1996c, *Astrophys. J.*, **471**, 237

Chakrabarti, S. K., Titarchuk, L. G., Kazanas, D. & Ebisawa, K., 1996, *Astron. Astrophys. Supp. Ser.*, **120**, 163

Chakrabarti, S. K., 1997, *Astrophys. J.*, **484**, 313 (C97)

Chakrabarti, S. K., Sahu, S. A., 1997, *Astron. Astrophys.*, **323**, 382

Chakrabarti, S. K., 1998a, *Ind. J. Phys.*, **72B**, 565

Chakrabarti, S. K., 1998b, *Black Holes: Theory and Observations*, Eds. F. W. Hehl, C. Keifer and R. J. K. Metzler, 80

Chakrabarti, S. K., 1999, *Astron. Astrophys.*, **351**, 185 (C99)

Chakrabarti, S. K. & Manickam, S. G., 2000, *Astrophys. J.*, **531**, L41

Chakrabarti, S. K. & Nandi, A., 2000, *Ind. J. Phys.*, **75(B)**, 1

Chakrabarti, S. K., Nandi, A., Manickam, S. G., Mandal, S. & Rao A. R., 2002, *Astrophys. J.*, **579**, 21

Chakrabarti, S. K., 2003, *Proc. 10th Marcel Grossman Meeting on General Relativity*, Eds. M. Novello, S. P. Bergliaffa and R. Ruffini, 559 (World Scientific: Singapore)

Chakrabarti, S. K., Acharyya, K. & Molteni, D., 2004, *Astron. Astrophys.*, **421**, 1

Chakrabarti, S. K., 2005, *Astrophysics & Space Science*, **297**, 131

Chakrabarti S. K. & Mandal, S., 2006, *Astrophys. J.*, **642**, L49

Chakrabarti, S. K., Ghosh, H. & Som, D., 2008, *Proc. 11th Marcel Grossman Meeting on General Relativity*, Eds. H. Kleinert, R. T. Jantzen and R. Ruffini, 1085 (World Scientific: Singapore) (CGS08)

Chakrabarti, S. K., 2008, *Proc. Observational Evidence for Black Holes in the Universe*, Eds. S. K. Chakrabarti and A. S. Majumdar, 325, (AIP: NY)

Chattopadhyay, I., 2003, *Ph.D. thesis*, Jadavpur University

Colpi, M., Maraschi, L. & Treves, A., 1984, *Astrophys. J.*, **280**, 319

Das, T. & Chakrabarti, S. K., 1999, *Class. and Quant. Grav.*, **16**, 3879

Das, S., Chattopadhyay, I., Nandi, A. & Chakrabarti, S. K., 2001, *Astron. Astrophys.*, **379**, 683

Diehl, R., 2001, *The Universe in Gamma Rays*, Eds. Schonfelder, V., 9, (Springer: Germany)

Dutta, B. G. & Chakrabarti, S. K., 2010, *MNRAS*, **404**, 2136

Ebisawa, K., Titarchuk, L. & Chakrabarti, S. K., 1996, *Publ. of the Astronomical Society of Japan*, **48**, 59

Galeev, A. A., Rosner, R. & Vaiana, G. S., 1979, *Astrophys. J.*, **229**, 318

Garain, S. K., Ghosh, H. & Chakrabarti, S. K., 2012, *Astrophys. J.* (to appear)

Ghosh, H., Chakrabarti, S. K. & Laurent, P., 2009, *Int. J. Mod. Phys.*, **18**, 1693 (GCL09)

Ghosh, H., Garain, S. K., Chakrabarti, S. K. & Laurent, P., 2010, *Int. J. Mod. Phys.*, **19**, 607 (GG10)

Ghosh, H., Garain, S. K., Giri, K. & Chakrabarti, S. K., 2011, *MNRAS*, **416**, 959

Giacconi, R., Gursky, H., Paolini, F. & Rossi, B., 1962, *Phys. Rev. Lets.*, **9**, 439

Giacconi, R., Gursky, H. & Waters, J. R., 1965, *Nature*, **207**, 572

Giacconi, R., Kellogg, E., Gorenstein, P., Gursky, H. & Tahanbaum, H., 1971, *Astrophys. J.*, **165**, L27

Giri, K., Chakrabarti, S. K., Samanta, M. M. & Ryu, D., 2010, *MNRAS*, **403**, 516

Gursky, H., Giacconi, R., Gorenstein, P., Waters, J. R., Oda, Bradt, H., Garmire, G. & Sreekantan, B. V., 1966, *Astrophys. J.*, **144**, 1249

Haardt, F. & Maraschi, L., 1991, *Astrophys. J.*, **380**, 51

Haardt, F. & Maraschi, L., 1993, *Astrophys. J.*, **413**, 507

Hawking, S. W., 1971, *MNRAS*, **152**, 75

Hua, J.M., & Titarchuk, L. G., 1996, *Astrophys. J.*, **469**, 280

Katz, J. I., 1976, *Astrophys. J.*, **206**, 910

Landau, L. D. & Lifshits, E. M., 1976, *The Classical Theory of Fields*, 4th ed., Pergamon

Laurent, P. & Titarchuk, L. G., 1999, *Astrophys. J.*, **511**, 289

Laurent, P. & Titarchuk, L. G., 2001, *Astrophys. J.*, **562**, 67

Laurent, P. & Titarchuk, L., 2007, *Astrophys. J.*, **656**, 1056

Ling, J. C. & Wheaton, W. A., 2003, *Astrophys. J.*, **584**, 399

Ling, J. C. & Wheaton, W. A., 2005, *Astrophys. J.*, **622**, 492

Liu, Q. Z., van Paradijs, J. & van den Heuvel, E. P. J., 2006, *Astron. Astrophys.*, **455**, 1165

Liu, Q. Z., van Paradijs, J. & van den Heuvel, E. P. J., 2007, *Astron. Astrophys.*, **469**, 807

Longair, M. S., 1981, *High Energy Astrophysics*, (Cambridge Univ. Press: UK)

Malkan, M. A. & Sergent, W. A. W., 1982, *Astrophys. J.*, **254**, 22

McClintock, J. E. & Remillard, R. A., 1986, *Astrophys. J.*, **308**, 110

McConnell et al., 2002, *Astrophys. J.*, **572**, 984

Mitsuda, K., Inoue, H., Koyama, K., Makishima, K., Matsuoka, M., Ogawara, Y., Shibazaki, N., Suzuki, K. & Tanaka, Y., 1984, *Publ. Astron. Soc. Japan*, **36**, 741

Molteni, D., Lanzafame, G. & Chakrabarti, S. K., 1994, *Astrophys. J.*, **425**, 161

Molteni, D., Sponholz, H. & Chakrabarti, S. K., 1996, *Astrophys. J.*, **457**, 805 (MSC96)

Molteni, D., Ryu, D. & Chakrabarti, S. K., 1996, *Astrophys. J.*, **470**, 460

Nandi, A., Chakrabarti, S. K., Vadawale, S. V. & Rao A. R., 2001, *Astron. Astrophys.*, **380**, 245

Novikov, I. & Thorne, K. S., 1973, *Black Holes*, Eds. C. DeWitt and B. DeWitt, 343, (Gordon and Breach, New York)

Paczyński, B. & Wiita, P. J., 1980, *Astron. Astrophys.*, **88**, 23 (PW80)

Parker, E. N., 1959, *Astrophys. J.*, **129**, 217

Payne, D. G. & Blandford, R. D., 1981, *MNRAS*, **196**, 781

Pottschmidt, K., Chernyakova, M., Zdziarski, A. A., Lubinski, P., Smith, D. M. & Bezayiff, N., 2006, *Astron. Astrophys.*, **452**, 285

Pounds, K. A., Reeves, J. N., King, A. R. & Page, K. L., 2004, *MNRAS*, **350**, 10

Pozdnyakov, L. A., Sobol, I. M. & Sunyaev, R. A., 1983, *Astrophys. Space Sci. Rev.*, **2**, 189 (PSS83)

Rees, M. J., Begelman, M. C., Blandford, R. D. & Phinney, E. S., 1982, *Nature*, **295**, 17

Reilly, K. T., 2002, SLAC-Report-610, Stanford University

Ross, R. R., Fabian, A. C. & Mineshige, S., 1992, *MNRAS*, **258**, 189

Rybicki, G. B. & Lightman, A. P., 1979, *Radiative Processes in Astrophysics* (New York: Wiley-Interscience) (RL79)

Ryu, D., Chakrabarti, S. K. & Molteni, D., 1997, *Astrophys. J.*, **474**, 378

Shakura, N. I., 1972, *Astron. Zhur.*, **49**, 921

Shakura, N. I. & Sunyaev, R. A., 1973, *Astron. Astrophys.*, **24**, 337 (SS73)

Shapiro, S. & Teukolsky, S., 1983, *Black Holes, Neutron Stars and White Dwarfs*, (John Wiley & Sons, New York)

Smith, D. M., Heindl, W. A. & Swank, J. H., 2002, *Astrophys. J.*, **569**, 362

Sobol, I. M., 1994, *A Primar to the Monte Crlo Method* (USA: CRC Press)

Soria, R., Wu, K., Hannikainen, D., McCollough, M. & Hunstead, R., 2001, *Proc. Joint Workshop on X-ray Emission from Accretion onto Black Holes*, Eds. Yaqoob T. and Krolik J. H., 65 (astro-ph/0108084v1)

Sun, W. H. & Malkan, M. A., 1989, *Astrophys. J.*, **346**, 68

Sunyaev, R. A. & Trümper, J., 1979, *Nature*, **279**, 506

Sunyaev, R. A. & Titarchuk, L. G. 1980, *Astron. Astrophys.*, **86**, 121 (ST80)

Sunyaev, R. A. & Titarchuk, L. G. 1985, *Astron. Astrophys.*, **143**, 374 (ST85)

Tananbaum, H. et al., 1972, *Astrophys. J.*, **177**, L5

Thorne, S. & Price, R., 1975, *Astrophys. J.*, **195**, L101

Titarchuk, L., 1994, *Astrophys. J.*, **434**, 570

van den Heuvel E. P. J., 1975, *Astrophys. J.*, **198**, L109

van Paradijs, J. & McClintock, J. E., 1995, *X-Ray Binaries*, Eds. W. H. G. Lewin, J. van Paradijs and E. P. J. van den Heuvel, 58 (Cambridge: Cambridge Univ. Press)

Wandel, A., Yahil, A. & Milgrom, M., 1984, *Astrophys. J.*, **282**, 53

Wandel, A. & Petrosian, V., 1988, *Astrophys. J.*, **329**, L11

Weinberg, S., 1972, *Gravitation and Cosmology*, (John Wiley & Sons, Inc.)

Wu et al., 2002, *Astrophys. J.*, **565**, 1161

Zel'dovich, Ta. B. & Novikov, I. D., 1966, *Sov. Astron.-AJ*, **10**, 602

Zhang, F., Li, X. D. & Wang, Z. R., 2004, *Astrophys. J.*, **603**, 663